2012

The Effects Of Deposition Conditions On Rf Sputtered Gallium Tin Zinc Oxide Thin Film Transistors

Tanina Bradley
North Carolina Agricultural and Technical State University

THE EFFECTS OF DEPOSITION CONDITIONS ON RF SPUTTERED GALLIUM TIN ZINC OXIDE THIN FILM TRANSISTORS

by

Tanina Bradley

A dissertation submitted to the graduate faculty
in partial fulfillment of the requirements for the degree of
DOCTOR OF PHILOSOPHY

Department: Electrical and Computer Engineering
Major: Electrical Engineering
Major Professor: Dr. Shanthi Iyer

North Carolina A&T State University
Greensboro, North Carolina
2012

ABSTRACT

Bradley, Tanina. THE EFFECTS OF DEPOSITION CONDITIONS ON RF SPUTTERED GALLIUM TIN ZINC OXIDE THIN FILM TRANSISTORS. **(Major Professor: Dr. Shanthi Iyer)**, North Carolina Agricultural and Technical State University.

Thin film transistors (TFTs) were fabricated with a transparent amorphous gallium tin zinc oxide (GSZO) channel layer. GSZO is a promising, low cost replacement for the commonly used indium gallium zinc oxide (IGZO).The transistors were fabricated on Si substrates to optimize performance prior to transferring device production to flexible substrates. This dissertation will address the effects of deposition and post-deposition parameters on the film properties and interface traps. It will also address the parameters' resultant effects on device performance and stability with the use of various characterization techniques. Film properties were studied using x-ray diffraction (XRD) and transmission measurements to assess the structural and optical properties of the deposited films. X-ray photoelectron spectroscopy (XPS) analysis was performed to determine the surface composition of the channel layer, and correlate the surface properties to the resulting device performance. Enhancement and depletion mode devices were fabricated. TFT performance was evaluated through the current-voltage (I-V) characteristics of the devices under normal, electrically stressed and photo-excited conditions operating conditions. Depletion mode TFTs were produced with drain current (I_D)= 10^{-6} A, threshold voltage (V_T)= -3 V, subthreshold swing (SS)= 1.3 V/decade, and on/off current ratio ($I_{on/off}$)= 10^6 when operated in the dark without gate stress. TFTs with 10 sccm oxygen incorporation during deposited and post-deposition annealing at 250 °C

exhibits the best performance amongst enhancement mode devices with I_D of 10^{-7}A, V_T of 3 V SS of 1.33 V / decade, and $I_{on/off}$ of 10^6. In addition, a stable RT deposited TFT has been achieved with 2 sccm oxygen incorporation, and 250 °C post deposition annealing temperature, that exhibits a ΔV_T as low as ~0.5 V for a 3hour stress period under a gate bias of 1.2 and 12 V.

School of Graduate Studies
North Carolina Agricultural and Technical State University

This is to certify that the Doctoral Dissertation of

Tanina Bradley

has met the dissertation requirements of
North Carolina Agricultural and Technical State University

Greensboro, North Carolina
2012

Approved by:

_____	_____
Dr. Shanthi Iyer Major Professor	Dr. Garry Cunningham Committee Member
_____	_____
Dr. Ward Collis Committee Member	Dr. Eric Forsythe Committee Member
_____	_____
Dr. Numan Dogan Committee Member	Dr. John Kelly Department Chairperson

_____
Dr. Sanjiv Sarin
Associate Vice Chancellor for Research and Dean of Graduate Studies

DEDICATION

This work is dedicated to my family and friends who have supported me throughout the doctoral program. Without their encouragement, this work would not have come to fruition.

BIOGRAPHICAL SKETCH

Tanina Bradley was born in Philadelphia, Pennsylvania. She received the Bachelor of Science degree in Engineering Physics from North Carolina Agricultural and Technical State University in 2004 and the Master of Science degree in Electrical Engineering from the University of North Carolina Charlotte in 2006. She is a candidate for the Doctoral degree in Electrical Engineering.

ACKNOWLEDGEMENTS

There are numerous individuals that contributed to the completion of this work and the mental sanity of its author. I thank my advisor Dr. Shanthi Iyer, who's knowledge and guidance helped me grow as a researcher. I thank my research group for their insight and assistance throughout this project. A special thanks goes to my group members who worked with me on the Center of Excellence for Battlefield Capability Enhancements: Environmentally Stable Flexible Displays project Robert Alston, Shereen Farhana, and Dr. Jia Li. Thank you Ms. Willetta Stamp for believing in my ability and encouraging me to overcome the hurdles encountered. In addition, I thank my friends who have supported me and become my cheerleaders throughout this process. I specifically thank my friends, Husniyah Abdus-Salaam, Adam Bowen, James Griggs, and Sharonda Eggleton, who have consistently been a source of encouragement and entertainment. I thank my family members, who have been my inspiration since the beginning of my education. Thank you Terry Lee Sr., Jessie Bradley, Terry Lee Jr., Damon Bradley, and Ella Bradley for the constant calls to keep me motivated and check on my progress. Lastly, it is impossible to offer sufficient thanks to my mother Tanina A. Bradley, who has been my source of sanity and reason through all things, and without whom this degree would have never been completed.

The work presented was supported by the Army Research Office contracts W911NF-04-2-0051 and W911NF-10-1-0316 (technical monitors John Zavada and Michael Gerhold) and the Department of Education through the Title III program.

TABLE OF CONTENTS

LIST OF FIGURES

FIGURES **PAGE**

LIST OF TABLES

TABLES **PAGE**

LIST OF SYMBOLS

ε	Photon energy
μ	Mobility
Ar	Argon
at. %	Atomic percent
a.u.	Arbitrary units
Au	Gold
BE	Binding energy
CB	Conduction band
CBM	Conduction band minimum
C_{ox}	Oxide capacitance
DC	Direct current
DI	Deionized
D_{it}	Density of interface traps
DOS	Density of states
E_C	Conduction band energy
ET	Elevated temperature
et al.	Et alia “and others”
Ga	Gallium
GSZO	Gallium tin zinc oxide
GZO	Gallium zinc oxide

HMDS	Hexamethyldisilazane
I_D	Drain current
IGZO	Indium Gallium Zinc Oxide
In	Indium
I_{off}	Off current
$I_{on/off}$	On/off current ratio
I-V	Current-voltage
IZO	Indium zinc oxide
KE	Kinetic energy
M-OH	Metal hydroxides
N_2	Nitrogen gas
O	Oxygen
O_2	Oxygen Gas
O_I	Low energy O 1s peak
O_{II}	High energy O 1s peak
PEB	Post exposure bake
PR	Phototresist
q	Charge
RF	Radio Frequency
RT	Room Temperature
SCCM	Standard cubic centimeter per minute
Si	Silicon

SiO_2	Silicon Dioxide
Sn	Tin
SS	Subthreshold swing
SZO	Tin zinc oxide
TAO	Transparent Amorphous Oxide
TCE	Trichloroethylene
TCO	Transparent conducting oxide
Ti	Titanium
TFT	Thin Film Transistor
UV	Ultra violet
V_G	Gate voltage
V_{DS}	Drain to source voltage
V_o	Oxygen vacancies
V_T	Threshold voltage
W/L	Width / Length ratio
wt. %	Weight percent
XPS	X-ray Photoelectron Spectroscopy
XRD	X-ray Diffraction
Zn	Zinc
ZnO	Zinc Oxide

CHAPTER 1

INTRODUCTION

1.1 Overview

The continuous strive to make electronics more conveniently portable, improve consumer experience, and meet consumer demands compels manufactures to constantly explore new ways to reinvent and improve products. One way to accomplish this goal is to employ new materials that are capable of providing added features, functionality or durability to devices. Currently zinc oxide (ZnO) and ZnO based alloyed material systems are attracting great attention [1-8] due to their broad applicability in electronics and optics. The most mature applications of ZnO are optical coatings, varistors, and surface acoustic wave devices [9]. With the evolution of displays from passive to active matrix switching [10] ZnO based alloys are emerging as materials of interest in the flat-panel display industry. This progression is driven by the use of TFTs that function within the active matrix of the display as a pixel switch. As a new material for active matrix switching ZnO based alloys compete with the widely used [10] existing amorphous silicon (a –Si) TFT [9]. ZnO TFTs have the capability to outperform existing silicon TFTs in certain environments [9]. They also have a lower density-of-states (DOS), including that of tail and deep level states, than that of a-Si [11]. In addition, ZnO's high transparency is advantageous in markets for fully transparent electronics, such as transparent monitors/televisions and heads-up displays.

Within the market of transparent electronics, there is a developing interest in devices that are both transparent and flexible. Device production on flexible substrates is

complex in that they require material systems to be deposited at low temperatures, while maintaining or exceeding the functionality of non-flexible devices. Low temperature deposited ZnO based TFTs were demonstrated by various groups. The published literature on these devices reports on various binary and ternary oxide systems but to date only limited work has been devoted to GSZO [12-21], which has been identified as reasonable endeavor based on the low temperature requirements [17].

1.2 Motivation

In an effort to provide advanced support systems to soldiers in the field, Research Triangle International Incorporated and North Carolina Agricultural and Technical State University joined in collaboration for the development of flexible displays for U.S. Army mobile electronics [22]. The ultimate goal of this collaboration is the development of "more portable, environmentally rugged flexible displays than glass-based technologies which require extensive protection that adds cost and weight [22]." The flexible display backplane must consist of transistors capable of maintaining functionality on a flexible substrate; hence this work is geared towards the investigation of a novel material system compatible with low temperature deposition for the utilization of a flexible backplane.

1.3 Objectives

In this study, GSZO films have been investigated as a channel layer for thin film transistors. The focus of this work is as follows:

(a) To gain further insight into the effect of deposition and post deposition parameters on the characteristics of GSZO films and the performance of the resulting TFT

(b) To develop a fundamental understanding of how the variation of film components influence the electrical and optical stability of resulting devices.

A literature review is presented in chapter 2, on the work that has been carried out thus far regarding the properties and influencing factors of ZnO and ZnO based alloys on thin films and the resulting TFTs. The procedures for film deposition/characterization and TFT production/testing are described in chapter 3. Chapter 4 presents film characterization and device testing results. Chapter 5 presents an interpretation of the results described in chapter 4. Chapter 6 is a brief summary of the work presented. Chapter 7 discusses areas of further investigation for the expansion of this work.

CHAPTER 2

OXIDE BASED SEMICONDUCTORS AND THIN FILM TRANSISTORS

2.1 Oxide based semiconductors

A special class of oxide based semiconductors exists that are transparent (when deposited as thin films) and capable of yielding good conductivities. These oxides fall within one of two categories 1) transparent conducting oxides (TCOs) or 2) transparent amorphous oxide (TAOs). The category of oxide is determined based on the crystal structure of the material, where TCOs are polycrystalline and TAOs are amorphous. Both TCOs and TAOs possess distinct attributes that make them ideal for their respective applications.

2.1.1. Transparent conducting oxides

The ability to produce materials that possessed both high optical transparency and high electrical conductivity was believed to be impossible prior to 1907 [23]. Materials with high transparency typically have low conductivities [5] due to the difficulty of carrier doping resultant from their large band gap ($\geq$ 3.3 eV). With the discovery of TCOs, the realization of dually transparent and conductive materials was attained. The five principal constituents of transparent conductors are Zn^{2+}, Cd^{2+}, In^{3+}, Ga^{3+}, and Sn^{4+} [24]. The high transparency/conductivity duality of TCOs arises from the material's large band gap and charge compensating electrons promoted from defect energy levels to the conduction band minimum (CBM) [3]. The CBM of these materials is primarily composed of vacant s-orbitals with a spatial spread large enough to cause a direct overlap between the s-orbitals of the neighboring cations, and

therefore the electron effective mass is small in these oxides, making the material highly conductive [25]. The conduction path formed by s-orbital overlap is shown in Figure 2.1.

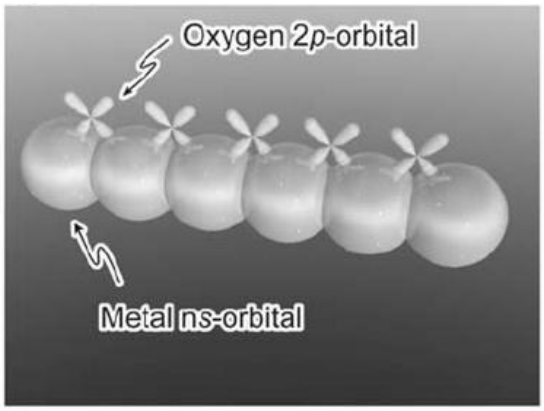

Figure 2.1. Schematic orbital of carrier transport paths for TCOs composed of post transition metal cations [26].

Amongst TCOs, ZnO is extensively investigated due to its direct wide bandgap of 3.4 eV at 300 K [8], low cost, elemental abundance, and promising electrical performance. The alloying of ZnO provides the opportunity to engineer TCO films for the enhancement of electrical, optical, and physical properties by altering their elemental compositions [27]. Unfortunately, due to the naturally high conductivity TCOs (ZnO, gallium zinc oxide (GZO)) are not optimally compatible with applications requiring current switching such as transistor active layers.

2.1.2. Transparent amorphous oxides

TAOs the amorphous and high resistance counterpart of TCOs not only allows for application in devices that demonstrate current switching, but also are capable of being deposited uniformly over large areas at low temperatures [28], making them highly desirable for the display industry and flexible electronics. The lack of crystal grains

means that the material is electronically homogeneous over very large areas and length scales [29]. Further, amorphous semiconductors are preferred over polycrystalline due to their degenerate band conduction that results in large mobility [26]. In addition, TAOs have a direct overlap among the neighboring metal orbitals that produce an optimal carrier transport path than that of covalent semiconductors in the amorphous state, such as a-Si. The TAO transport path is show in Figure 2.2. Common ZnO based TAOs alloys are indium zinc oxide (IZO) and indium gallium zinc oxide (IGZO). A fairly recently investigated material system gaining attention is gallium tin zinc oxide (GSZO).

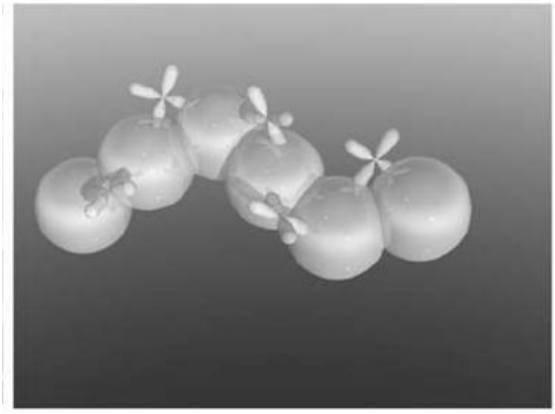

Figure 2.2. Schematic orbital of carrier transport paths for TAOs composed of post transition metal cations [26].

2.2 Zinc oxide and zinc oxide based materials

The following is a brief review of ZnO and ZnO based alloys containing In, Ga , and Sn in order to show the characteristics of these elements when incorporated into ZnO. As a result, some alloyed compositions may belong to TCO class of material, therefore the review will cover both TCOs and TAOs. For ease of comparison, tables

have been composed of the research findings that closely parallel the experiments performed for this work.

2.2.1. Zinc oxide

Research on ZnO, a II – VI compound semiconductor began in the 1930s [30]. It has a preferred hexagonal wurzite crystalline structure and a wide band gap of approximately 3.4 eV that enables it to appear colorless [2, 30]. Currently, ZnO is an area of interest for implementation in thin film transistor applications [31]. As a result there have been numerous investigations into the effect of deposition conditions and ambient on the characteristics of ZnO films.

Webb et al. [32] in their investigation of rf sputtered ZnO films found that resistivity is strongly dependent upon substrate temperature. They observe that increasing the temperature above 400 K (127 °C) resulted in an increase in film resistivity of the, whereas reducing the temperature to 350 K (77 °C) decreased the resistivity by a factor of two, and the further reduction of temperature resulted in a rapid increase in resistivity. In studies of an organometallic chemical vapor deposited films, a decreasing band gap was also observed to be resultant of increasing substrate temperature [33].

There is an expected deterioration in electrical performance of ZnO layers that are rf sputter deposited at low temperatures (RT), due to the lower crystalline quality and increased randomness of deposited atoms [34]. These properties can be improved with thermal annealing. Ahn et al. [34] observed a drastic decrease in the resistivity of the channel layer with annealing, where resistivities decreased from an order of $10^6\ \Omega$ cm

(as-deposited) to 10^3 Ω cm (350 °C annealed). Upon further annealing of 650 °C the resistivity decreased further to an order of 10^{-2} Ω cm.

The intentional incorporation of oxygen during film deposition was found to influence the resistivity and carrier concentration of ZnO. Jie et al. [35] demonstrated that crystallinity deterioration with increasing oxygen incorporation. It was also found that the increased oxygen results in lower sputtering efficiency of the target. Im et al. [36] found that the introduction of oxygen (in small amounts) during deposition resulted in a slight decrease in resistivity and upon higher incorporations the resistivity increased. They also observed a continuous decrease in carrier concentration with increasing oxygen, though the magnitude of change with increasing oxygen pressure decreased. This change in resistivity and carrier concentration is attributed to the reduction of oxygen vacancies (shallow donors) with increasing oxygen incorporation. Carcia et al. [37] observed that the films went from semiconducting (0.03 Ω cm) at low oxygen pressure to semi-insulating (10^6 – 10^8 Ω cm) at higher pressure, which is in agreement with Im et al. This phenomenon is believed to occur due to the films becoming closer to stoichiometric with fewer structural defects at higher oxygen incorporations, and therefore yielding higher resistivities.

Literature on ZnO mentions a photoresponse that yields an instability in the electrical characteristics of the film [38, 39]. Illuminated by monochromatic light causes the generation of electron-hole pairs, resulting in increased conductivity. For UV and visible excitation, the electron – hole pairs are generated from valence – conduction band as well as defect – conduction band transition [38]. The photoresponse is commonly

delineated into two parts [40]: a rapid and reproducible solid-state process for band-band transition, and a slow process with large response which is defect related. The former can be expressed by,

$$\boldsymbol{h\nu \rightarrow h^{+} + e^{-}}, \qquad \textbf{2-1}$$

where e and h represent electron and hole respectively. The latter, a two-step process, involves the absorption of oxygen in dark conditions,

$$\boldsymbol{O_2(g) + e^{-} \rightarrow O_2^{-}\,(ad)}, \qquad \textbf{2-2}$$

and the photodesorption of O_2 by capturing a photo-generated hole,

$$\boldsymbol{h^{+} + O_2^{-}\,(ad) \rightarrow O_2\,(g)}. \qquad \textbf{2-3}$$

Oxygen chemisorption at the surface affects the electrical parameters on ZnO films [1, 41].

2.2.2. Gallium doped zinc oxide and Gallium zinc oxide

Ga^{3+} has been reported to be amongst the best dopants for transparent conductive ZnO films, which is attributed to its radius being closer to and smaller than Zn^{2+} in comparison to other impurities [42]. Low temperature deposited GZO was observed to possess a lower resistivity than undoped ZnO signifying that part of Ga atoms lie in substitutional sites [42]. Kelly et al. [43] found the resistivites of ZnO:Ga to be significantly lower than that of ZnO, though the variation of Ga incorporation from 1 to 5 at. % showed no significant changes in resistivity. Lee et al. [43] shows that as the wt. % of Ga_2O_3 increases (from 0.6 to 5.7 wt. %) the crystallinity improves, and resistivity decreases and saturates.

Song et al. [44] observed that films carrier concentration and hall mobility increased with increase in deposition temperature from RT to 400 °C, with films deposited at 400 °C having the lowest resistivity. Films deposited at temperatures above 400 °C showed a significant increase in resistivity, along with a decrease in carrier concentration and hall mobility. Wu et al. [45] shows an increase in crystallinity with increased deposition temperature. In addition, it was observed [45] that increasing substrate temperature increases the Ga doping concentration along with the number of oxygen vacancies. Lee et al. [43] shows that at Ga_2O_3 incorporations of 3 wt. % and beyond there is an increase in optical bandgap with increasing deposition temperature. Nagarani et al. [46] shows an increase in crystallinity and a decrease in resistivity with an increase in deposition temperature.

Ma et al. [47] illustrates the dependence of the resistance of a ZnO:Ga on the Ar/O_2 gas ratio used during deposition. Here it was found that a minimum resistivity is achieved at a ratio of 15:1, beyond which the resistivity increases. With increasing Ar/O_2 gas ratio (lower O_2 partial pressure) the oxygen amount was too low to oxidize all of the sputtered metal atoms, thus the film became sub-stoichiometric and a large number of oxygen vacancies were created there creating a high carrier concentrations. It was also found that the optical bandgap of the film increased with increasing Ar/O_2 gas ratio.

Martins et al. [48] corroborates Ma's finding and adds that increased oxygen begins to compensate vacancies and reducing carrier concentration, and thereby increasing resistivity. Martins continues to report that ZnO films are more sensitive to oxygen pressure than films based on binary metal oxide alloys. It was found that

electrical conduction in oxide semiconductors is highly dependent on its iconicity and hence on the number of vacancies (as a source of free carriers). In ZGO Ga forms a shallow bound state below the ZnO conduction band edge, but at high concentrations, this forms a continuous band with the ZnO in the alloy.

Wong et al. [49] observed three regimes that show different reactions to oxygen pressures. The first regime (low oxygen 10^{-6} to 10^{-4} Torr) showed no change in the carrier concentrations, but improvement in mobility, and a reduction in resistivity. This is attributed to the removal of deep-level oxygen vacancy charge defects (2^{+} state). The second regime (mid-oxygen 10^{-4} to $5x10^{-3}$ Torr) showed slight decreases in both carrier concentration and mobility with increasing oxygen pressure. This is attributed to the formation of oxygen interstitials, which introduce states in the lower part of the band gap that can accept two electrons, thereby decreasing the electron concentration. The third regime (high oxygen > $5x10^{-3}$ Torr) shows a drastic decrease in mobility and a large increase in resistivity. This is attributed to a reduction in the diffusion path length for the absorbed atoms which leads to a loss in mobility through grain boundary scattering.

Huang et al. [50] shows that annealing in vacuum yields the lowest resistivity, followed by oxygen, then Nitrogen. They also show a decrease in resistivity with increased annealing temperature for oxygen and vacuum ambients, where nitrogen has an initial increase in resistivity followed by a steady decrease.

2.2.3. Indium zinc oxide

IZO tends to favor the deposition of a material with a disordered structure, leading to the formation of an ionic amorphous oxide semiconductor [29]. Nunes et al. [51]

illustrates that as the incorporation of In increases in ZnO the film becomes amorphous. In^{3+} is said to form shallow donor states in ZnO [48]. It was shown that upon incorporating 1 at. % In into ZnO the resistivity decreased from 0.14 to $9.6x10^{-3}$ Ω cm, and with a 2 at. % incorporation to $6.3x10^{-2}$ Ω cm [52]. It was shown by Park et al. [53] that IZO when the film content of Zn is greater than 60% for RT deposited films they show a crystalline behavior. Films tested by Park that were grown at 300 °C all showed crystalline behavior for all Zn incorporation percentages. Park also shows a decrease in bandgap energy with increasing Zn incorporation. By adjusting the Zn/In ratio Kumar et al. [54] was able to vary the absorption edge from approximately 2.65 eV to 3.0 eV. The Martins group [55] observed that unlike ZnO where the only scattering mechanism is ionized impurity, causing the mobility to increase as the net carrier concentration decreases, IZO films exhibit a reverse behavior. This behavior is explained by the Hall mobility being limited by trapping at localized states and that oxygen vacancies contribute to the enhancement of conduction electrons [56]. Wang et al. [57] determined the main influence on the resistivity of the films were the oxygen partial pressure. Martins et al. [48, 55, 58] confirms this statement with their work by showing a decrease in resistivity with decreasing oxygen partial pressure. Naghavi et al. [59]observes the influence of deposition temperature on the crystallinity of the films. Here they find that films deposited at room temperature and 100 °C to be amorphous while films deposited at higher temperatures become increasing more crystalline. They also note changes in the film composition with respect to the oxygen pressure. This is attributed to an increase of the oxygen pressure, which regulates the velocity distribution of the various components.

Kim et al. also investigates the effect of deposition temperature, and shows that films became crystalline at temperatures above 200 °C. They also showed an evolution of crystallinity, where the layers closest to the substrate were amorphous and the layers beyond 50nm away were crystalline. Dehuff et al. [60] illustrates the effect of post-deposition annealing on transistor V_{on} and V_T values by showing the mode of operation difference between TFTs with channel layers annealed at 600 and 300 °C. The 600 °C device operated in depletion mode where the 300 °C device is enhancement mode. Goncalves et al. [61] shows a drastic increase in resistivity of their annealed sample versus the as-deposited. This increase in resistivity was accompanied with a decrease in carrier concentration and mobility. Ito et al. [62]shows the effect anneal with respect to the crystallinity of the film. Their XRD patterns show that as annealing increases beyond 400 °C it changes from amorphous to crystalline. They also show upon annealing at various temperatures films annealed in air show an increase in resistivity where those annealed in vacuum show a slight decrease. This is attributed to a decrease in carrier concentration for those annealed in air and a slight increase in concentration for those in vacuum. Ku et al. [63] shows a decrease in resistivity with increasing annealing temperature up to 400 °C for films with 1% oxygen incorporation, beyond 400 °C there is an increase in resistivity. The samples with less than 1% oxygen show no significant change in resistivity. The increases in resistivity with annealing was also confirmed by Jeon et al. [64], which is attributed to the filling of oxygen vacancies. Jeon et al. also shows a decrease in band edge with annealing. Lee et al. [65] observed an unexpected decrease in resistivity with increased annealing, described to be due to the low (200 °C)

annealing temperature used. At low temperature the kinetics of diffusion of oxygen into the film is likely to be extremely slow, and instead it was proposed that a structure relaxation occurs which generates carriers when the as-deposited film is annealed.

2.2.4. Indium gallium zinc oxide

Multicomponent oxides lead to a better control on vacancies, lower off currents, and a lessened sensitivity to the state of oxidation [48]. This is done by reducing the sensitivity to oxygen and exploiting the beneficial traits from each element incorporated into the system.

2.2.4.1. Oxygen

It was observed by Takagi et al. [66]that the transmission spectra of a-IGZO films differ according to carrier concentrations, and that the concentrations were variable by altering the oxygen pressure during deposition. Yabuta et al. [67] shows that electrical conductivity decreases as the oxygen partial pressure increases. Shin et al. [68] reports that the number of defect states (or tail states) that absorb the photon energy is believed to decrease with the oxygen content to reach a minimum. This accounts for the reduction in the absorption edge with increased oxygen. Na et al. [69] determined that IGZO films are semi-insulating when deposited with oxygen incorporations greater than 1.47%. Park et al. [70] suggests that unlike absorbed oxygen molecules, forming a depletion layer below the active surface, absorbed water molecules form an accumulation layer. Kwon et al. [71] states that sputtering of oxygen during Ar ion bombardment causes a-IGZO to become oxygen deficient near the surface, which can effect carrier concentration in two

ways (1) induce n-type free carriers near the conduction band and (2) increase the In^{3+} content.

2.2.4.2. Deposition/Annealing Temperatures

Chen et al. [72] shows films begin to become crystalline at deposition temperatures of 400 ˚C or greater. They also show that after an initial drop in resistivity when increasing deposition temperature from RT to 200˚C, resistivity remains relatively constant upon further increase.

2.2.5. Tin zinc oxide

Ko et al. [73] shows that films demonstrate a decrease in resistivity with increased annealing temperature as long as the films remain amorphous, but once they begin to crystalize resistivity increases sharply. The crystallization temperature was shown to be above 200 °C for films deposited with an rf power of 10 W and below, and 450 °C for those deposited at 20 W. Jayaraj et al. [74] shows that films are amorphous until annealed at temperatures of 450 °C and above. At this point the films crystalizes partially, given rise to crystalline phases of the simple oxides ZnO and SnO_2.

2.2.6. Gallium tin zinc oxide

Unlike, previously mentioned material systems the high resistivity of GSZO hinders the use Hall measurement techniques. The characterization of the film is therefore typically done through AFM, XRD, transmission/reflectance, and XPS. Hall measurements show film resistivity of as-deposited samples to be of the order of 10^{10} Ω cm, with a Hall mobility of 5 cm^2/ V s AFM demonstrated no significant change in surface roughness with annealing temperature [15]. XRD showed stability of the

amorphous structure up to 600 °C for an ALD deposited film [15] and up to 2 % oxygen partial pressure for sputter deposited samples [20]. The increased percent incorporation of Ga into ZSO was shown by Palmer et al. [12] to be proportional to the size of the optical band gap of the resultant GSZO. This influence of Ga incorporation on the optical band gap was also observed by Kim et al. [21]. Ogo et al. [15] upon analysis of absorption data, deduced from transmission and reflectance measurements showed the presence of extra energy states formed in the subgap region. The subgap absorption decreases on increasing the annealing temperature [14, 15]. XPS analysis of the films yield varied results. Fortunato et al. [13] observed a surface enrichment of Ga and Sn with increased annealing temperature, along with an increase in the O 1s ratio of oxide/hydroxide. With respect to oxygen incorporation during deposition Kim et al. [20] shows a decrease in the atomic concentration of Sn and a surface enrichment of Zn with increasing oxygen partial pressure.

2.3 Metal oxide semiconductor field effect transistors (MOSFET).

The MOSFET is a vital component in the production of integrated circuits due to its capability to control current [75]. Its basic structure is shown in Figure 2.3. The W and L in the figure represent the width and length of the transistor's channel region. The type of MOSFET is determined by the majority carriers of the doped the source and drain regions, where a device with n+ source/drain regions yield a n-type transistor and p+ source/drain regions a p-type. Both n- and p-type devices have two modes of operation, enhancement and depletion mode. The two modes of operation differ in that the channel is not former in enhancement mode devices at zero gate to source voltage (V_{GS}), where

depletion mode devices have a former channel zero V_{GS} [75]. The application of gate-to-source bias induces an electric field in the oxide layer that penetrates the semiconductor [75]. In the case of n-channel enhancement transistors the electric field produced by a positive applied V_{GS} greater the V_T attracts electrons to the oxide – semiconductor junction producing a conductive channel between the source and drain regions, and a negative V_{GS} repels electrons from the channel region. A positive V_{GS} for n-channel depletion transistors enhances the already formed channel where a V_{GS} more negative than V_T compensates the charges of the normally formed channel. A cross sectional view along with the typical output and transfer characteristics of the transistor types and modes of operation are shown in Figure 2.4. The application of voltage across the source and drain causes the mobile charges in the channel to flow, producing a current.

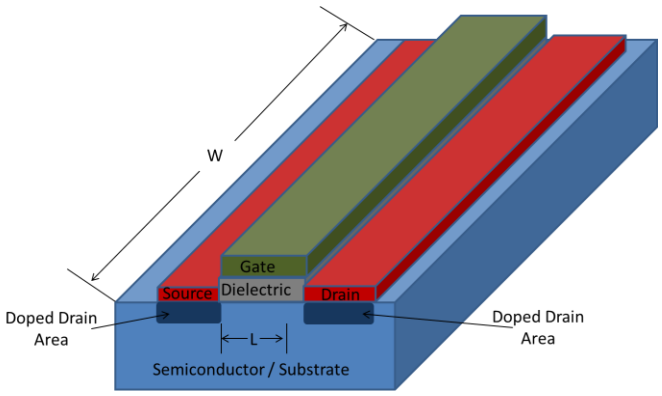

Figure 2.3. Basic structure of a MOSFET.

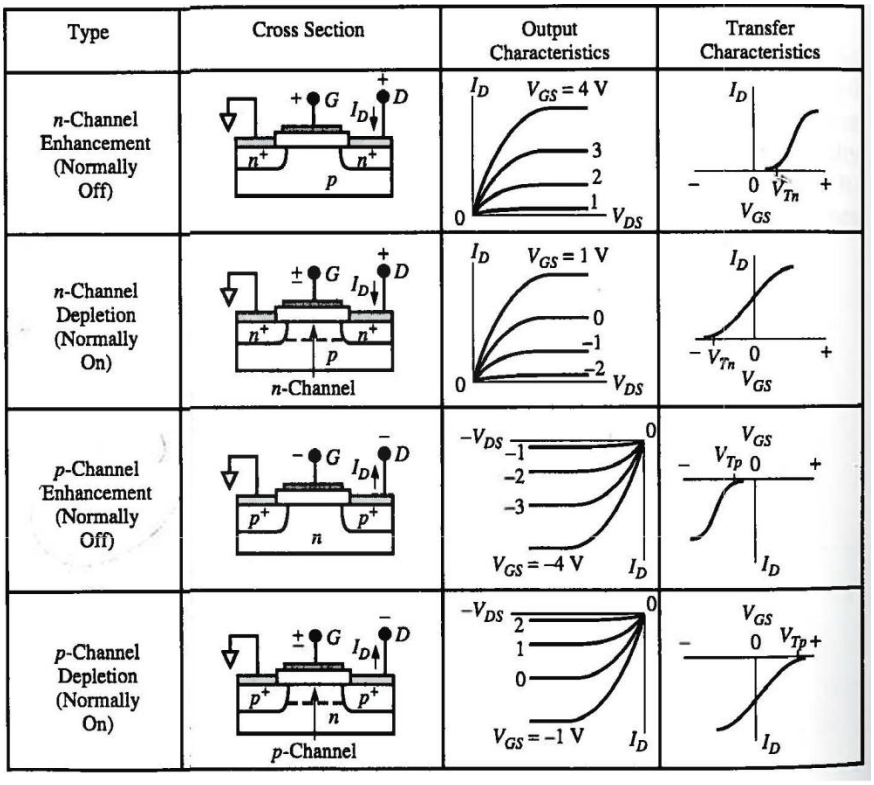

Figure 2.4. Cross sections, output characteristics, and transfer characteristics of MOSFETs [76].

The current – voltage relationship for both n- and p-channel transistors is expressed in equations [75, 76]. Transistors are described to be in the linear region when applied drain to source voltage (V_{DS}) is less than the saturation value of V_{DS} ($V_{DS(sat)}$). When V_{DS} is greater than or equal to $V_{DS(sat)}$ the transistor is operating in the saturation region, where the maximum achievable I_D has been reached, see Figure 2.5. Equation 2-4 shows the calculation for determining the value of $V_{DS(sat)}$. Equations 2-5 and 2-7 are for the linear operation region where Equations 2-6 and 2-7 are for saturation.

$$\boldsymbol{V_{DS(sat)} = V_{GS} - V_T}\,, \qquad \textbf{2-4}$$

$$\boldsymbol{I_D = \frac{W}{L}\frac{\mu_n C_{ox}}{2}[2(V_{GS} - V_{TN})V_{DS} - V_{DS}^2]}, \quad \textbf{for } V_{DS} < V_{DS(sat)} \qquad \textbf{2-5}$$

$$I_D = \frac{W}{L}\frac{\mu_n C_{ox}}{2}(V_{GS} - V_{TN})^2, \quad \text{for } V_{DS} > V_{DS(sat)} \qquad \textbf{2-6}$$

$$I_D = \frac{W}{L}\frac{\mu_p C_{ox}}{2}[2(V_{SG} + V_{TP})V_{SD} - V_{SD}^2], \quad \text{for } V_{SD} < V_{SD(sat)} \qquad \textbf{2-7}$$

$$I_D = \frac{W}{L}\frac{\mu_p C_{ox}}{2}(V_{SG} + V_{TP})^2, \quad \text{for } V_{SD} > V_{SD(sat)} \qquad \textbf{2-8}$$

In the above current equations μ_n and μ_p are the mobility of electrons and holes respectively, C_{ox} is the capacitance of the oxide layer, and W/L the width : length ration of the channel region. The threshold voltages of the n- and p-channel transistors are distinguished by their subscripts, and for p-channel devices the "SG" & "SD" subscripts represent source to gate and source to drain respectively.

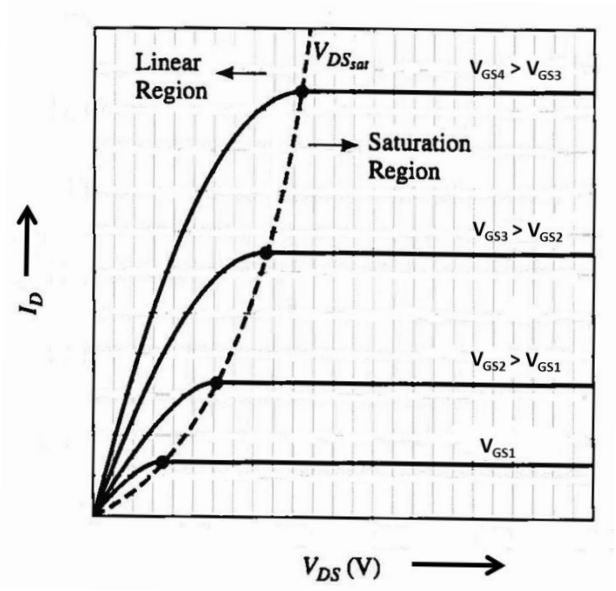

Figure 2.5. Output curves for n-channel enhancement mode MOSFET.

2.4 Thin film Transistors

The first TFT was produced in 1962 by Weimer [77, 78]. The basic working of TFTs, like traditional MOSFETs, is that charge density in the active layer and thus its conductivity can be modulated by the bias applied at the gate [79]. The charges are then

injected and collected by the source and drain electrodes, respectively [79]. Due to these similarities it is common practice to specify the electrical characteristics of a TFT using the MOSFET model equations [80]. The benefit of TFTs as opposed to the typical MOSFET is the structure allows for low temperature production of these devices. The TFT structure differs from the conventional MOSFETs where the semiconductor material is the substrate. The structure of a top gate TFT is shown in Figure 2.6.

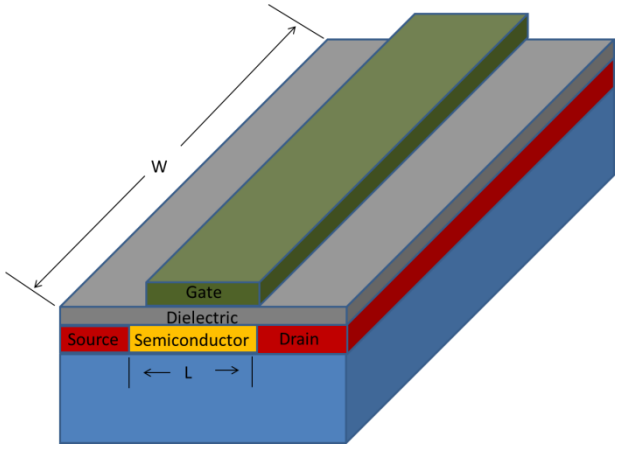

Figure 2.6. Top gate TFT structure.

2.5 ZnO and ZnO based TFTs

2.5.1. ZnO TFTs

The first ZnO TFT was proposed in 1968 by Boesen et al. [81, 82], and has become a highly researched area, and has expanded to include doped ZnO and ZnO based alloys [6, 8, 83]. The utilization of these materials are ideal for TFT production due to the low costs, suitability for semiconductor applications, mature manufacturing processes, low temperatures manufacturing, and high transparency. The first ZnO transistor was reported in 1968 by Boesen et al. [84], and was found to have relatively large values of surface states and/or insulator charge that could be improved with “more sophisticated

processing." Since 1968, with advances in the transistor fabrication process, it is now possible to deposit high quality films at /near room temperature [85], thereby improving the device performance. Some important factors in the processing of the active layer are the deposition conditions (temperature and ambient) and annealing temperature. It was found that these factors could drastically alter the behavior of the resulting device.

Regarding deposition temperature Kwon et al. [86] observed that devices produced with ZnO channel layers deposited at 130 °C did not exhibit saturation and behaved more like a metallic than a semiconductor. They attributed the metallic behavior to a higher carrier concentration invoked by the higher deposition temperature (vs. room temperature). The higher carrier concentration was illustrated by the decrease in V_T as the deposition temperatures were increased.

The effect of deposition ambient, specifically oxygen incorporation on ZnO TFT performance was realized by Carcia et al. [37].

Ahn et al. [34] reports that the I-V characteristics of their device with 650 °C annealing showed metallic behavior with an almost linear curve.

As a means of evaluation of the quality and reliability of the ZnO layers and the resulting TFTs photoexcitation and electrical stress measurement techniques are employed.

Bae et al. [87] reports on the photodetection capability of ZnO TFTs, noting that the largest photoelectric effect resulted from ultraviolet illumination, while red photons were shown to be ineffective. The ineffectiveness of the red photons was described to be attributed to the natural midgap states induced by Zn vacancies or O interstitials that are

known to exist near 2.3 eV below the conduction band of ZnO polycrystals [33, 36, 87]. In addition, the photoelectric ratio was observed to be larger in the depletion states [87]. Murphy et al. [38] confirms the presence of deep traps levels (near 2.3 eV) in ZnO where a "green band " peaking at 2.35 eV (530 nm) is observed through photoluminescence spectra. They also note that deep traps present at the ZnO surface are a primary source of the photoconductive response associated with the adsorption of oxygen or hydroxide groups on the ZnO surface. Lee et al. [88, 89] related the magnitude of threshold voltage shift to the density of traps present in the device active layer. They deduced that the density of interface traps measured by the V_T shift is only valid in cases without significant bulk trap densities, and when bulk traps are significant the sub-threshold swing (SS), mobility (μ), and I_{off} will change in addition to V_T. The relationship between the shift in V_T with photoexcitation and the density of trap states was expressed as follows:

$$\boldsymbol{D_{it}(E_c - \varepsilon) = \frac{C_{ox}}{q}\frac{\partial V_T(\varepsilon)}{\partial \varepsilon}} \qquad \textbf{2-9}$$

where $D_{it}(E_c - \varepsilon)$ is the DOS (cm^{-2} eV^{-1}) with respect to E_C, C_{ox} is the dielectric capacitance, and $\frac{\partial V_T(\varepsilon)}{\partial \varepsilon}$ is the change in V_T with respect to ε. Using the above equation 2-9 it is possible to calculate the density of trap states at specific energy levels.

With any device produced it is important that its performance remains consistent throughout the expected lifetime of the product in which it is implemented into. For this reason stability testing is essential when characterizing the performance of devices. Two mechanisms were identified to be responsible for the instability in TFTs under gate bias. The first being defect creation in the channel material, and the second is charge trapping

in the gate insulator/channel interface [90-92]. The former is said to dominate at lower field, while the latter dominates in large stress fields [93]. Cross et al. [92] observed that the application of positive bias resulted in the displacement of the transfer curve in the positive direction and the application of a negative bias displaced the curve in the negative direction. Cross et al. goes on to state, the shift of V_T is evidence of charge trapping being dominant in the instability of the TFT, which the group justifies due to the initial state recovery of the device without any annealing to release the trapped charges. In addition, they state that a low stress bias, temporary charge trapping at/near the channel/ insulator interface seems to dominate; temporary defect creation becomes increasing evident at high biases and long stress times. Navamathavan et al. [94] reports on a ZnO TFT produced with a 200 nm active on glass/ITO/SiN_x. The stability of the TFT was examined through the device performance after electrical gate bias stress. Devices were stressed for duration of 200 s under a gate bias of +10 and -10 V. The TFT transfer characteristics prior to electrical stress were compared to that after stress to determine the stability of the device. A horizontal shift towards the left was observed, suggesting the presence of trapped charges at the semiconductor/dielectric interface. A change (3 orders of magnitude) in off current (I_{off}) was also observed indicating that leakage current increases with bias stress. It was determined that the magnitude and duration of applied electrical is directly related to the amount of degradation experienced by the TFT. Flewitt et al. [29] observed a minimal change in V_T of 0.2 V during a stress period of 10^5 s, with a 15 V V_{GS}. The minimal V_T shift is attributed to a high quality gate dielectric.

2.5.2. GZO

Verma et al. [95] investigated the environmental effects on GZO bottom gate TFTs and observed a 2 order of magnitude decrease in current of the device after a 10 day storage period. This was attributed to oxygen vacancies and zinc dangling bonds at the surface that act as active sites for the absorption of oxygen molecules present in atmosphere. The absorption of oxygen on the surface forms a depletion layer in the thin film channel and overall performance of the device decreases.

2.5.3. IZO

Barquinha et al. [96] discusses the effects of photoexcitation and demonstrates a negative shift in V_T and a decrease in $I_{on/off}$ as excitation wavelength increases. Regarding gate stress it was proposed [29] that the accumulation of free electrons in the channel region upon application of the gate bias will result in deep defect states becoming occupied with time. Once occupied, they will not act to trap further electrons, and so the average lifetime of free electrons in the conduction band will increase. Liu et al. [97] showed the effect of stress in both positive and negative stress in air, showing a positive and negative shift in V_T respectively. This was also illustrated by Xu et al. [98]. The positive shift was attributed to absorbed oxygen from the ambient atmosphere, where the negative shift is attributed to an increased number of holes in the channel region and absorbed moisture from the atmosphere to form positively charged H_2O^+. The resultant buildup of positive space charges H_2O^+ induce conduction electrons in the a-IZO TFT channel, negatively shifting V_T.

2.5.4. SZO

Kelly et al. [52] showed that Ga and In incorporation into ZnO showed blue shifts in the absorption edge with relation to undoped ZnO while Sn-doped ZnO showed a red shift. Sn-doped ZnO was shown to have an increased resistivity as opposed to undoped ZnO. In addition, the incorporation of Sn shows a resistivity of 1 – 4 orders of magnitude higher than that of comparable Ga and In incorporations. Adversely, Hoffman et al. [99] showed a negative shift in V_{on} with increasing Sn incorporation, signifying a reduced resistivity. It is to be noted that Hoffman et al. [99]also observed that the TFT performance is influenced by numerous additional process-related and structural parameters. In an comparison of rf and dc sputtering [100] it was observed that rf sputtering was strongly dependent on oxygen flow rate during deposition and a negative shift in V_{on} was observed with increased annealing for rf where none was observed for dc. Görrn et al. [101]observed that devices with Zn contents below 36% and above 65% tend to exhibit positive shifts of V_T when stressed , where as transistors transistors with nearly equal fractions of Zn and Sn show negative shifts of V_T. Processing temperature was identified by Görrn et al. [102] as the dominating parameter for light sensitivity of the resulting device, with the sensitivity increasing with decreasing deposition temperature. Görrn et al. [102]also showed a negative shift in V_{on} and an increase in I_{off} were shown for increasing light intensity and decreasing wavelength. The defect states responsible for V_{on} shifts are situated near the semiconductor dielectric interface while the increase of the off current is caused by states in the volume of the oxide semiconductor [102]. Jeong et al. [103]observed positive shift in V_T with positive stress

voltages and no significant shift for negative stress voltages signifying positively charged oxygen vacancies can behave as acceptor-like traps that are responsible for a positive shift [70]. The absence of the negative shift indicates that the electron concentration is predominant over the hole concentration in the ZTO. Chen et al. [104] shows a positive shift in V_T with stress time that appears to saturate above 1000 seconds. Nayak et al. [105] shows a positive shift in V_T when devices were stressed with a positive gate voltage and a negative shift for negative gate stress.

2.5.5. IGZO

In IGZO films Kang et al. [106] delves into the investigation of the effect of oxygen by observing the shift in transfer curves of devices that are produced in increasing oxygen deficient and rich conditions. Kang's results show a shift in on voltage in negative direction as the deposition ambient becomes increasingly oxygen deficient, and a positive shift in V_{on} as the deposition ambient becomes oxygen rich. Barquinha et al. [107] shows that oxygen content has a greater effect on the transfer characteristics of non-annealed devices than that of annealed. They also show that as oxygen incorporation increases the degradation of devices characteristics. They observed the maximum incorporation before degradation to be 0.63%. Chiang et al. [108] reports findings similar to that of Barquinha regarding degradation of characteristics with increased oxygen pressure. Shin et al. [68] reports that V_T increases with increasing oxygen content, due to the suppression of the carrier concentration generated by the oxygen vacancies in the active layer. Further, it was observed that the number of defect states (or tail states) that absorb the photon energy is believed to decrease with the oxygen content to reach a

minimum. This accounts for the reduction in the absorption edge with increased oxygen. Na et al. [69] determined that IGZO films are semi-insulating when deposited with oxygen incorporations greater than 1.47%. Park et al. [70]suggests that unlike absorbed oxygen molecules, forming a depletion layer below the active surface, absorbed water molecules form an accumulation layer. Barquinha et al. [109] shows a positive shift along the V_G for V_{on} as oxygen pressure is increased. The TFT active layer was deposited in an Ar ambient. Kwon et al. [71] states that sputtering of oxygen during Ar ion bombardment causes a-IGZO to become oxygen deficient near the surface, which can effect carrier concentration in two ways (1) induce n-type free carriers near the conduction band and (2) increase the In^{3+} content.

2.5.5.1. Stress

Suresh et al. [110] determined that V_{on} can also be engineered to produce enhancement and depletion mode devices by varying the thickness of the channel layer. In another report Suresh et al. [111] investigated the stability of IGZO TFTs when electrically stressed. The Suresh group observed a positive shift in V_{on} along the V_G axis. This shift was attributed to the trapping of negative charge carriers in the semiconductor/dielectric interface since it was not accompanied by a change in saturation mobility or subthreshold swing. Lee et al. [112] tested the stability of the TFT by applying a stress voltage to the gate and observed a shift in V_{on} in the positive V_G direction. These devices were deposited in an Ar environment with oxygen incorporation. Suresh et al. [113] shows a shift in the negative V_G direction of V_{on} after stressing the gate. Cho et al [114] shows a positive shift in V_{on} along V_G after stressing the gate. The

TFT active layer was deposited in an Ar ambient. Hoshino et al [115] shows a positive shift in V_{on} along V_G after stressing the gate.

2.5.5.2. Photoconduction

Chuang et al. [116] reports on the effect of photosensitivity of the active layers, observing a shift in the negative V_G direction of V_{on} as photon wavelength is decreased. Jeong et al. [117] reports that a reducing chamber pressure for deposition can improve sub-threshold swing and mobility. Kim et al. [118] investigated photoconduction and found that V_{on} shifts in the negative V_G direction as photon wavelength is increased.

2.5.5.3. Aging

Lim et al. [119] observed the effect of aging on the performance of the TFTs. They noted a slight migration by 150 mV in the positive V_G direction of V_T after 500 h aging time, and a change of only ±1.5% for the same time period in another report [120].

2.5.5.4. Deposition/Annealing Temperatures

Moon et al. [121] illustrates the dual effects of substrate temperature and annealing temperature. Here it was determined that both cause a negative shift along the V_G axis for V_T. In addition, heated depositions have essentially the same influence on as-deposited devices as low temperature annealing (100˚C) on RT deposited samples. Further, high temperature annealing (400˚C) causes extreme negative V_T shifts in devices with channel layers produced under heated deposition conditions. Jeon et al. [122] shows an increased negative shift in V_T as annealing temperature is increased.

2.5.6. GSZO

The emergence of GSZO's implementation as a channel layer arose from the necessity to find a replacement for In^{3+} within IGZO. Upon investigation characteristics of GSZO TFTs were found comparable to that of IGZO devices, showing Sn^{4+} to be a suitable replacement [13, 15, 18]. Table 2.1 high lights the transistor characteristics achieved when using GSZO active layers.

Table 2.1. GSZO TFT electrical characteristics

Author	Deposition Temp. (˚C)	Annealing Temp. (˚C)	Mobility (cm^2/ V s)	V_T (V)	$I_{on/off}$	SS (V/decade)
Fortunato, et al. [13]	RT	300	18.1	6.5	$6x10^7$	0.62
Ogo, et al. [15]	RT	300	$5x10^{-3}$	2.5	$1x10^3$	11.5
Jeong, et al. [18]	RT	200	1.2	3	$1x10^6$	1.5

Fortunato et al. [13] report on the effects of both deposition and annealing temperature on electrical performance of TFTs and found devices annealed at 300˚C demonstrated a drastic improvement. Further, devices subjected to heated deposition illustrated better electric characteristics than that of comparable room temperature produced TFTs. Ogo et al. [15] also investigated the effect of annealing and related annealing temperature not only to electrical characteristics, but also the optical absorption spectra. Here electrical characteristics dependence on annealing is in agreement with the findings of the Fortunato [13] group, stating that increased annealing temperatures improve TFT performance. Regarding absorption data, Ogo [15] shows a reduction in tail intensity as

annealing temperature increases. Continuing the GSZO TFT characterization Jeong et al. [18] reports the effect of gate bias stress on V_T stability. It was found that increased stress voltage results in an increased change in V_T, with the maximum ΔV_T of 3 V occurring at the largest stress voltage of 40 V.

2.6 Oxygen Absorption/Desorption

Oxidation physically means that oxygen attracts electrons, for instance from the surface of the solid. It remains then tightly bound as a charged ion at the surface. The bound electron is then no longer "free" for the solid and the resulting oxygen species can exist in various forms such as O^{2-} , O^-, or $2O^-$ as shown in Equation 2-10. As a result of charge transfer, a depletion layer is formed beneath the films surface, creating an active backchannel [123]. The V_T of devices as a result is dependent on absorption on this O_2 created backchannel. The absorption process is illustrated in Figure 2.7.

$$\mathbf{O_2(gas) + e^- = 2O^-(solid)} \qquad \mathbf{2\text{-}10}$$

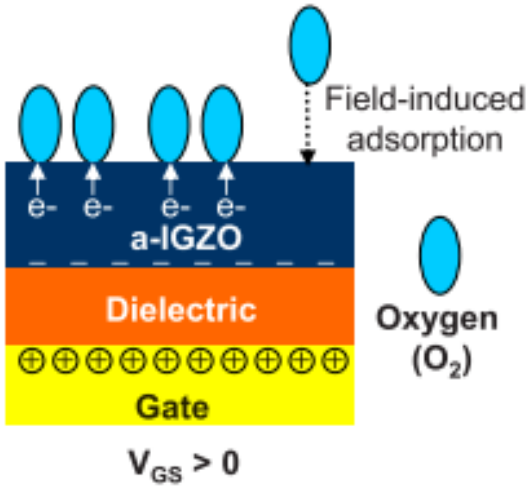

Figure 2.7. Field induced absorption of oxygen [123].

2.7 Photoexcitation

According to the photoelectric effect, first observed in 1887 by Heinrich Hertz, monochromatic light can be used to liberate electrons from the surface of a solid [75]. Application of the effect allows for use of optical techniques to identify defects and characterize materials. Photoexcitation, as discussed in this work relates to the excitation of electron from trap states within the channel / dielectric interface. The concept behind this is that the photoexcitation causes the trapped charge carriers in the gap states between CBM – ε and CBM to be released into the CB.

2.8 XPS Studies on ZnO Based Alloys

In the literature [18, 87, 124-126] the typical O1s peak is fit by three nearly Gaussian curves center approximately at 529.8, 531.3, and 532.4 eV. The high binding energy component is usually attributed to the presence of loosely bound oxygen on the surface of the film resultant from chemisorbed oxygen impurities. The medium energy peak is associated with oxygen ions in oxygen deficient regions with in the film. Lastly, the low binding energy peak is attributed to oxygen ions bonded to the cations within the material.

2.8.1. ZnO

Ogata et al. [127] demonstrates the effects of prolonged exposure to air on the O 1s peak of ZnO films. They show that films exposed to air longer than 3 months possess an increased O-H peak in the O 1s spectra. The dependence of the shape of the O 1s peak on oxygen partial pressure during deposition was investigated by Jang et al. [128], where

it was found that the peak attributed to oxygen deficiencies in the structure decreased with increased oxygen.

2.8.2. SZO

The observation of the deconvoluted O 1s peak by Oh et al. [129] showed the presence of both oxygen atoms in the vicinity of an oxygen vacancy at the lower binding energy and M-OH species at the higher. Dissimilar to the Oh et al., Jain et al. [130] fit the O 1s peak with three Gaussian components. They observed a decrease in peaks attributed to lattice and free hydroxyl group oxygen, and an increase in oxygen deficient peak with annealing. In addition they contributed the presence of SnO to lattice oxygen deficiency.

2.8.3. IGZO

Shin et al. [68] found that the concentration of Ga increases, In decreases and Zn remains constant with increasing oxygen content. This finding was reiterated by Cho et al. [131], but adversely Zn was observed to decrease as oxygen was increased. It was found [122, 132] that the relative concentration of oxygen vacancies (identified in the O1s peak) in the film to increase with annealing temperature. Kim et al. [133] found the ratio of Ga/Zn to be inversely proportional to ratio of oxygen vacancies to oxygen ion bond with Zn, Ga and In ions. With the continued increase of Ga, they found the film to become semi-insulating. Yao et al. [126] observed an increase in threshold voltage and subthreshold swing with increased oxygen content. Cho et al.[131] showed Zn to decrease with increased annealing temperature while Ga increases. Chen et al.[134] observed that with the increase in oxygen content of the sputtering gas mixture, the surface non-lattice oxygen ions (oxygen vacancies increase) percentage also increased,

and metal bound oxygen decreases. This result indicates that the oxygen ions are not completely reoxidized during deposition, and that these ions become weakly bound oxygen species on the film's surface. Chen et al.[135] shows an increase in Ga concentration. Trinh et al.[125] describes a reduction in oxygen vacancies with annealing, due to surface compensation with O atoms.

2.8.4. GSZO

Fortunato et al. [13] found a surface enrichment of Ga and Sn with annealing temperature. Kim et al. [20]found no chemical shift resulting from the chemical state variation due to the addition of O_2 gas, but did observe the peaks to shift to a slightly higher binding energy with increasing the O_2 ratio.

CHAPTER 3

FABRICATION AND CHARACTERIZATION TECHNIQUES

3.1 Oxidation

Prior to film deposition a silicon dioxide layer was grown onto the Si wafers as an insulting barrier (dielectric). This growth process (oxidation) is performed within a furnace by heating the silicon wafers to a high temperature (900 to 1200 °C) in the presence of pure oxygen. Silicon dioxide is formed through a chemical reaction occurring at the silicon surface (Equation 3-1). For dry oxidation the reaction is identified as

$$\boldsymbol{Si\ (solid) + O_2\ (vapor) \rightarrow SiO_2\ (solid)} \qquad \textbf{3-1}$$

The silicon surface is consumed as the oxide grows; resulting in the final oxide layer being approximately 54% above the original surface of the silicon and 46% below the original surface, see Figure 3.1.

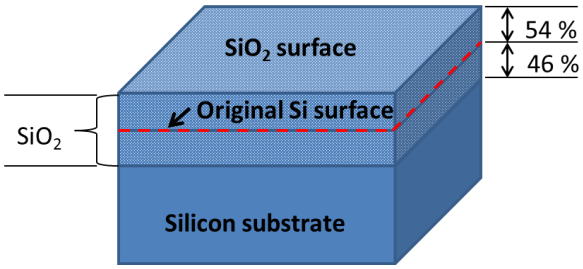

Figure 3.1. Formation of Silicon dioxide on the surface of a silicon wafer.

3.2 Film Deposition

3.2.1. RF Magnetron Sputtering Overview

Sputtering, a type of physical vapor deposition, proceeds according to the following steps: 1) the material to be deposited is physically converted to vapor phase, 2) the vapor is transported across a region of reduced pressure, 3) some of the vapor produced can

condense to form a thin solid film on the substrate [136]. The rf sputtering process is performed within a chamber that is placed under vacuum then re-filled with a gas at low pressure of the order of 1 – 10 mTorr. Within the chamber there are two electrodes driven by an rf power source, which ionizes the gas between the electrodes, thereby generating the plasma [137] [138] . Argon is generally the processing gas of choice for plasma generation due its non-reactivity with the elements frequently sputtered, ease of availability, and mass (allowing for good sputtering yields) [136]. The plasma is sustained by the ionization caused by secondary electrons emitted from the cathode due to ion bombardment which are accelerated into the plasma. A DC potential is used drive the ions towards the surface of one of the electrodes (named the target) causing atoms to be knocked off the target and condense on the substrate surface [139]. A strong magnetic field is applied to contain the plasma near the surface of the target to increase the deposition rate [138]. Rf sputtering is ideal for the production of high quality films without heating the substrate due to the additional energy delivered from the plasma to the growing film [4].

3.2.2. Channel Layer Deposition (RF Magnetron Sputtering Specifics)

GSZO for both film characterization and TFT production were deposited by rf magnetron sputter deposition. The deposition process was performed in the Edwards ESM 100 sputtering tool [140, 141], using the sputter up configuration. Prior to film deposition, pre-sputtering was performed at a RF power of 60 W for 10 minutes to remove oxide build-up from the target's surface. A GSZO layer approximately 30 nm thick was then deposited using a 4" diameter single target located approximately 90 mm

from the substrate. The target was composed of 88 wt. % ZnO, 7 wt. % SnO_2, and 5 wt. % Ga_2O_3. The target's elemental atomic concentration was calculated to be 51.5 , 44.4 , 2.2, 1.9 % O, Zn, Ga, and Sn, respectively. Depositions were carried out using a rf powers of 120 W and 45 W, and processing pressure ($Ar + O_2$) of 5 mTorr. Depositions performed utilized various O_2 flow rates ranging from 0 to 10 sccm. Deposition temperatures were room temperature (RT) and an elevated temperature (ET) of 150 ˚C. A radiant heater was used to heat the sputtering chamber for ET depositions. Films for XPS, and TFT production were deposited on thermally grown SiO_2 coated Si substrates, where films for transmission and XRD measurements were deposited on 7059 glass. SiO_2 was grown to an approximate thickness of 125 nm.

3.3 Thickness Measurements

A thickness measurement of both silicon dioxide (prior to film deposition) and GSZO was conducted using ellipsometry. This contactless optical technique measures the change in polarization state of light reflected from a surface. The polarization change is dependent upon the optical constants of the substrate, the angle of incidence of the light, the optical constants of the film, and the film thickness. If the optical constants of the substrate are known and if the film is non-absorptive at the wavelength being used, the state of polarization of the reflected beam depends only the index of refraction and the thickness of the film.

The Rudolph Research Auto EL II model ellipsometer used to conduct ellipsometry measurements is shown in Figure 3.2. A He/Ne laser operating at a

wavelength of 632.8 nm was used to penetrate the GSZO films and reflected to a sensor for analysis.

Figure 3.2. Rudolph Research Auto EL II model ellipsometer.

3.4 Post Deposition Annealing

Post deposition annealing of the sputtered channel material was performed to optimize film perform. Annealing was performed in an in-house built single zone annealing furnace (Figure 3.3), which consists of a Au coated quartz tube, sample boat (for sample loading), and k type thermocouples (for temperature monitoring). Annealing ambient, duration and temperature were varied. Ambients included rough vacuum, air, and N_2. Durations ranged from no annealing to 4 hours. Annealing temperatures consisted of 150, 250, 350, and 450˚C. The impact of these variations is illustrated in chapter 4.

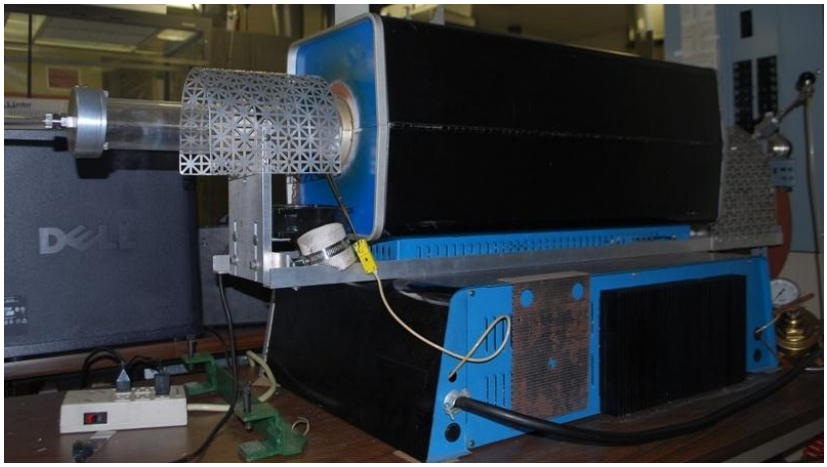

Figure 3.3. Annealing Furnace.

3.5 Transistor Production

Bottom gate TFTs with GSZO active layers were fabricated on SiO_2 coated Si substrates. The TFT fabrication process consisted of photolithography, plasma cleaning, source and drain metallization, lift-off, and gate placement.

3.5.1. Photolithography

The photolithography step was initially a one mask process that utilized a blanket layer of GSZO, this later matured to a two mask process that isolated the GSZO channel layer for TFT optimization. The one mask process consisted of defining the source and drain regions of the TFT. Mask 1 is pictured in Figure 3.4. After the deposition of the GSZO film the patterning process for the source and drain is performed. This is done by spin coating hexamethyldisilazane (HMDS) to promote adhesion of the photoresist (PR). The sample is then hard baked on a hot plate for 1 minute at 90 ˚C. After baking negative photoresist, NFR-016D2, is spin coated on top of the HMDS, and the sample is hard baked again for 1 minute at 90 ˚C. The sample is then placed in the mask aligner to be

masked and exposed to ultra violet (UV) light to apply the pattern for the channel material. The use of negative PR allows the unmasked areas of PR become more robust, where the unmasked areas are dissolvable in the PR developer. Following exposure the sample is placed on the hot plate for a 90 second post-exposure baking (PEB) to set the pattern. After which the sample is placed in the PR developer where the pattern is developed meaning the PR on the masked region is removed. An example of the pattern development differences between negative and positive resist is shown Figure 3.5.

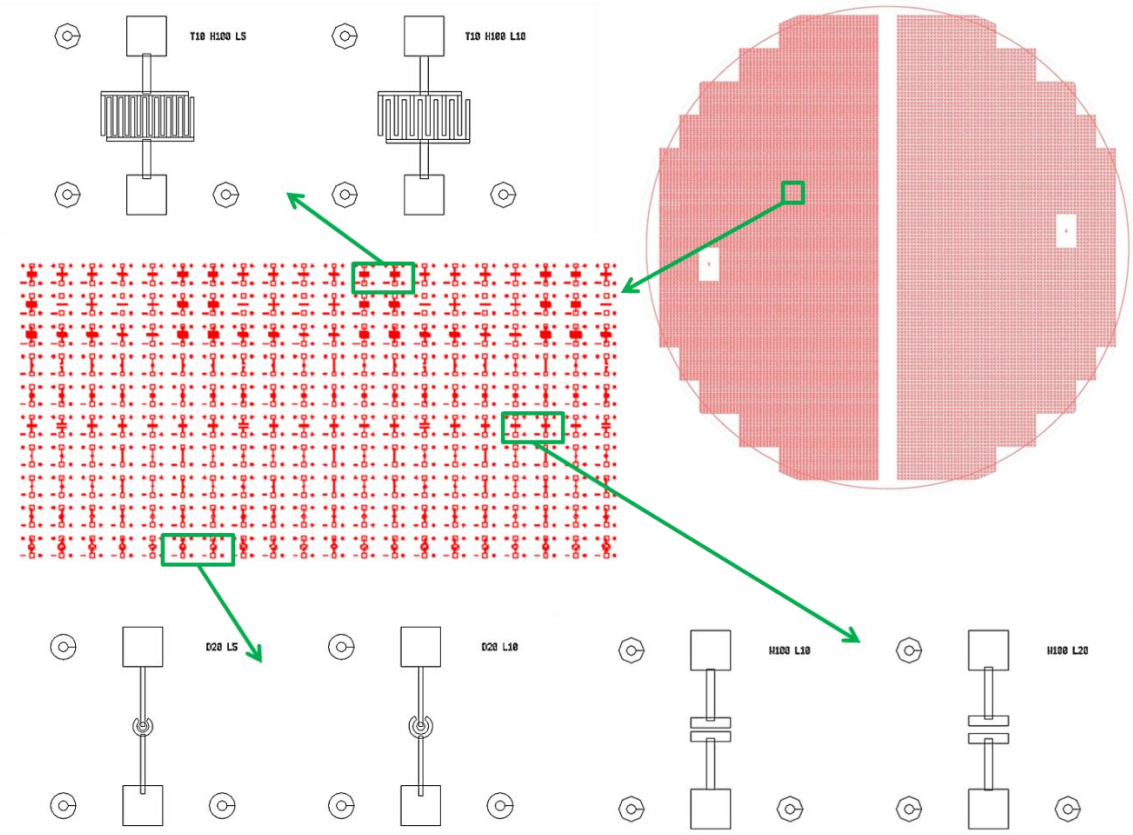

Figure 3.4. Mask 1 Design Layout.

The two mask photolithography process utilizes mask 2. The processing steps include channel layer patterning and etching steps that precede the source and drain

procedures of the one mask process. First, the channel material must be isolated for the individual devices. HMDS is spin coated onto the sample for PR adhesion promotion. The sample is then hard baked on a hot plate for 1 minute at 90 ˚C. After baking positive

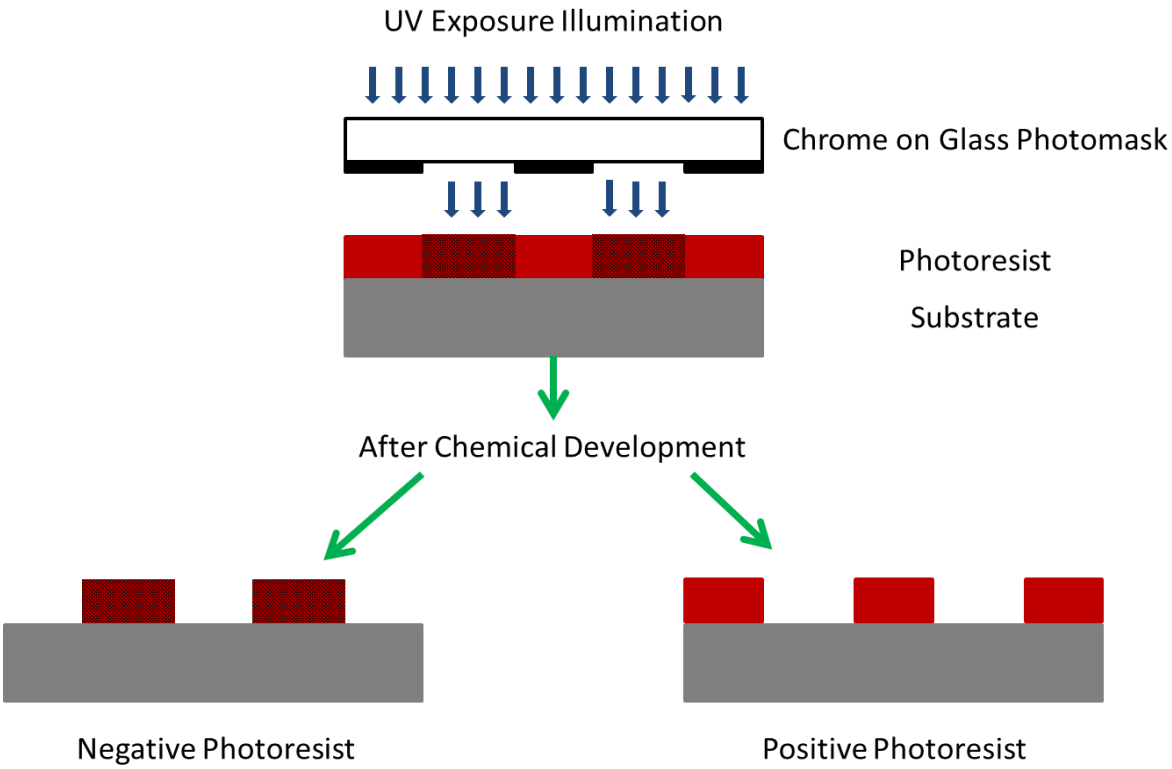

Figure 3.5 Schematic of PR development.

photoresist, Microposit s1818, is spin coated on top of the HMDS, and the sample is hard baked again for 1 minute. The sample is then placed in the mask aligner and exposed to UV light to pattern the channel material. The masked areas of PR become more robust, where the unmasked areas are soluble in the PR developer, therefore when the pattern is developed the photoresist on the unmasked region is removed. At this point the unwanted regions of GSZO are unshielded by PR. The sample is placed in a 0.1:1 solution of

hydrochloric acid and deionized (DI) water, respectively for 1 minute. This removes the unwanted GSZO and creates isolated regions of GSZO on the substrate. The PR remaining is then removed by placing the sample successively in acetone and propanol for 1 minute each. Once removed from propanol the sample is rinsed in DI water, blown dry using nitrogen gas and dehydration baked for 30 seconds. The source and drain patterning process flow is similar to the process mentioned above for the one mask. They differ only in the mask aligner step where here the source and drain pattern must be aligned to ensure placement atop the channel material, in that the PR used, NFR-016D2, is negative, the exposure is followed by a PEB prior to developing, and timing of certain steps. The differing/ new timings are as follows, 2 min for the hard baking performed after the application of the negative, 90 sec for PEB, and 30 sec for developing.

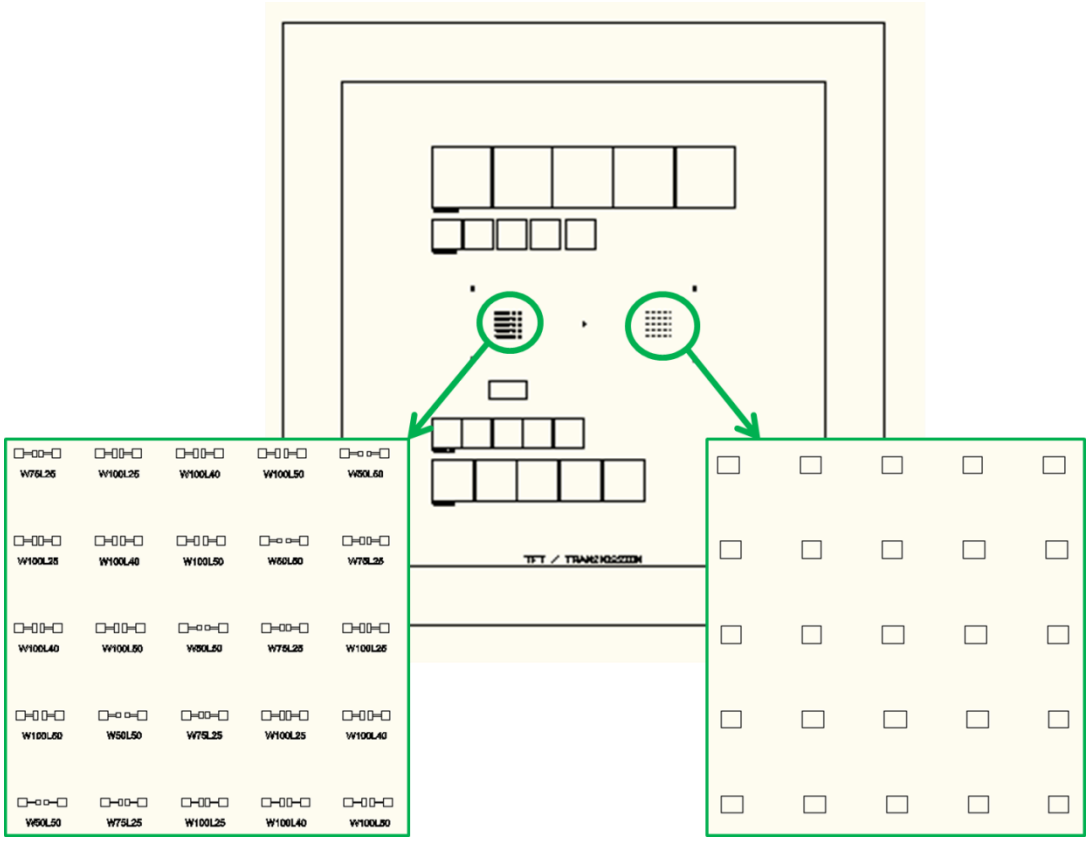

Figure 3.6 Mask 2 layout.

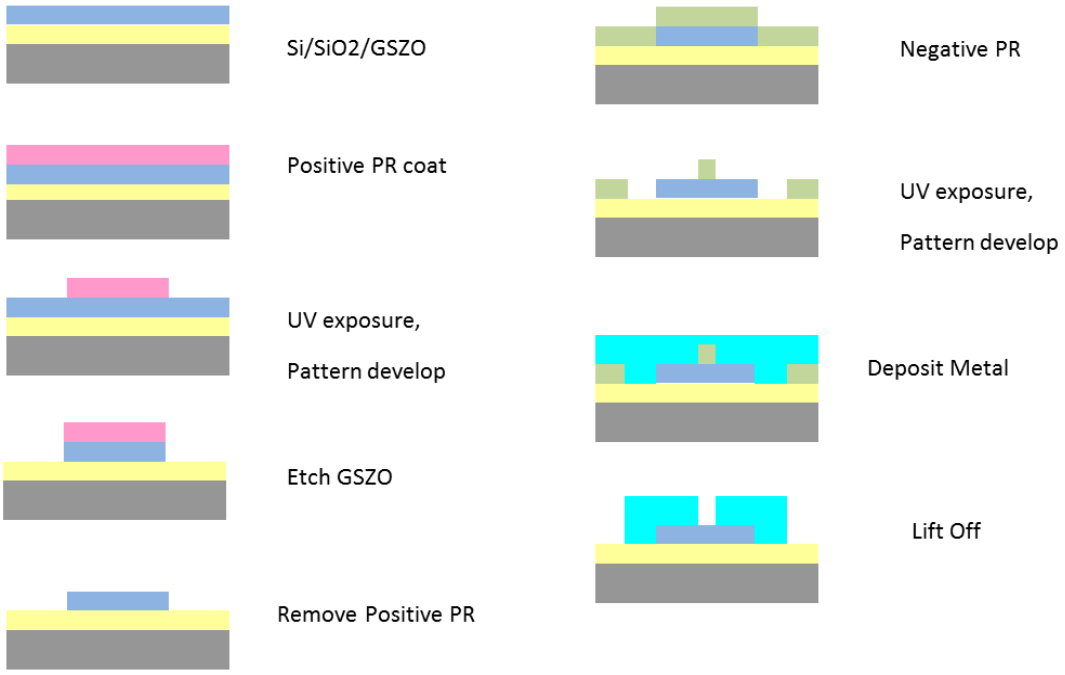

Figure 3.7. Schematic of TFT processing steps.

3.5.2. Plasma Cleaning

Plasma cleaning is conducted after photolithography to remove remaining organics and solvents left in the regions defined for source and drain metal deposition. Cleaning is performed using the South Bay Technology PE-150 plasma etcher. The sample undergoes O_2 plasma etching for 5 min. Etching was performed using a working pressure of 5 mTorr and a RF power of 149 W.

3.5.3. Metalization and Lift-off

An Airco Temescal e-beam evaporator was used to deposit Ti/Au source and drain contact metals. The Ti/Au was deposited to thicknesses of 20 and 100 nm respectively. Following deposition, the source and drain contacts and thereby the channel were patterned by lift-off. TFT produced had various W/L ratios.

3.5.4. Gate Placement

The Si substrate was used as a common gate with a silver paint contact pad. The gate contact was formed by scribing down through the SiO_2 dielectric layer to reach the Si. Once the Si was visible a small dab of silver paint was applied to that area and allowed to air dry.

3.6 Film Characterization

Various measurement techniques were employed to determine the properties of the channel materials. The Varian Cary UV-VIS-NIR 6000i spectrophotometer was used to conduct transmission measurements. Transmission data relayed the transparency of the films, and the data extracted from the measurements gives information on the optical band gap material.

3.6.1. XRD

XRD measurements were performed using the Bruker D8 Discover XRD System, to verify the amorphous nature of the film. XRD is a non-destructive technique for determining a film's structural information. X-rays are incident on the sample at XRD an angle α. The primary beam is absorbed by or transmitted through the sample; only the diffracted beam is recorded on the film. The diffracted beam emerges at twice the Bragg angle θ (Equation 3-2)

$$\boldsymbol{\theta = \arcsin\left(\frac{\lambda}{2d}\right),} \qquad \textbf{3-2}$$

which relates the wavelength of electromagnetic radiation to the diffraction angle and lattice spacing. These diffracted X-rays are then detected and processed where it is then

converted into a count rate which relays the intensity of the diffracted beam which is more intense for dislocations.

3.6.2. XPS

Electrons occupy discrete energy levels or states in an atom and can be excited to higher energy states through collisions with energetic particles or interaction with electromagnetic radiation [142], and upon suitable excitation, produces unique spectral radiation. The identification of this emitted spectral radiation can be used to determine the presence and concentration of elements in a sample. A technique that exploits this phenomenon to determine elemental composition is x-ray photoelectron spectroscopy (XPS). XPS, a high energy version of the photoelectric effect is primarily used for identifying chemical species at the sample surface [143], where incident x-rays interact with core level electrons, causing electron ejection from any orbital with photoemission occurring for x-ray energies that exceed the binding energy. XPS measurements were carried out by Evans Analytical Group, using the Phi 5701 LSci with a 1486.6 eV x-ray Al-Kα source. Samples were not sputtered in an effort to preserve the atomic composition of the GSZO surface. As a result a surface oxide was measured along with film characteristics. A sample area of 2.0 mm x 0.8 mm was analyzed, and the resulted data was charge corrected based on C1s at 284.8 eV.

3.6.3. Transmission

Transmission measurements were conducted using a Varian Cary 5000 spectrophotometer. Films used for transmission measurements were deposited on 7059

glass substrates. Measurements were conducted in the visible range (200 nm – 800 nm). A bare glass substrate was used as a reference.

3.7 Transistor Characterization

Electrical characteristics of the TFT were analyzed with respect to V_T, $I_{on/off}$, I_D, SS, and in some instances I_{off} using a Keithley 4200-Semiconductor Characterization System and SemiProbe LA-150 probe station. V_T was determined from the extrapolation of the $\sqrt{I_D}$ vs. V_{GS} data through the V_{GS}-axis at I_D= 0 A. SS was determined from the linear portion of the transfer graph by calculating the change in gate voltage per decade of drain current. Output and transfer characteristics were measured in air and in the dark, except for photoexcitation tests which were illuminated by a laser light.

3.7.1. Gate Stressed Stability Tests

Device stability under electrical stress was investigated by applying a voltage to the gate of the TFT for a pre-determined amount of time of up to 10^6 sec, and then measuring the transfer characteristics at the end of each stress period. TFTs were stressed to produce both low and high electric fields that correspond to applied gate voltages of 1.2 and 12 V, respectively. Transfer characteristics measured during stress tests had a drain voltage (V_D) of 0.1 V.

3.7.2. Photoexcitation

To determine the change in trap density and the trapping mechanisms within the films of different deposition processes, photoelectron spectroscopy was performed. The effects were observed through transfer characteristics of photoexcited TFTs. A laser of energy 1.94 eV (639 nm) or 2.33 eV (532 nm) was focused on the transparent channel of

the TFT to excite trapped carriers. Transfer measurements were taken while the TFT was in the dark and re-measured under photoexcitation. To ensure the effects of photoexcitation were observed, V_D was maintained at a low voltage of 1 V.

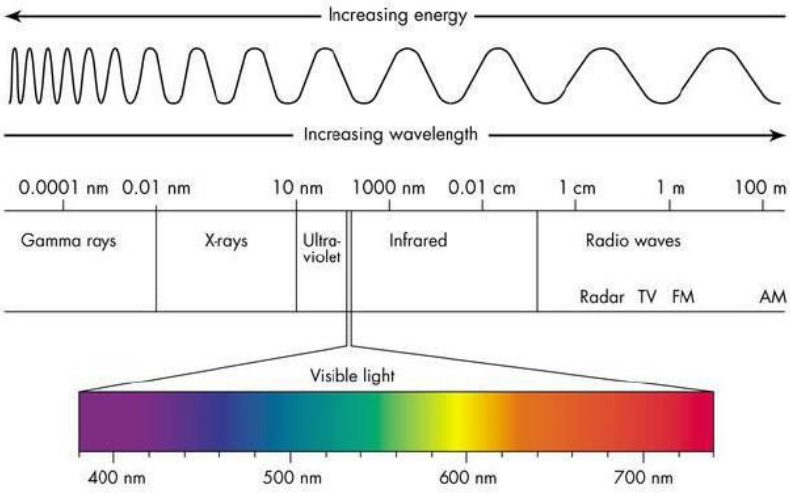

Figure 3.8. The electromagnetic spectrum [144].

CHAPTER 4

RESULTS

4.1 Film Characterization Results

4.1.1. XRD Results

XRD measurements were performed on samples of various deposition and annealing temperatures. An amorphous like behavior is illustrated for all samples despite ET deposition and increased annealing temperatures as shown in the diffractograms of Figure 4.1. The diffraction peak shown at 33° is attributed toSi (200).

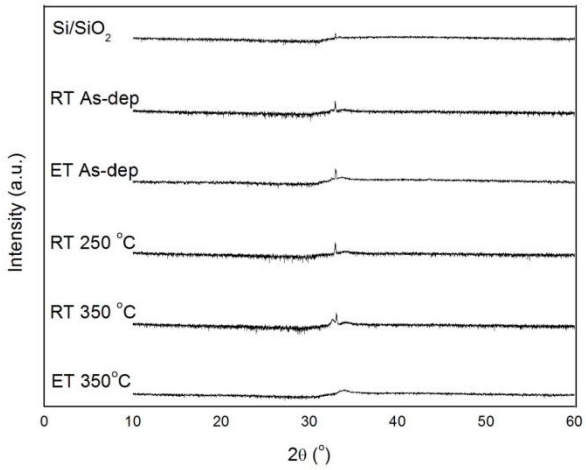

Figure 4.1. XRD diffractograms of GSZO films with various deposition and annealing temperatures.

4.1.2. XPS Results

XPS analysis was employed to observe the effects of deposition conditions on the surface composition. Chemical state assignments for a given element were made based on reference data from the literature. The species identified were of various concentrations, and consisted of Zn^{2+}, Sn^{4+}/Sn^{2+}, Ga^{3+}, Cl^{-}, hydrocarbons, C-O and O-C=O. The close proximity of the binding energies of Sn^{4+} and Sn^{2+} (486.5 and 486.25 eV

respectively) does not allow the unequivocal determination of oxidation state. However, Sn is most likely in the state of oxidation Sn^{4+}, as Sn^{2+} is not commonly observed in the system. Finally, the levels of organics observed were deemed typical of air-exposed inorganic materials. The lack of Sn, Ga, and Zn on the surface indicates an oxide layer of at least 3-5 nm for each sample. The atomic concentration data shown in Table 4.1 was normalized after removing the C contributions. Sample names are designated to easily identify samples in reference to their deposition condition, and are formatted as follows (deposition temperature - oxygen flow - annealing temperature). Table 4.2 summarizes the Zn charge corrected peak positions and widths, and Table 4.3 that of both Sn and Ga . Included in the table is the position of the main Zn Auger line, which was used to aid in assigning the oxidation state of zinc. Zn Auger parameter is a measure of the kinetic energy from the Auger peak plus the binding energy of the photoelectron. This is constant throughout all the samples which indicates that the shift in surface charge is minimal. Further, the full width at half maximum (FWHM) of the samples show no significant variation, suggesting the local atomic arrangement remains the same. The general peak shape of the metals identified are shown in Figure 4.2. The shape of the metal element peaks did not change with processing.

Table 4.1. Normalized elemental at. % concentration on the surface

Sample	O at. %	Cl at. %	Zn at. %	Ga at. %	Sn at. %
RT-2-0	54.3	0.6	41.2	1.6	2.2
RT-2-150	55.0	1.3	39.9	1.4	2.4
RT-2-250	53.3	0.9	41.7	1.5	2.5
RT-2-350	56.9	1.2	37.1	2.0	2.9
ET-2-0	50.7	0.6	44.5	1.8	2.4
ET-2-150	53.7	0.8	41.8	1.5	2.3
ET-2-250	52.3	0.9	42.7	2.0	2.3
ET-2-350	52.6	1.1	41.4	2.2	2.7
RT-0-250	53.4	1.2	40.8	1.9	2.8
RT-10-250	51.9	1.4	42.7	1.7	2.3

Table 4.2. Zn peak positions and full-width-at-half-maximum (FWHM)

	Zn $2p_{3/2}$		Zn LMM	Zn Auger Parameter (eV)
Sample	BE (eV)	FWHM (eV)	BE (eV)	
RT-2-0	1021.8	1.9	498.6	2009.9
RT-2-150	1021.7	1.9	498.4	2010.0
RT-2-250	1021.8	1.9	498.4	2010.1
RT-2-350	1021.8	2.0	498.4	2010.0
ET-2-0	1021.8	1.9	498.5	2010.0
ET-2-150	1021.8	1.9	498.5	2010.1
ET-2-250	1021.8	1.9	498.4	2010.1
ET-2-350	1021.8	2.0	498.4	2010.2
RT-0-250	1021.8	1.9	498.3	2010.2
RT-10-250	1021.8	2.0	498.4	2010.2
Avg.	*1021.8*	*2.0*	*498.4*	*2010.1*
St. Dev.	*0.04*	*0.05*	*0.08*	*0.08*

Table 4.3. Sn & Ga peak positions and full-width-at-half-maximum (FWHM)

	Sn $3d_{5/2}$		Ga $2p_{3/2}$	
Sample	**BE (eV)**	**FWHM (eV)**	**BE (eV)**	**FWHM (eV)**
RT-2-0	486.5	1.6	1117.8	1.6
RT-2-150	486.5	1.6	1117.6	1.9
RT-2-250	486.5	1.6	1118.0	1.8
RT-2-350	486.6	1.6	1117.9	1.9
ET-2-0	486.4	1.6	1117.8	1.8
ET-2-150	486.5	1.6	1118.0	1.7
ET-2-250	486.5	1.6	1118.0	1.9
ET-2-350	486.5	1.6	1118.0	1.9
RT-0-250	486.4	1.6	1117.9	1.8
RT-10-250	486.5	1.6	1117.9	1.9
Avg.	*486.5*	*1.6*	*1117.9*	*1.8*
St. Dev.	*0.04*	*0.02*	*0.11*	*0.10*

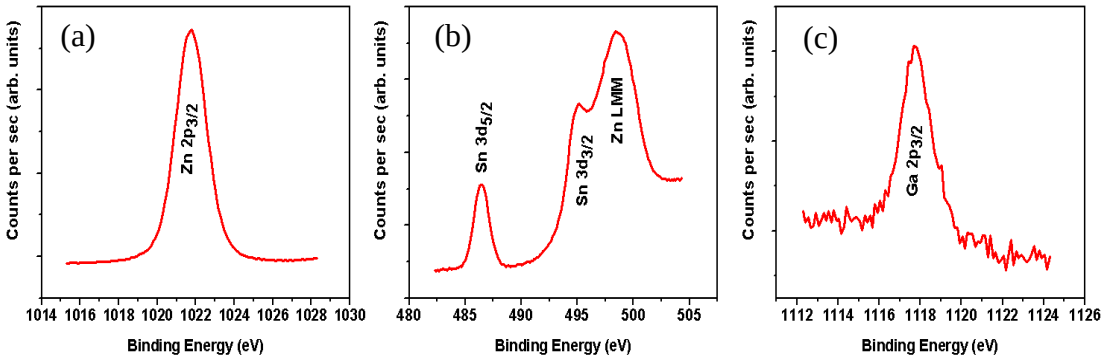

Figure 4.2. The (a) Zn $2p_{3/2}$, (b) Sn $3d_{5/2}$, Sn $3d_{3/2}$, & Zn LMM, and (c) Ga $2p_{3/2}$ typical XPS spectra of measure GSZO films.

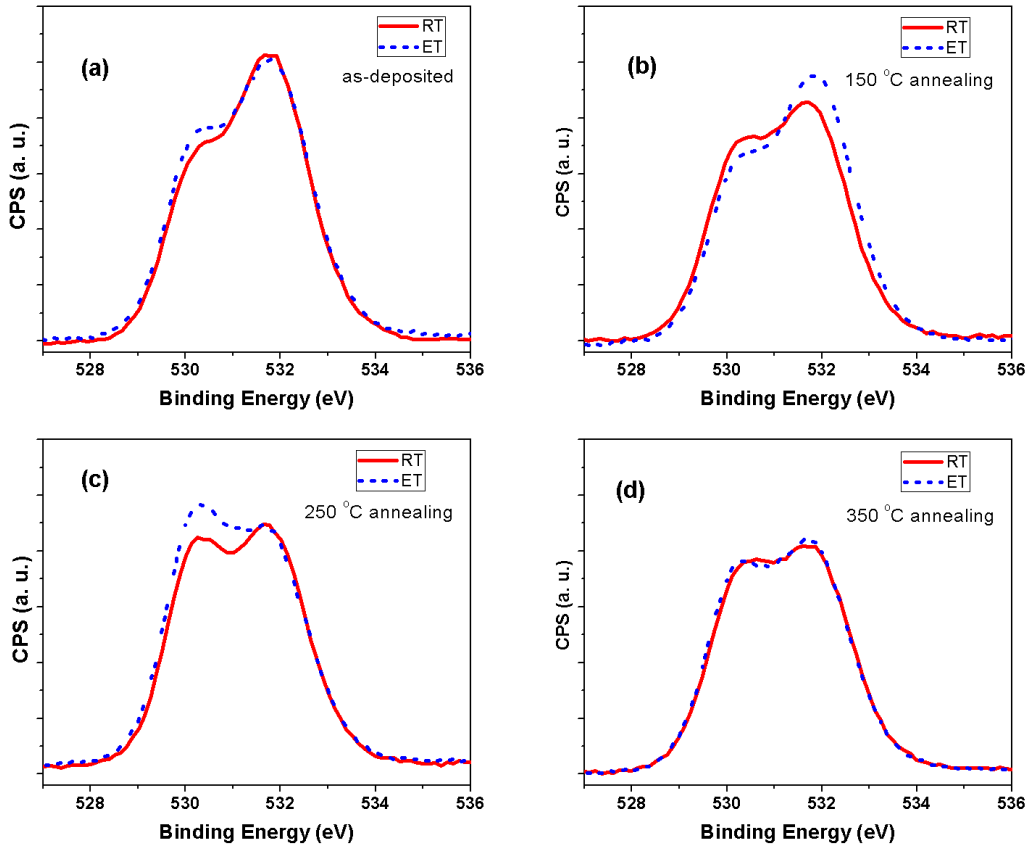

Figure 4.3. O1s peaks for RT and ET films with various annealing temperatures.

The O 1s peaks shown in Figure 4.3 demonstrate the influence of deposition temperature and post-deposition annealing, on the shape and intensity of the two contributing peaks. The peak at the lower energy will be referred to as $O_{I(x)}$, and the higher energy peak will be $O_{II(x)}$, where (x) is the deposition temperature, RT or ET. The variation in concentration of the O1s sub-peaks is quantified in Table 4.4. The O_I peak is attributed to the O^{2-} ions combined with Zn, Ga, and Sn ions and oxygen vacancies present in the GSZO system. The O_{II} peak is assigned to weakly bound oxygen species on the films surface such as M-OH, $-CO_3$, or absorbed O_2 [129],and possibly Zn vacancies.

The presence of the chemisorbed M-OH species (O_{II} contributers) on the surface suggests that metal ions are not effectively converted to metal oxides [146].

In Figure 4.3RT and ET peaks were analyzed comparatively. Figure 4.3a shows a slightly higher peak for $O_{I(ET)}$. Upon annealing at 150 °C (Figure 4.3b) $O_{I(RT)}$ and $O_{II(ET)}$ demonstrates the highest peaks. Figure 4.3c shows a higher $O_{I(ET)}$ peak than that of $O_{I(RT)}$ and similar RT & ET O_{II} peaks. Lastly, Figure 4.3d shows similar peaks for both RT and ET. The deconvoluted O 1s peaks of films with varied oxygen partial pressure are shown in Figure 4.4. Figure 4.4a shows a decrease in O_I peak height with increased oxygen partial pressure, and Figure 4.4b shows a slight increase O_{II} peak.

Table 4.4. O 1s fitted peak concentrations and binding energy

	Relative %		**Binding Energy (eV)**	
Sample	**O_I**	**O_{II}**	**O_I**	**O_{II}**
RT-2-0	26.7	73.3	530.1	531.8
RT-2-150	35.82	64.18	530.1	531.8
RT-2-250	39.28	60.72	530.1	531.8
RT-2-350	41.88	58.12	530.2	531.8
ET-2-0	30.95	69.05	530.1	531.8
ET-2-150	30.48	69.52	530.2	531.9
ET-2-250	41.86	58.14	530.1	531.7
ET-2-350	37.62	62.38	530.1	531.8
RT-0-250	42.45	57.55	530.2	531.8
RT-10-250	35.12	64.88	530.2	531.8

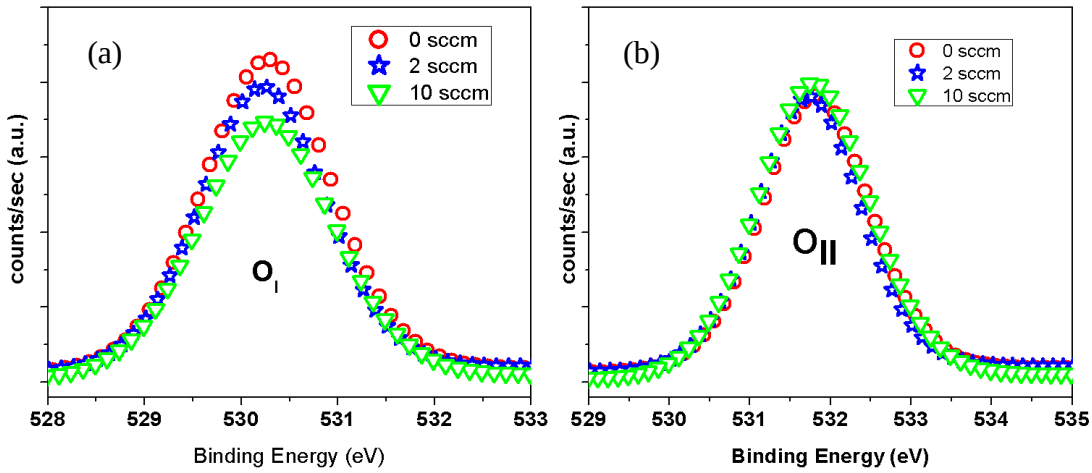

Figure 4.4. Gaussian fit of (a) O_I and (b) O_{II} contributors to the O_2 flow dependent O1s peak.

Figure 4.5 shows the influence of oxygen flow on the atomic concentration. From the figure there is a straight forward decrease in Sn and O at. %, and an increase in Zn with increased O_2 flow. Ga at % shown in Figure 4.5b demonstrates a decrease in concentration at 2 sccm followed by an increase at 10 sccm. Figure 4.6 shows the effect of annealing temperature on at. % of the elements in the film. The relationship between O at. % and annealing temperature shows no clear trend. Sn demonstrates an increase in at. % with annealing temperature. The RT and ET concentrations of Zn demonstrate similar behavior with annealing. For both RT and ET with annealing, there is an initial decrease in Ga atomic concentration followed by a steady increase.

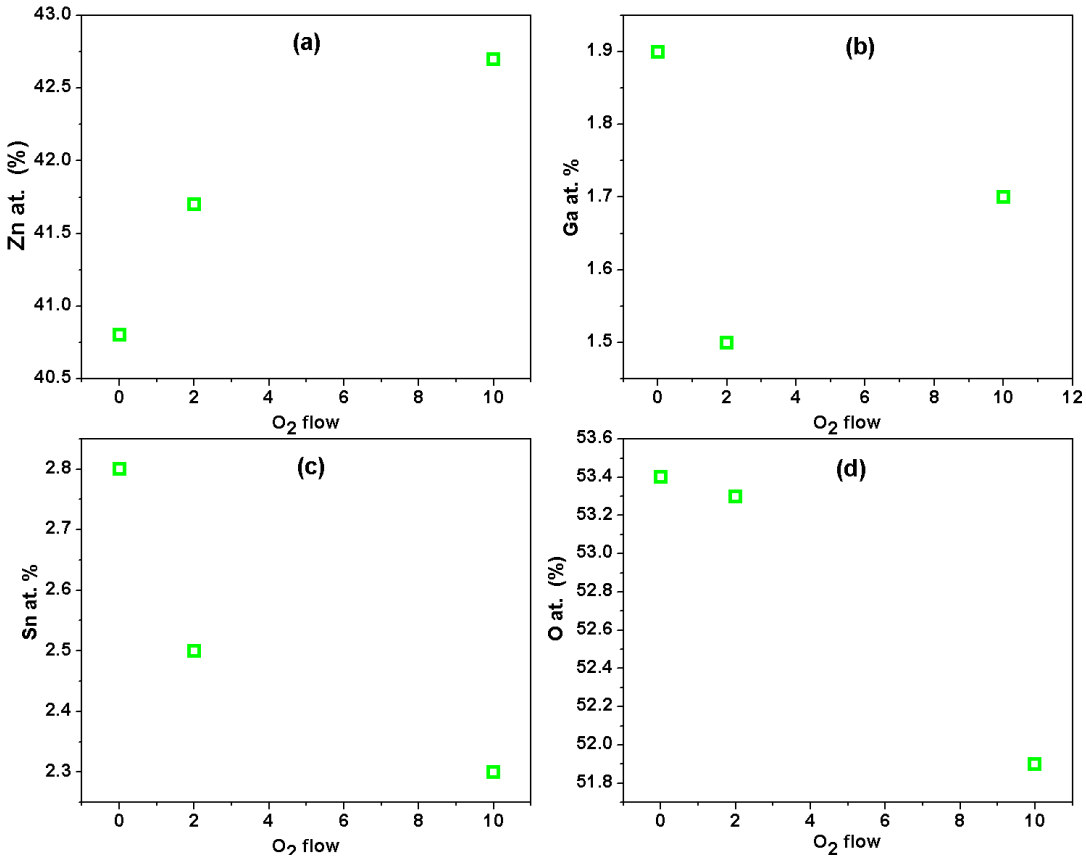

Figure 4.5. Influence of oxygen flow on the atomic concentration.

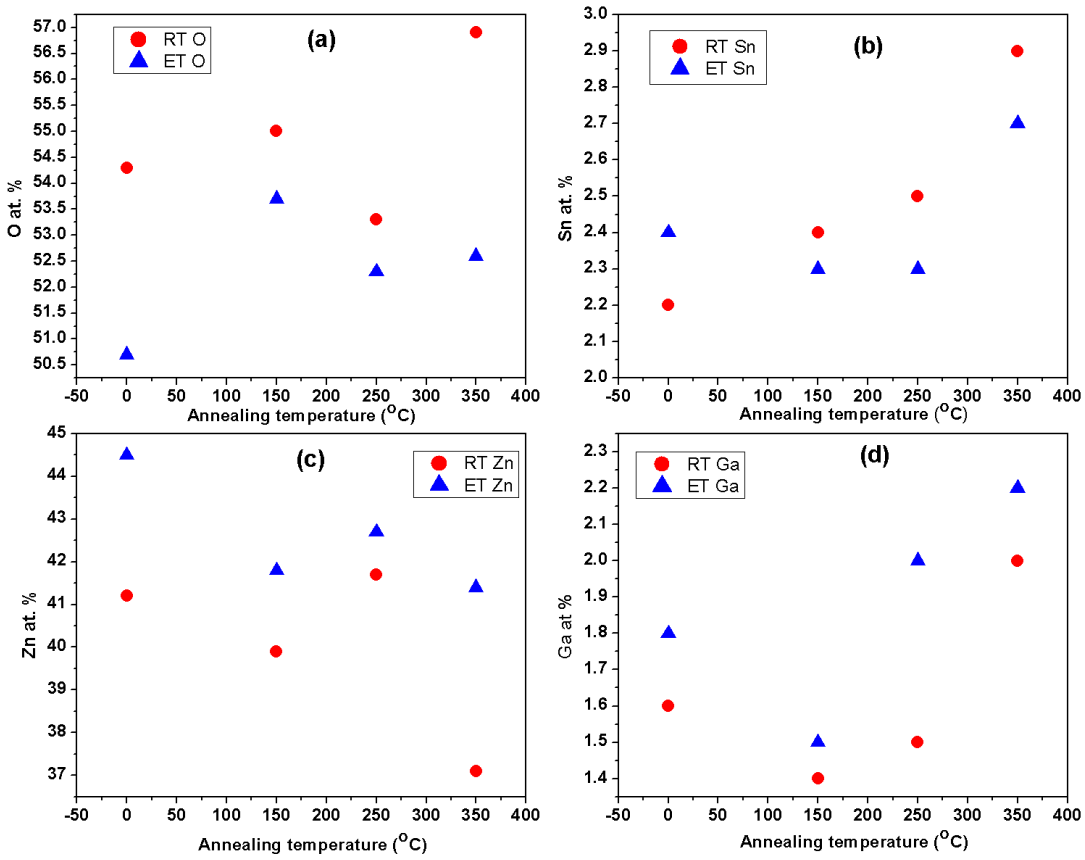

Figure 4.6. Influence of annealing temperature on the atomic concentration of RT & ET films.

The investigation into the effect of deposition temperature, oxygen flow, and annealing lead to an in-depth comparison of elemental relations. The results of these comparisons are reported below. Zn was shown (Figure 4.7) to have an inverse relationship to the concentration of oxygen. As a result, the possibility of Zn vacancies was explored by observing the dependence of the O_{II} peak on the deconvoluted carbon peaks (carbon peaks not shown). Figure 4.8 shows a proportional dependence on carbon. In addition, the Zn concentration is the highest for ET samples, followed by the O_2 flow ones and then the RT annealed samples.

The atomic concentration of both Sn and Ga with respect to Zn was shown to increase with annealing temperature for RT deposited films shown in Figure 4.9. In addition, there is a separation of the RT and ET Sn/Zn ratio, where the Ga/Zn ratio showed separation for RT and ET only for 250 °C.

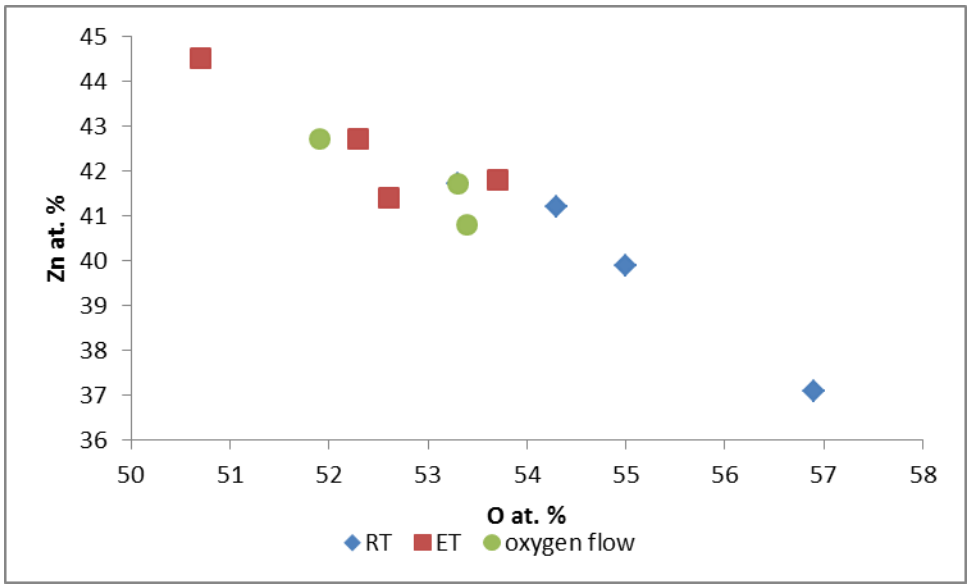

Figure 4.7. Influence of oxygen concentration on the atomic concentration of Zn.

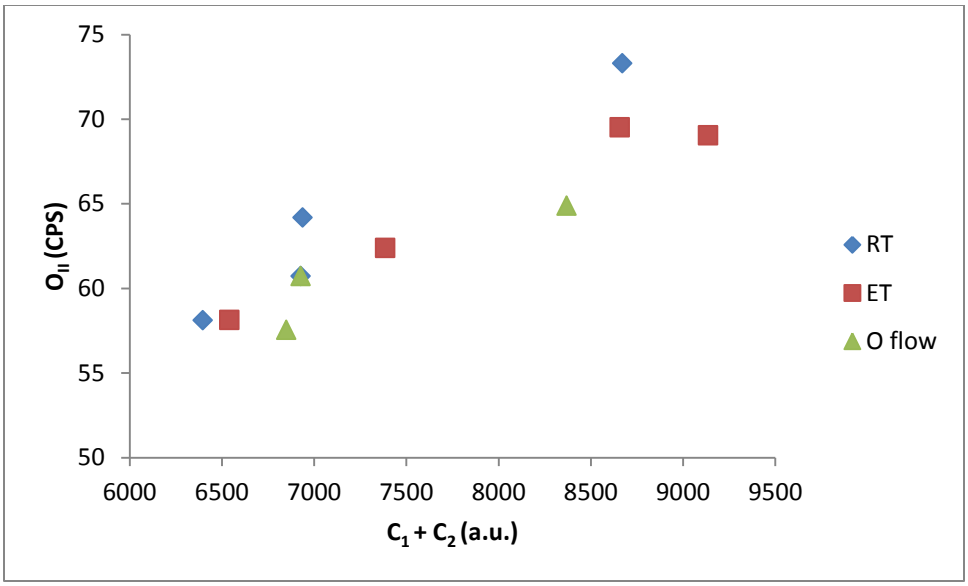

Figure 4.8. O_{II} versus C_1+C_2

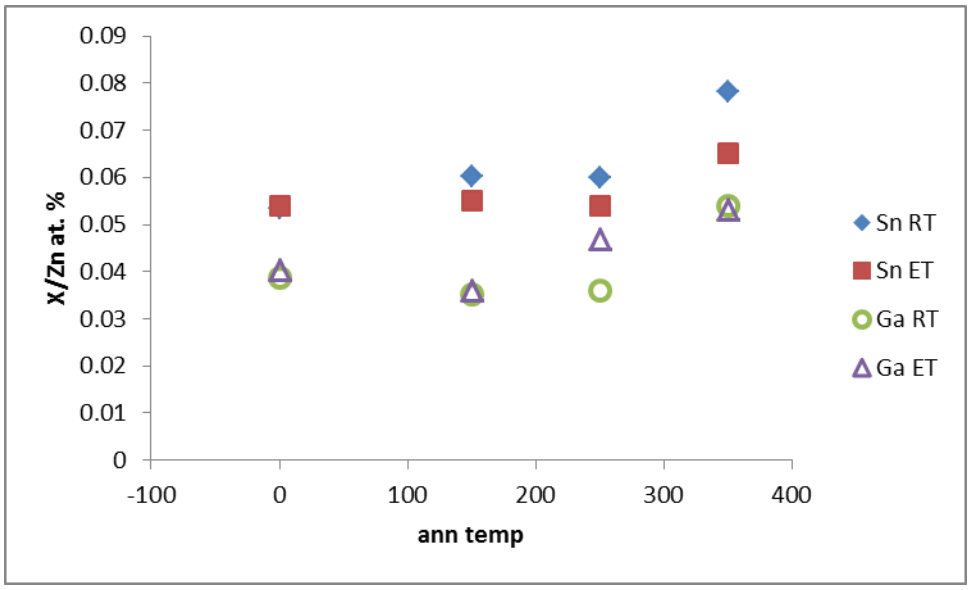

Figure 4.9. Influence of annealing temperature on the atomic concentration of Sn and Ga.

4.1.3. Transmission Results

Figure 4.10 shows the transmission spectrum of the 250 °C 1 hour annealed film. The transmittance of the film was found to improve with the oxygen flow. The Beer-

Lambert law was used to extract absorption (α) values from the transmittance data. The absorption edge was extracted from the α^2 versus photon energy plot (Figure 4.11), by extrapolating from the linear region onto the photon energy axis. The absorption edge of GSZO is observed to be approximately 3.05 eV.

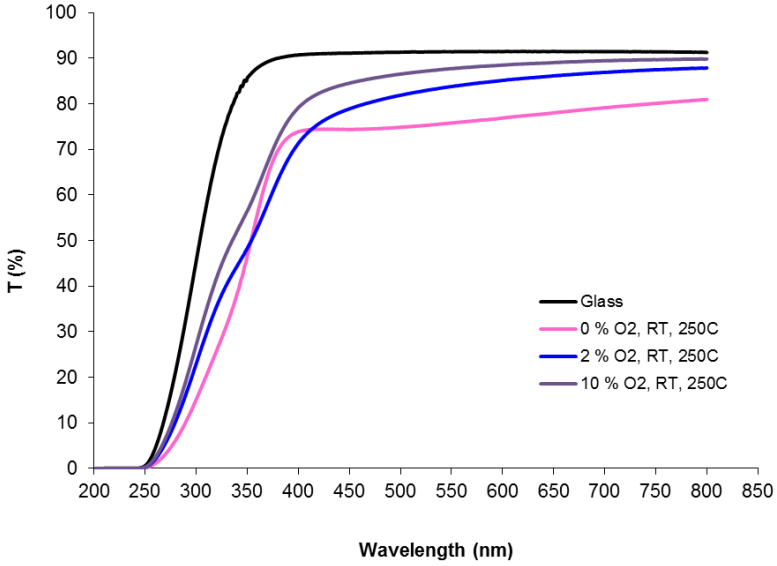

Figure 4.10. Transmission of RT 250 ˚C annealed sample.

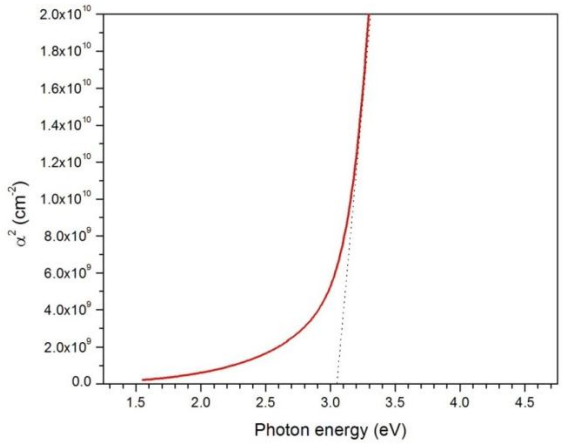

Figure 4.11. Alpha squared of RT 250 °C annealed sample.

4.2 Transistor Performance

4.2.1. Blanket GSZO

4.2.1.1. Effect of Oxygen Flow

The effect of oxygen incorporation was initially investigated on samples that utilized a blanket channel layer of GSZO. The electrical characteristics of these samples are illustrated in Figure 4.12 and Figure 4.13 for 2 sccm and 4 sccm O_2 flow respectively. Though the electrical characteristics of the 4 sccm sample are not optimal, it performs better than that of the 2 sccm by having a smaller V_T (9 V vs. 16 V), and higher $I_{on/off}$ (10^3 vs. 10^1). Both the devices possess a high I_{off} resulting in poor $I_{on/off}$. The TFTs demonstrate high SS values (> 10 V/decade) and high gate current (> $1x10^{-7}$ A).

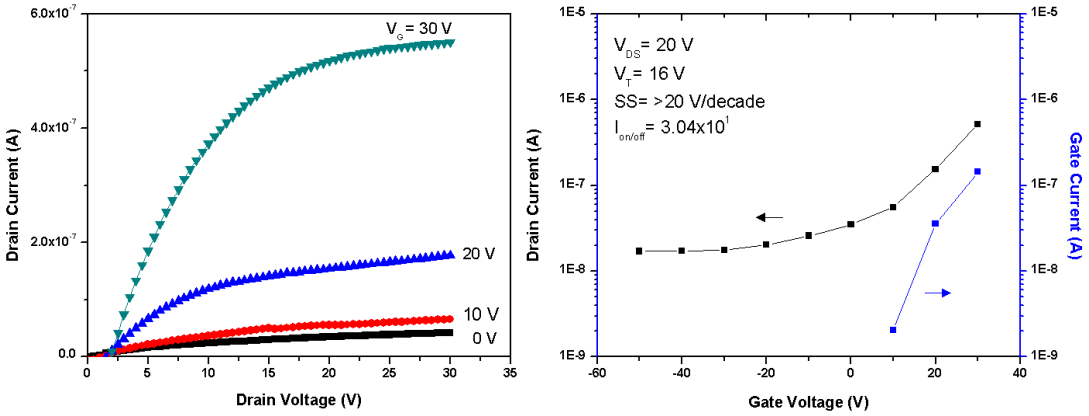

Figure 4.12. Blanket channel layer TFT electrical characteristics with 2 sccm oxygen flow.

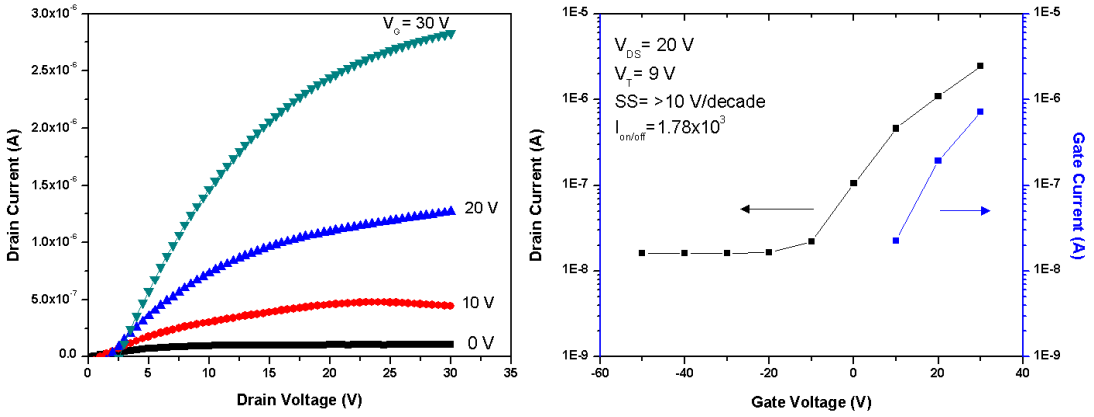

Figure 4.13. Blanket channel layer TFT electrical characteristics with 4 sccm oxygen flow.

4.2.1.2. Effect of Vacuum Annealing

The devices characterized in Figure 4.14 and Figure 4.15 have a W/L ratio of 5:1 with channel dimensions of W:100/L:20 and W:50/L:10 respectively. The sample annealed in air appears to be less conductive than that annealed in vacuum, where degree of conductivity is deduced from observing the saturation curves, calculated V_T, and achieved I_D at V_G= 30 V. The output curve of Figure 4.15a demonstrates a metallic behavior, with no sign of saturation.

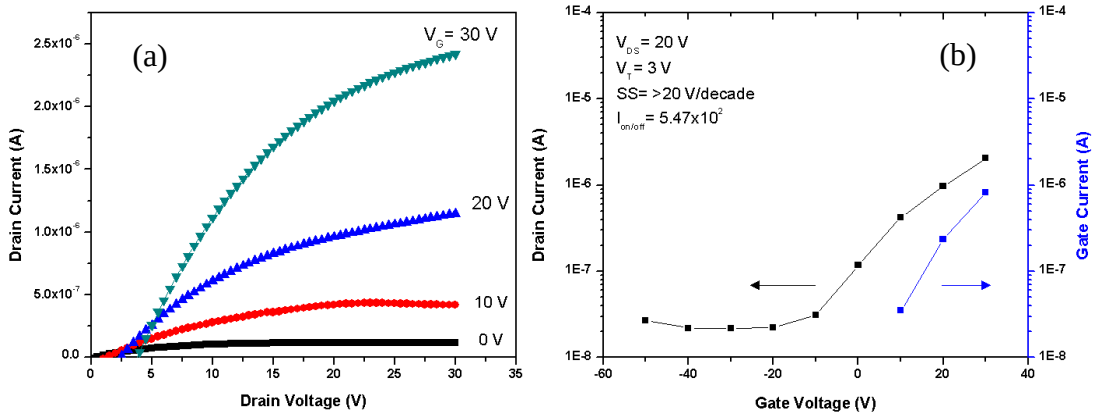

Figure 4.14. Blanket channel layer TFT electrical characteristics with film annealed 4 hours in air.

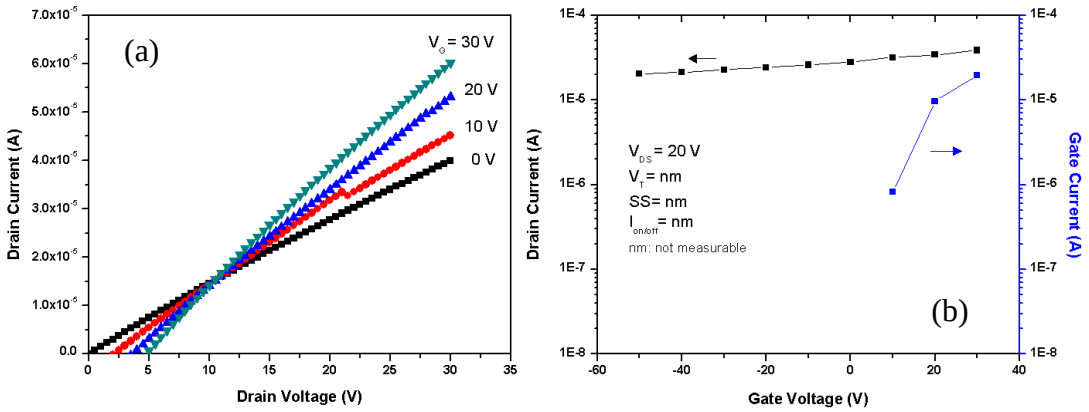

Figure 4.15. Blanket channel layer TFT electrical characteristics with film annealed 1 hour in vacuum.

4.2.1.3. Effect of annealing temperature

Devices for Figure 4.16 have channel width of 100 µm and a length of 10 µm. The channel layers for these TFTs and all the TFTs presented further were deposited with a rf power of 45 W. Transfer characteristics show increased film conductivity upon annealing at 450 °C, where the device operates in depletion mode (V_T < 0 V) and there is an increase in I_{off} greater than one order of magnitude. The specifics of the device performance are shown in Table 4.5.

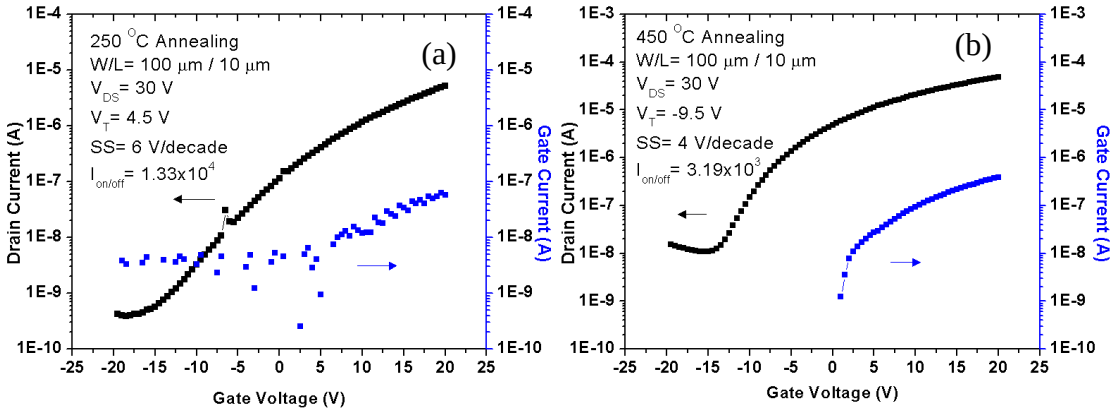

Figure 4.16. Transfer characteristic for TFTs with a) 250 °C annealing 4 hours, b) 450 °C annealing 1hour.

Table 4.5. TFT characteristics of devices annealed at 250 and 450 °C

Annealing Temperature (°C)	I_D (A)	V_T (V)	SS (V/decade)	$I_{on/off}$
250	$5.17x10^{-6}$	4.5	6	$1.33x10^{4}$
450	$4.84x10^{-5}$	-9.5	4	$3.19x10^{3}$

4.2.2. Channel layer isolation

As mentioned in the experimental section, the GSZO layer was converted from a blanket layer to insolated areas of GSZO that lie beneath the source and drain contacts. This was done to reduce the gate leakage observed when testing the blanket layer transistors. The benefits of isolated channel regions are illustrated when observing the gate leakage current of Figure 4.17 compared to that of the previous TFTs shown in Figure 4.12 through Figure 4.16. In addition, the transfer curves of the isolated devices have a reduced I_{off} value which results in an improved $I_{on/off}$. Due to these drastic improvements in device performance, all following device production procedures include channel layer isolation. Therefore, devices reported in the remainder of this work possess isolated channels unless otherwise mentioned.

4.2.2.1. Deposition temperature and annealing temperature/duration

Once the gate current was improved, the impact of deposition parameters on device performance was investigated. The influence of deposition temperature and annealing parameters were examined. The output and transfer characteristics of the devices tested during this examination are shown in Figure 4.17 - Figure 4.23. Varied deposition temperatures demonstrated a negative shift in V_T for TFTs with 250 °C

annealing, where RT devices operated in enhancement mode and ET devices in depletion mode. Conversely, the effect of deposition temperature on TFTs with 450 °C shows a positive shift in V_T, with both devices operating in depletion mode. The effect of deposition is shown comparatively in Figure 4.24. The characteristic values are shown in Table 4.6 for RT TFTs and Table 4.7 for that of ET.

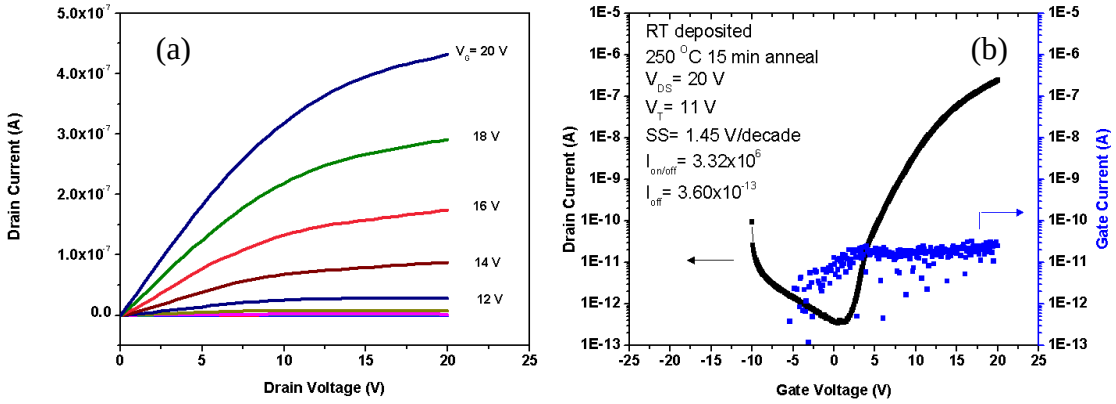

Figure 4.17. RT 250 °C 15 minute isolated channel TFT a) output and b) transfer characteristics.

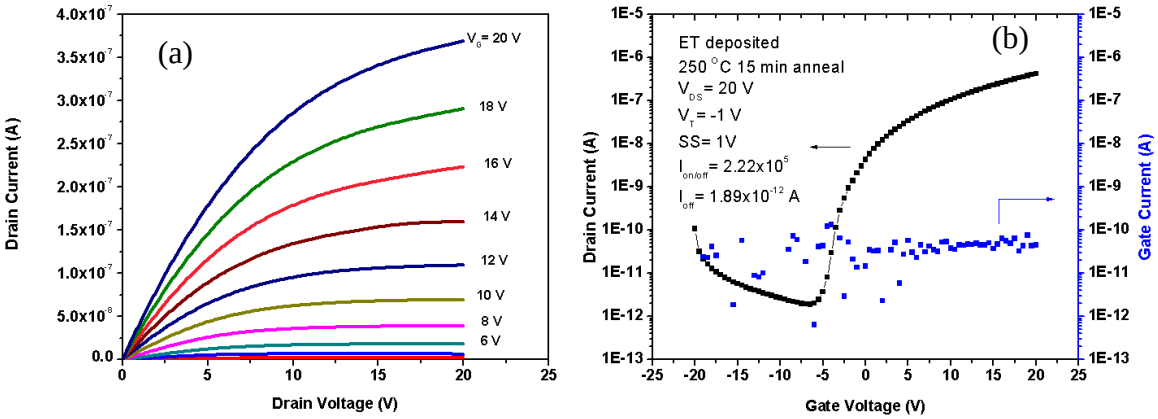

Figure 4.18. ET 250 °C 15 minute isolated channel TFT a) output and b) transfer characteristics.

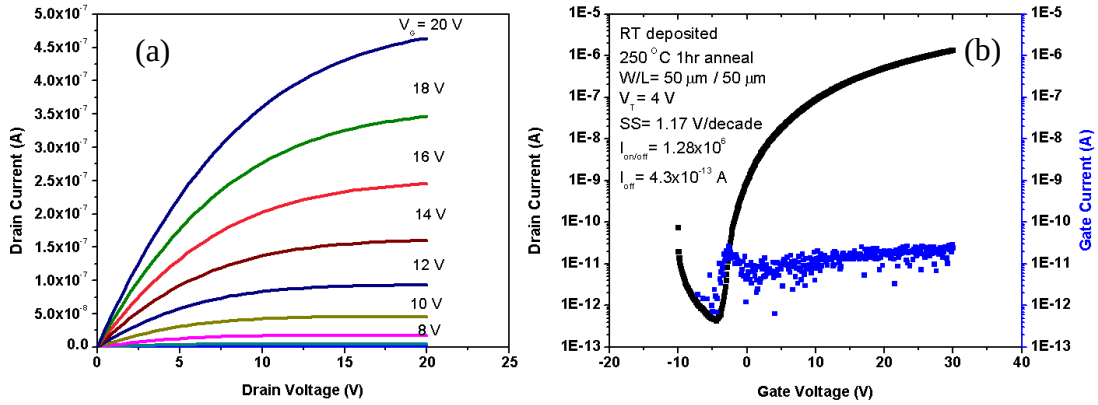

Figure 4.19. RT 250 °C 1 hour isolated channel TFT a) output and b) transfer characteristics.

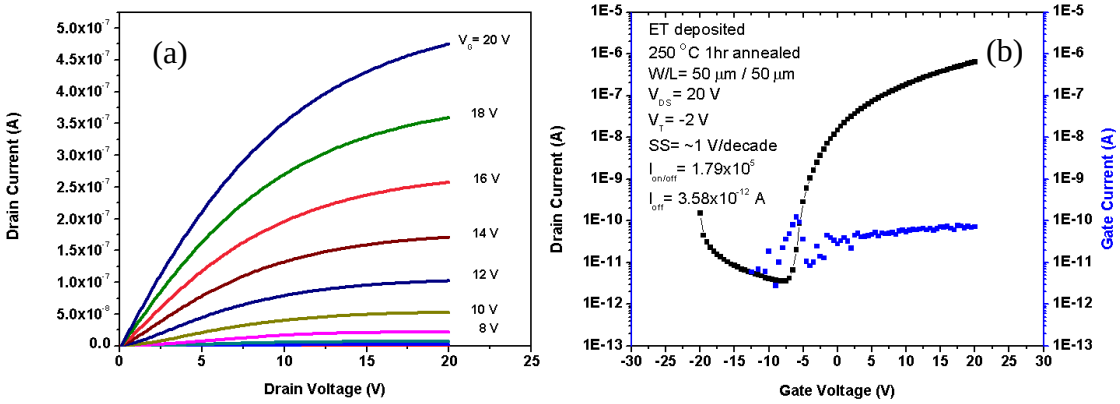

Figure 4.20. ET 250 °C 1 hour isolated channel TFT a) output and b) transfer characteristics.

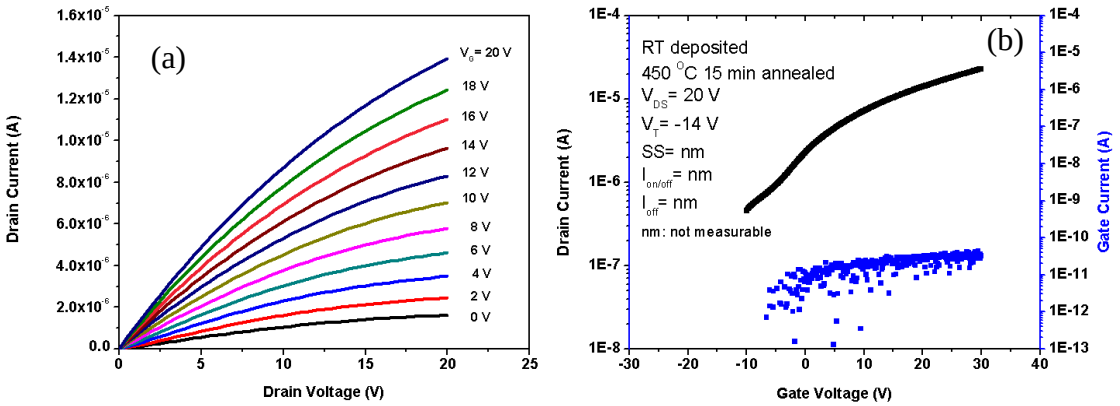

Figure 4.21. RT 450 °C 15 minute isolated channel TFT a) output and b) transfer characteristics.

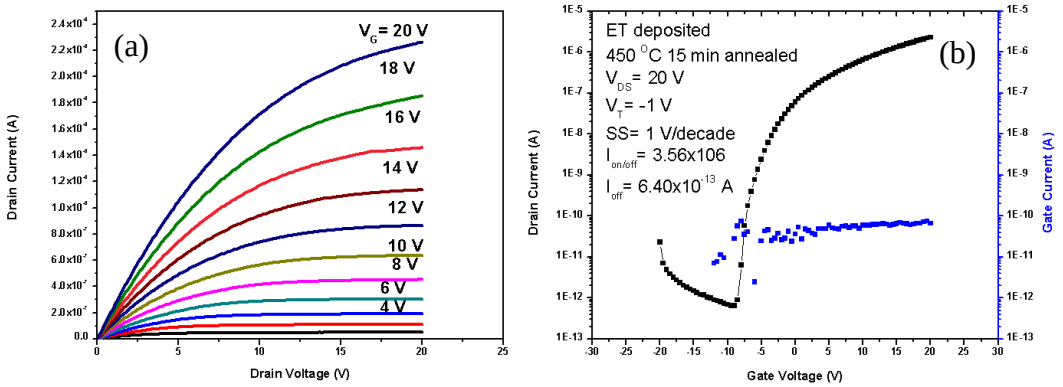

Figure 4.22. ET 450 °C 15 minute isolated channel TFT a) output and b) transfer characteristics.

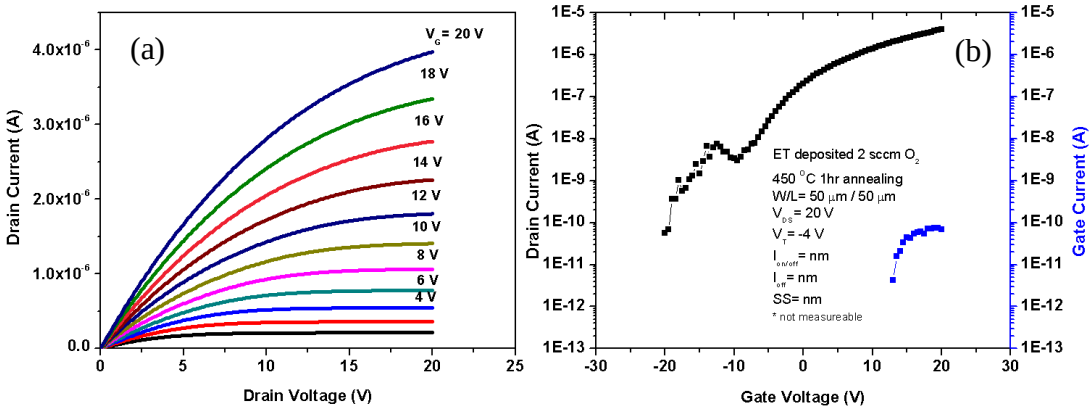

Figure 4.23. ET 450 °C 1 hour isolated channel TFT a) output and b) transfer characteristics.

Comparison of the transfer graphs shown in Figure 4.17b and Figure 4.18b to Figure 4.21b and Figure 4.22b respectively, highlights that deposition temperature is efficient in dampening the effect of higher annealing temperatures. This is clearly illustrated when observing the transfer curves of the devices with the same annealing conditions and differing deposition temperatures. The off region of all devices involved in this comparison can be viewed within V_{GS} testing range except that of the RT 450 °C, showing that annealing temperature has a greater effect on RT deposited devices than that

of ET. Figure 4.25 shows that an increase in the temperature and duration of annealing both result in a negative shift of the transfer curve along the V_{GS} axis. This negative shift is observed for both RT (Figure 4.25a) and ET (Figure 4.25b) devices.

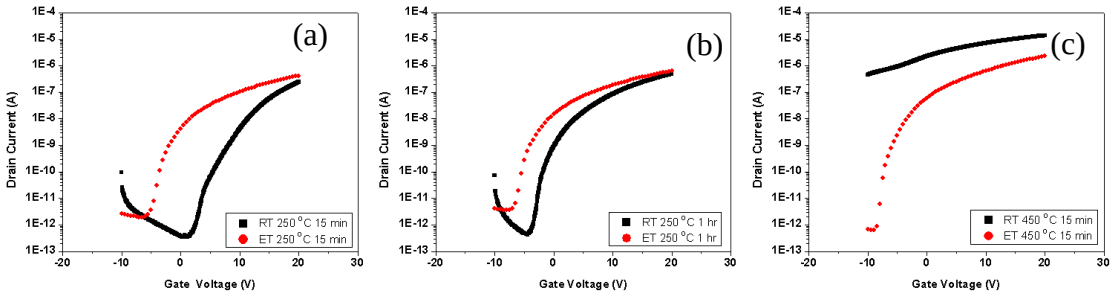

Figure 4.24. Channel deposition temperature comparison a) 250 °C 15 minute, b) 250 °C 1 hour, and c) 450 °C 15 minute.

Table 4.6. Comparison of annealing temperature effects on RT TFT performance

RT Deposited	I_D (A)	V_T (V)	SS (V/decade)	$I_{on/off}$	I_{off} (A)
250 °C 15 minute	2.42×10^{-7}	11	1.45	3.32×10^{6}	3.6×10^{-13}
250 °C 1 hour	4.94×10^{-7}	4	1.17	1.28×10^{6}	4.3×10^{-13}
450 °C 15 minute	1.39×10^{-5}	-14	Not measurable	Not measurable	Not measurable

Table 4.7. Comparison of annealing temperature effects on ET TFT performance

ET Deposited	I_D (A)	V_T (V)	SS (V/decade)	$I_{on/off}$	I_{off} (A)
250 °C 15 minute	4.19×10^{-7}	-1	1	2.22×10^{5}	1.89×10^{-12}
250 °C 1 hour	6.39×10^{-7}	-2	~1	1.79×10^{5}	3.58×10^{-12}
450 °C 15 minute	2.28×10^{-6}	-1	1	3.56×10^{6}	6.4×10^{-13}
450 °C 1 hour	3.94×10^{-6}	-4	Not measurable	Not measurable	Not measurable

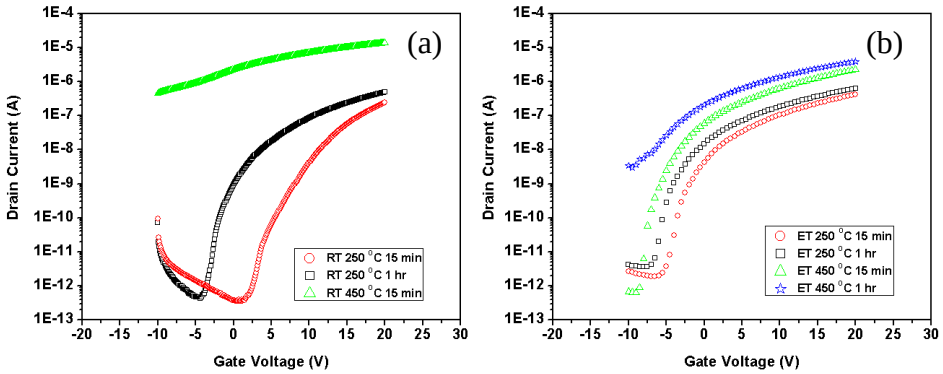

Figure 4.25. Channel annealing condition comparison a) RT and b) ET.

4.2.2.2. Annealing ambient

As a continuation of the investigation of annealing effects, annealing ambient was explored. Comparison of device performance when annealed in air (Figure 4.19) versus nitrogen (Figure 4.26) shows a lower V_T, SS, and I_{off} for the air annealed TFT. The characteristic values are shown in Table 4.8. The output characteristics of the nitrogen TFT shows stronger saturation than that of the air annealed device. The transfer curve comparison is shown in Figure 4.27.

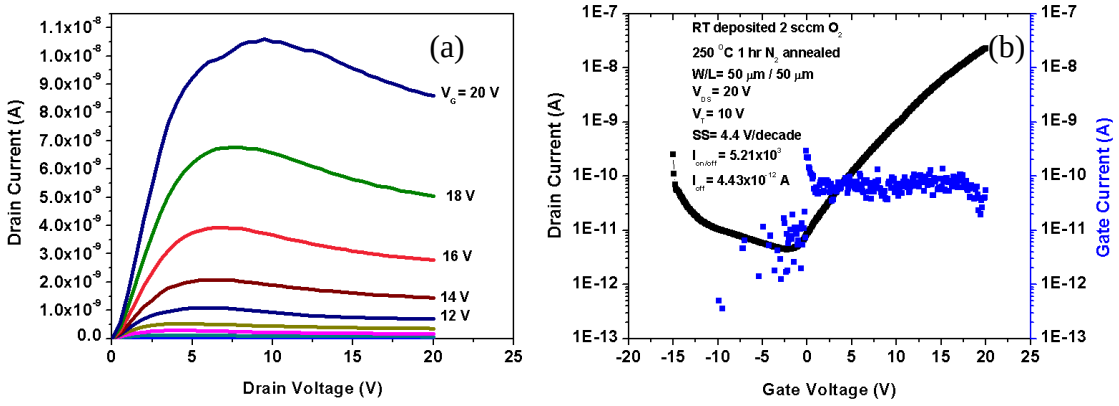

Figure 4.26. RT 250 °C 1hr N_2 2 sccm O_2 TFT a) output and b) transfer characteristics.

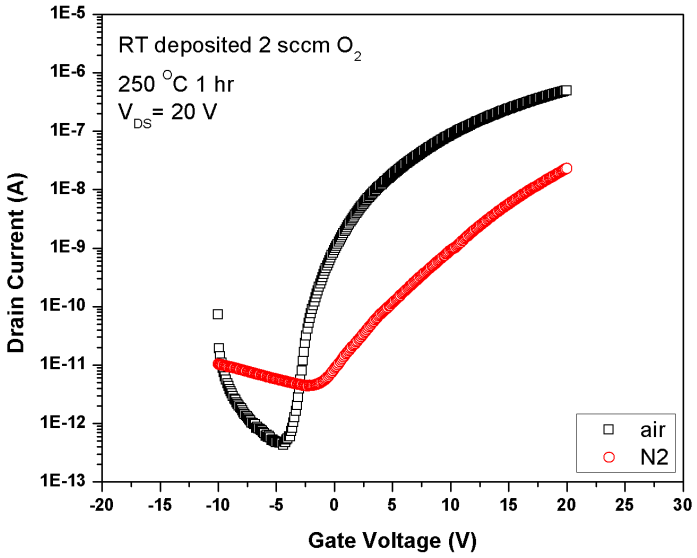

Figure 4.27. Effect of annealing ambient on TFT characteristics.

Table 4.8. Comparison of annealing ambient effects on TFT performance

Annealing Ambient	$I_{D(max)}$ (A)	V_T (V)	SS (V/decade)	$I_{on/off}$	I_{off} (A)
Air	$4.94x10^{-7}$	4	1.17	$1.28x10^{6}$	$4.3x10^{-13}$
Nitrogen	$2.31x10^{-8}$	10	4.4	$5.21x10^{3}$	$4.43x10^{-12}$

4.2.2.3. Oxygen incorporation

The effect of oxygen on TFT performance was revisited using TFTs with isolated channels layers. During this investigation TFTs were produced with 4 and 7 sccm oxygen flow. The electrical performance of these devices is shown in Figure 4.28 and Figure 4.29 respectively, shown numerically in Table 4.9. The transfer curves of the previously examined 2 sccm device and recently explored 4 sccm & 7 sccm TFTs are shown comparatively in Figure 4.30. Here it was observed that there is a negative shift in the V_{on} values of the devices with increased oxygen flow.

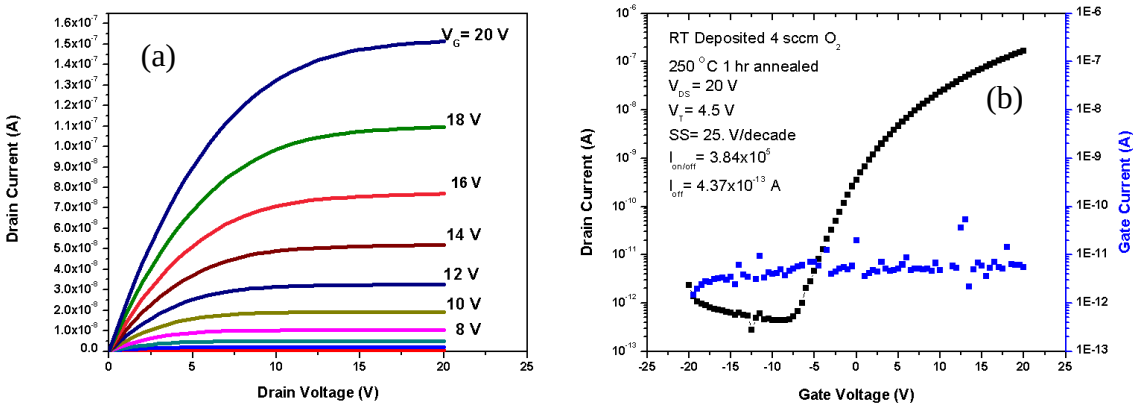

Figure 4.28. RT 250 °C 1hr 4 sccm O_2 TFT a) output and b) transfer characteristics.

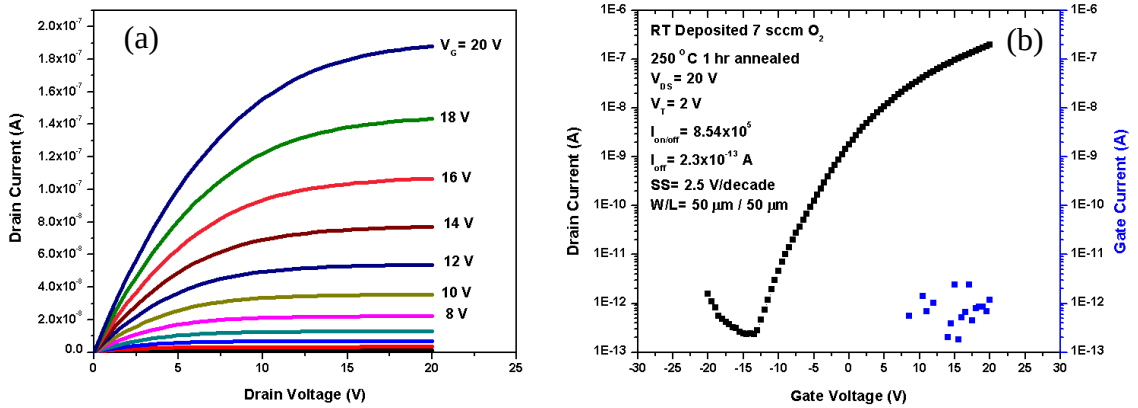

Figure 4.29. RT 250 °C 1hr 7 sccm O_2 TFT a) output and b) transfer characteristics.

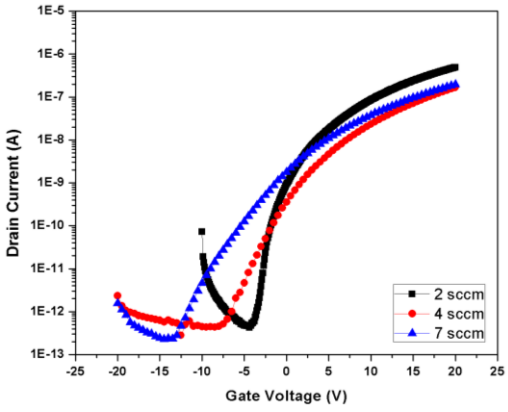

Figure 4.30. Transfer characteristics of TFTs with various oxygen flows.

Table 4.9. Comparison of the effects of oxygen flow on TFT performance

Oxygen Flow (sccm)	I_D (A)	V_T (V)	SS (V/decade)	$I_{on/off}$	I_{off} (A)
2	$4.94x10^{-7}$	4	1.17	$1.28x10^{6}$	$4.3x10^{-13}$
4	$1.67x10^{-7}$	4.5	2.5	$3.84x10^{5}$	$4.37x10^{-13}$
7	$1.96x10^{-7}$	2	2.5	$8.54x10^{5}$	$2.3x10^{-13}$

4.2.2.4. Si majority carrier type

Due to silicon being used as the TFTs' gate metal, the effect of the substrates' majority carrier type was investigated to observe the impact or lack thereof on the characteristics of the device. The output and transfer curves of these devices are shown in Figure 4.31 through Figure 4.34. The transfer curves of these TFTs are compared in Figure 4.35. V_T extracted from transfer data showed no clear trend with varied oxygen flow (Table 4.10). RT TFT transfer characteristics indicate an average V_T ranging from 0.5 – 3 V and a I_D on the order of 10^{-7} A (Table 4.10) for films deposited with various oxygen flows. The highest I_D along with the lowest SS was achieved by devices produced with a 10 sccm oxygen flow (Table 4.10). All devices observed in the oxygen incorporation studies consistently operated in enhancement mode, except those produced with 0.7 sccm oxygen flow. The 0.7 sccm group of TFTs consisted of both enhancement and depletion mode devices.

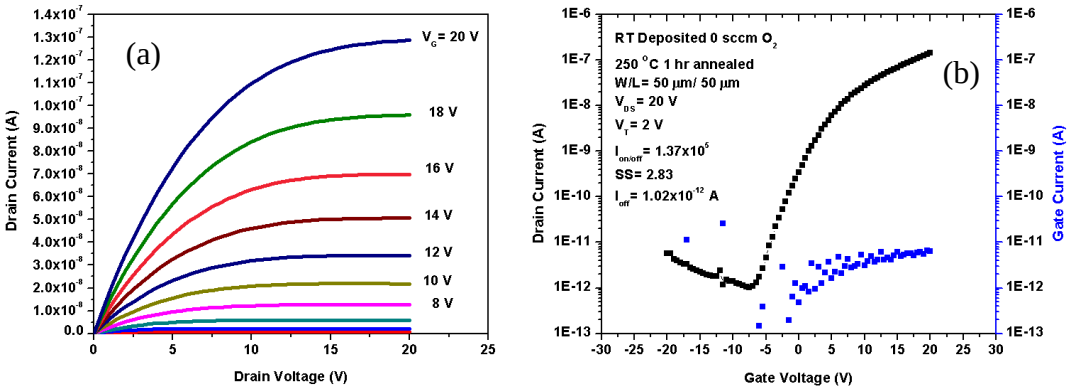

Figure 4.31. RT 250 °C 1hr 0 sccm O_2 TFT with n^+ Si substrate a) output and b) transfer characteristics.

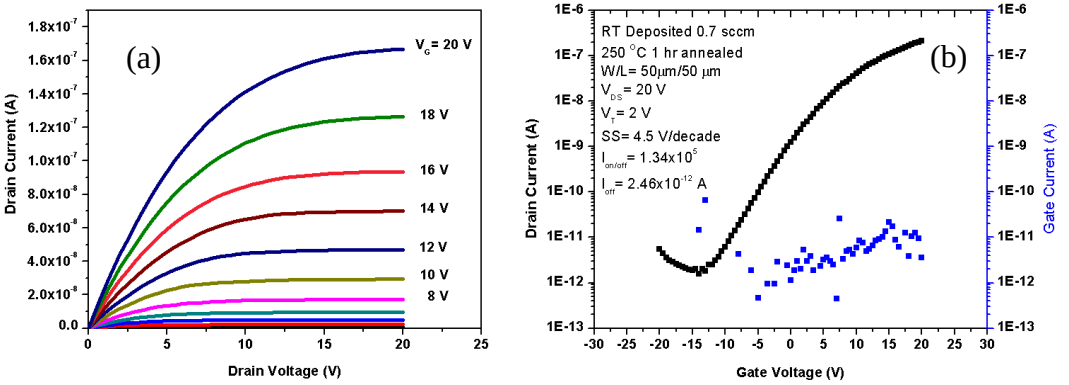

Figure 4.32. RT 250 °C 1hr 0.7 sccm O_2 TFT with n^+ Si substrate a) output and b) transfer characteristics.

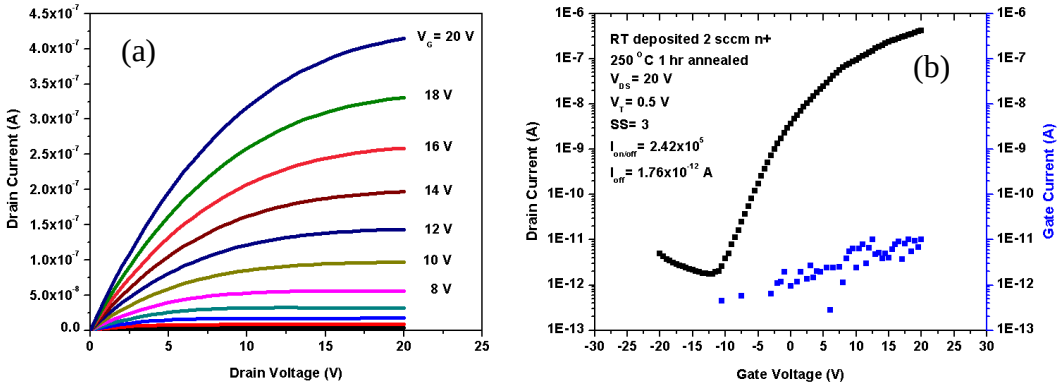

Figure 4.33. RT 250 °C 1hr 2 sccm O_2 TFT with n^+ Si substrate a) output and b) transfer characteristics.

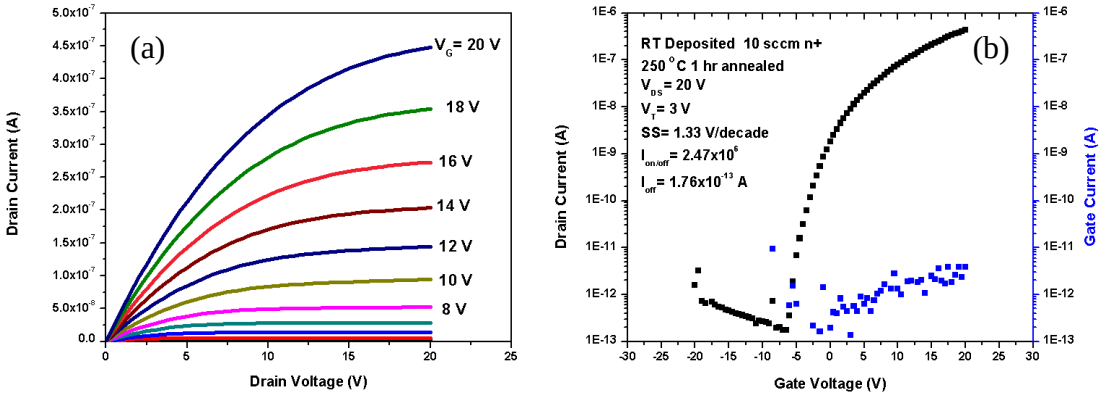

Figure 4.34. RT 250 °C 1hr 10 sccm O_2 TFT with n^+ Si substrate a) output and b) transfer characteristics.

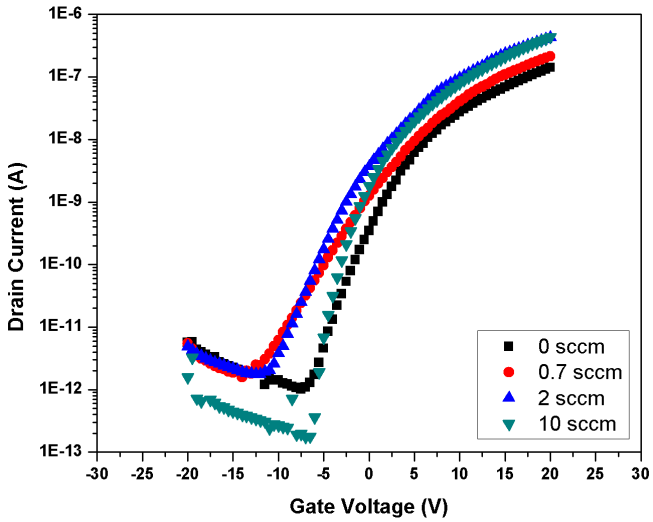

Figure 4.35. Transfer characteristics of RT 250 °C 1hr TFTs with various O_2 flows on n^+ Si substrate.

Table 4.10. Comparison of the effects of oxygen flow on TFT performance

Oxygen Flow (sccm)	I_D (A)	V_T (V)	SS (V/decade)	$I_{on/off}$	I_{off} (A)
0	$1.41x10^{-7}$	2	2.83	$1.37x10^5$	$1.02x10^{-12}$
0.7	$2.13x10^{-7}$	2	4.5	$1.34x10^5$	$2.46x10^{-12}$
2	$4.26x10^{-7}$	0.5	3	$2.42x10^5$	$1.76x10^{-12}$
10	$4.34x10^{-7}$	3	1.33	$2.47x10^6$	$1.76x10^{-13}$

4.2.2.5. Deposition and annealing temperature

After optimization of the production process, the influence of deposition temperature and annealing temperature were revisited. During this experiment RT as-deposited devices (not shown) were nonfunctional. Figure 4.36 through Figure 4.38 shows the output and transfer characteristics of the RT deposited devices with annealing temperatures of 150, 250, and 350 °C respectively. The RT 150 °C annealed device was operable though not optimally, but with continued annealing the performance of RT TFTs improved. An increase in I_D of 3 orders of magnitude was achieved for RT devices when annealing temperature was increased from 150 ˚C to 350 ˚C. The I_D for all annealed ET TFTs was of the order of 10^{-6} A, illustrating that annealing temperatures of up to 350 °C have no effect on I_D. The output and transfer characteristics of the ET deposited devices with no annealing and annealing temperatures of 150, 250, and 350 °C respectively are shown in Figure 4.39 through Figure 4.42. There was an increase in $I_{on/off}$ by an order of magnitude for every 100˚C increase in annealing temperature for RT devices, whereas ET devices remained relatively constant. The V_T of RT TFTs showed a shift in the negative direction as annealing temperature is increased. This shift results in a change in operation mode of the devices from enhancement to depletion. Conversely, for ET TFTs a trend of devices changing from depletion to enhancement mode was observed for ET TFTs. The negative shift in RT TFTs' characteristics is clearly evident in the shift observed in the corresponding transfer curves of Figure 4.43a. The shift in ET TFTs' transfer curves is shown in Figure 4.43b.

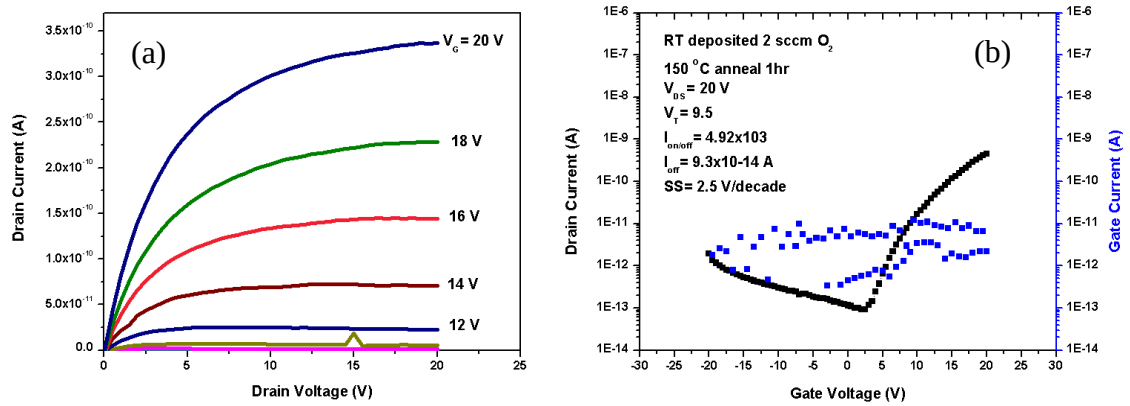

Figure 4.36. RT 150 °C 1hr 2 sccm O_2 TFT a) output and b) transfer characteristics.

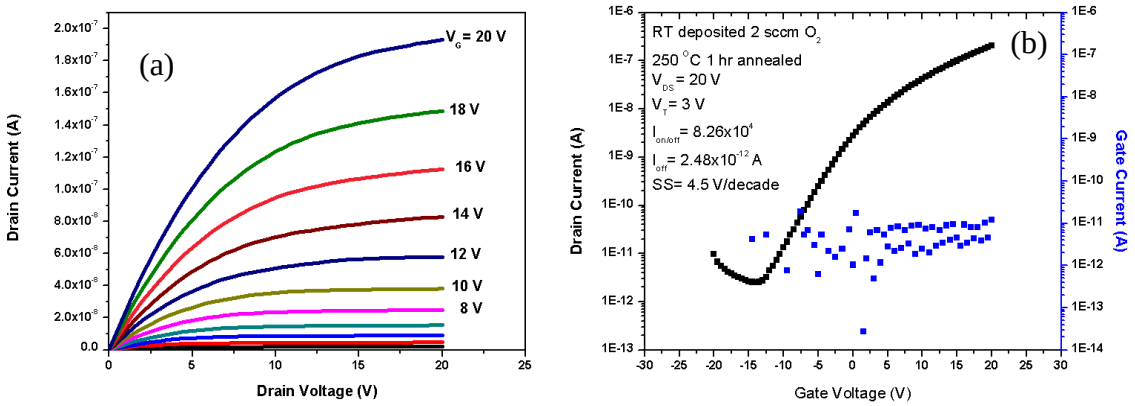

Figure 4.37. RT 250 °C 1hr 2 sccm O_2 TFT a) output and b) transfer characteristics.

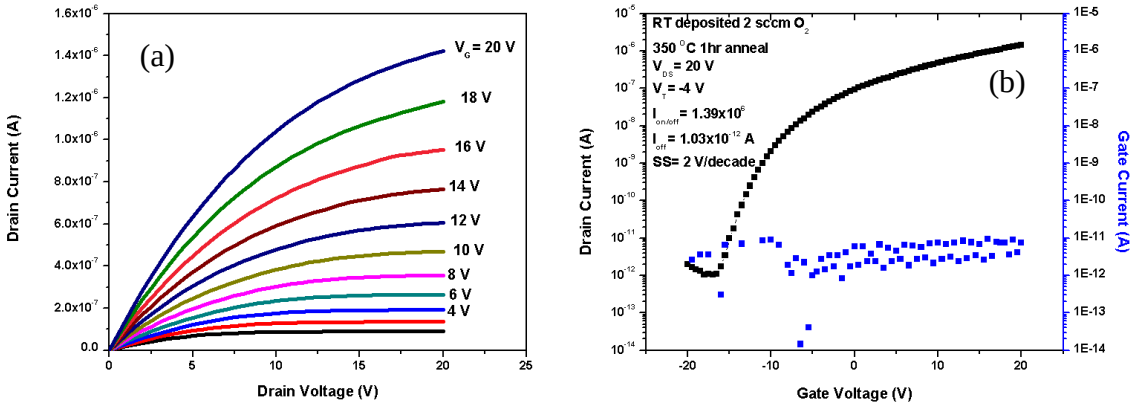

Figure 4.38. RT 350 °C 1hr 2 sccm O_2 TFT a) output and b) transfer characteristics.

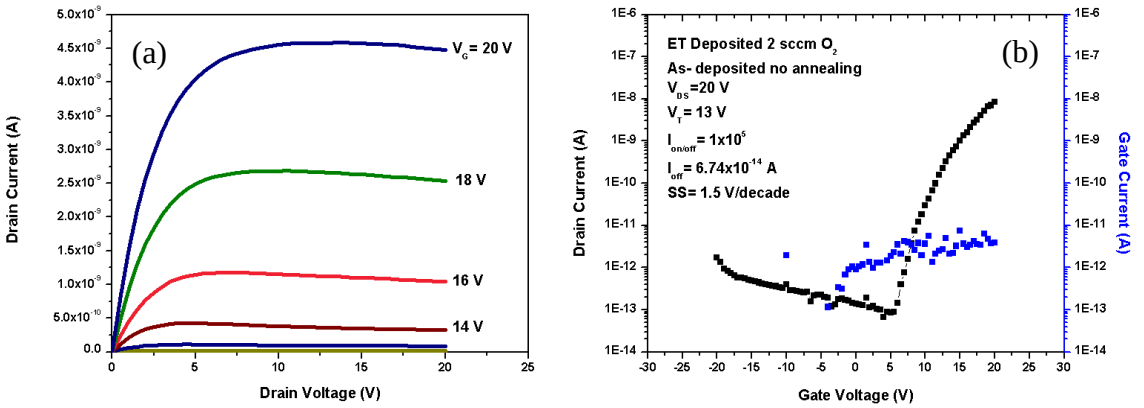

Figure 4.39. ET as-dep 2 sccm O_2 TFT a) output and b) transfer characteristics.

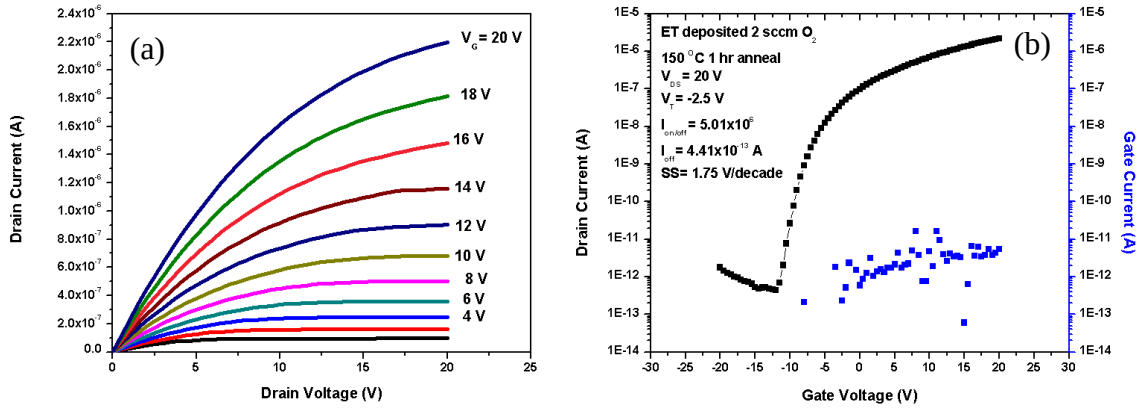

Figure 4.40. ET 150 °C 2 sccm O_2 TFT a) output and b) transfer characteristics.

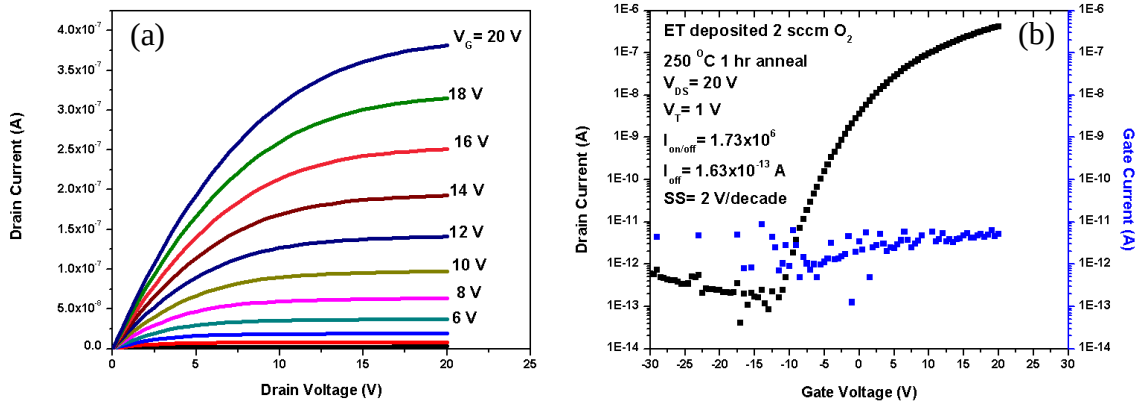

Figure 4.41. ET 250 °C 2 sccm O_2 TFT a) output and b) transfer characteristics.

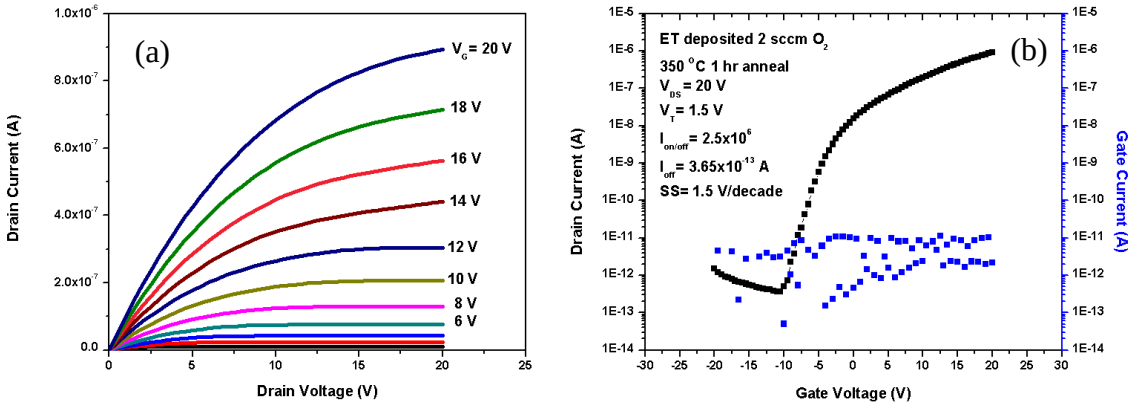

Figure 4.42. ET 350 °C 2 sccm O_2 TFT a) output and b) transfer characteristics.

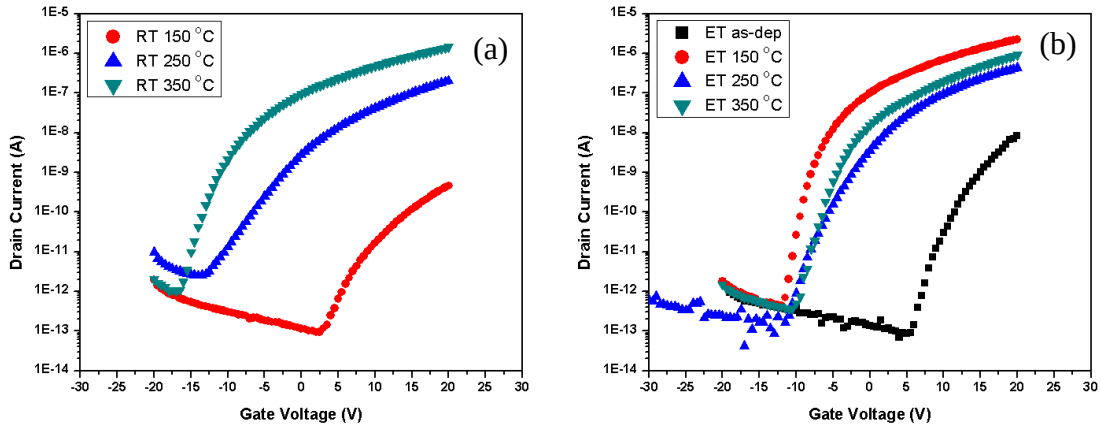

Figure 4.43. Effect of annealing temperature with respect to deposition temperature a) RT and b) ET.

Investigation into the influence of deposition temperature shows that devices produced at RT with no annealing are inoperable (as mentioned above) as opposed to those produced at ET which were functional though not well performing. Figure 4.44 illustrates the V_T and I_D characteristics for both RT and ET devices with similar annealing. RT and ET are shown to have similar characteristics when annealed at 250 °C. Table 4.11and Table 4.12 show the characteristics of RT and ET devices respectively, with varied annealing temperatures.

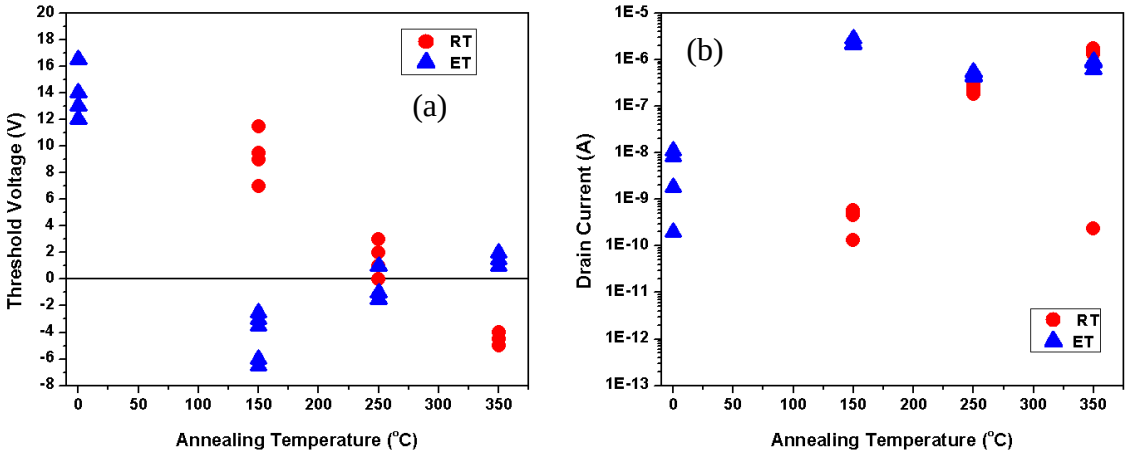

Figure 4.44. Effect of annealing temperature with respect to deposition temperature a) V_T and b) I_D.

Table 4.11. Characteristics of RT TFTs with various annealing temperatures

Annealing temperature (°C)	I_D (A)	V_T (V)	SS (V/decade)	$I_{on/off}$	I_{off} (A)
150	4.57E-10	9.5	2.5	4.92E+03	9.30E-14
250	2.05E-07	3	4.5	8.26E+04	2.48E-12
350	1.43E-06	-4	2	1.39E+06	1.03E-12

Table 4.12. Characteristics of ET TFTs with various annealing temperatures

Annealing temperature (°C)	I_D (A)	V_T (V)	SS (V/decade)	$I_{on/off}$	I_{off} (A)
0	8.44E-09	13	1.5	1.00E+05	6.74E-14
150	2.21E-06	-2.5	1.75	5.01E+06	4.41E-13
250	4.26E-07	1	2	1.73E+06	1.63E-13
350	9.12E-07	1.5	1.5	2.50E+06	3.65E-13

4.2.2.6. Electrical stability

Device stability was investigated for both high and low electric field conditions with various oxygen incorporations. The V_T of stressed devices was taken to be the voltage where I_D crosses through 5 pA. The stress tests show both a decrease in I_D and a

minimal positive shift in V_T with stress time up to 10^3 sec. Beyond 10^3 sec the changes become more significant, but V_T still remains under 5 V. Devices fabricated with a 2 sccm oxygen flow yielded the most stable results throughout the stress period (Figure 4.45). The low field 0 sccm and 10 sccm devices exhibited similar results, being the most change in V_T and I_D occurred at 10^3 sec. Under the influence of high field 0 sccm illustrates the most change in characteristics, with the onset of the V_T variation beginning during the first stress period. The transfer characteristics of the stressed devices are shown in Figure 4.46(low field) and Figure 4.47(high field).

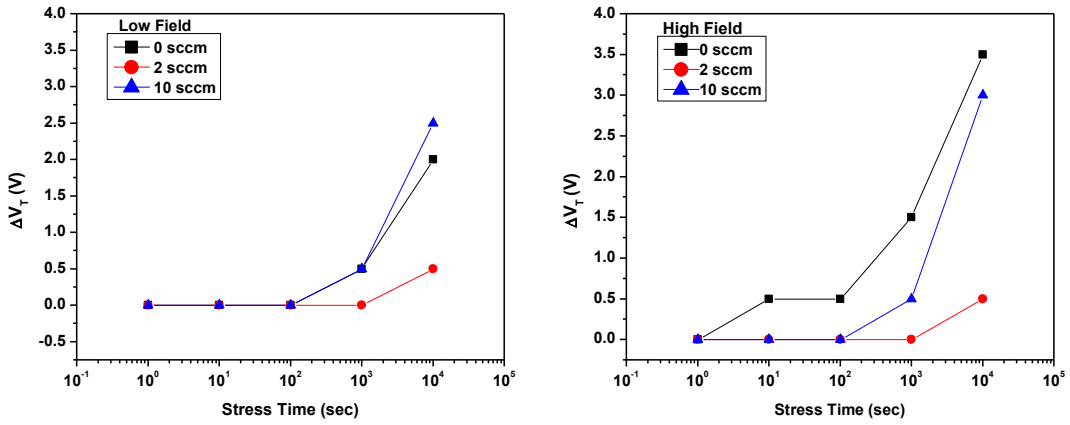

Figure 4.45. Effect of stress on V_T

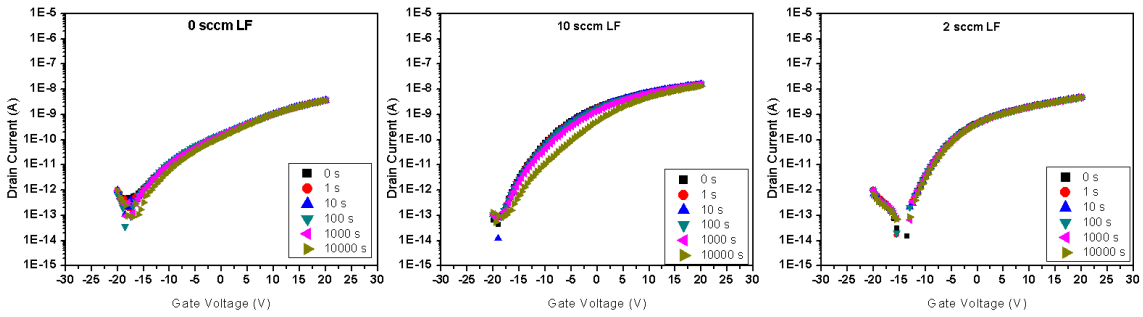

Figure 4.46. LF stress transfer.

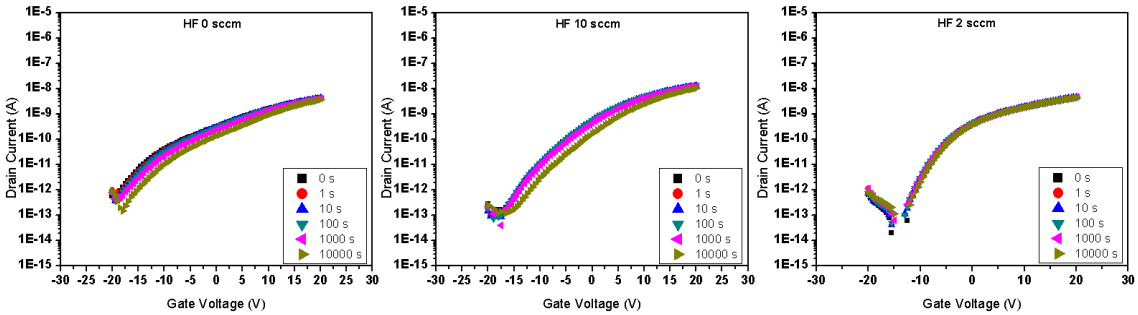

Figure 4.47. HF stress transfer.

4.2.2.7. Photoexcitation

Devices were subjected to photoexcitation to gain insight into the nature of the trapping mechanisms within the film. Excitation energy with respect to O_2 flow shows a negative shift in V_T as excitation energy and O_2 flow is increased. TFTs with an oxygen flow of 10 sccm exhibited the least change in transistor performance with change in photoexcitation energy, shown in Figure 4.48a. The characteristics extracted from the transfer curve are significantly changed when there is no oxygen flow during deposition, as seen in Table 4.13 for red laser excitation and Table 4.14 for green. The D_{it} was calculated using Equation 4-1. Comparison of D_{it} values show a reduction of interface traps with increasing oxygen flow. The mobility of devices with various oxygen flows was calculated, and is shown in Table 4.15. Mobility is shown to increase with oxygen incorporation.

$$\Delta D_{it} = \frac{C_{ox}}{\ln(10) qkT} (SS_{after} - SS_{before}) \qquad \textbf{4-1}$$

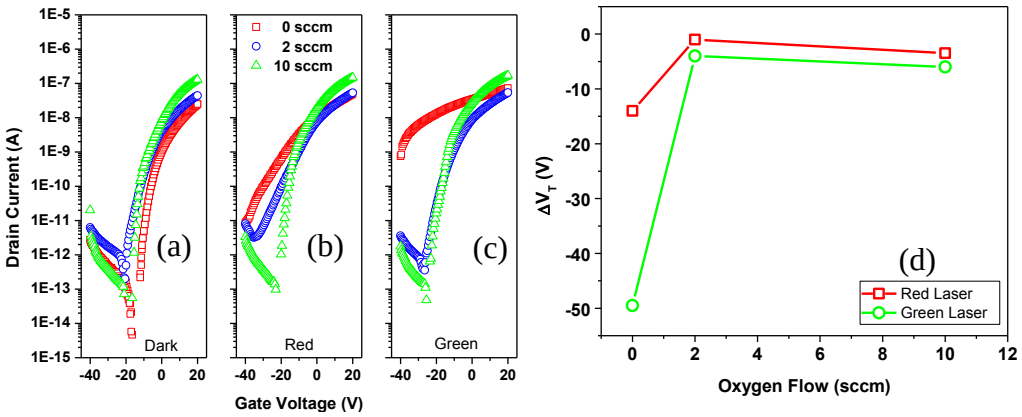

Figure 4.48. The of photoexcitation with respect to oxygen incorporation.

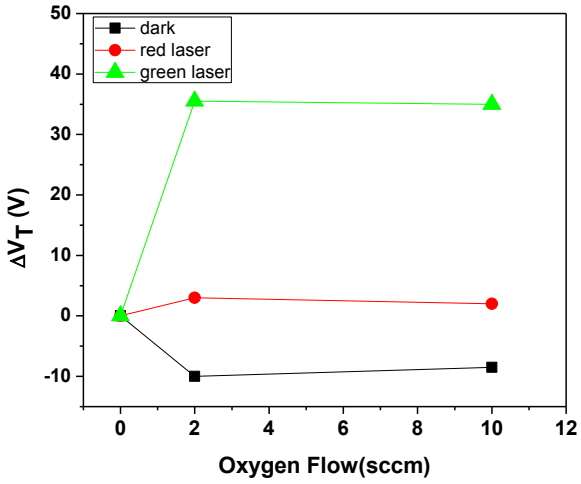

Figure 4.49. Change in V_T due to photoexcitation with respect to 0 sccm oxygen flow.

Table 4.13. Comparison of the effects of oxygen flow on TFT performance when excited by red (1.94 eV) laser

Oxygen Flow (sccm)	ΔV_T (V)	ΔSS (V/decade)	ΔI_{off} (fA)	D_{it} (cm^{-2} eV^{-1})
0	-14	6.5	Not measurable	Not measurable
2	-1	0	-298	1.015E+12
10	-3.5	0.25	71.9	6.621E+11

Table 4.14. Comparison of the effects of oxygen flow on TFT performance when excited by green (2.33 eV) laser

Oxygen Flow (sccm)	ΔV_T (V)	ΔSS (V/decade)	ΔI_{off} (fA)	D_{it} (cm^{-2} eV^{-1})
0	-49.5	Not measurable	Not measurable	Not measurable
2	-4	3.75	1999	6.248E+11
10	-6	0.25	-41.2	3.675E+11

Table 4.15. Mobility based on oxygen flow

Oxygen Flow (sccm)	Mobility (cm^2 V^{-1} s^{-1})
0	0.156
2	0.436
10	0.716

When observing the influence of deposition temperature on trap states, ET TFTs (Figure 4.50a) show a greater change in SS and I_{off} than that of the RT device with increasing excitation energy. The SS value of ET becomes immeasurable with increased photoexcitation, and there is a 40 V change in V_T under the green laser, see Table 4.16 (red laser) and Table 4.17 (green laser).

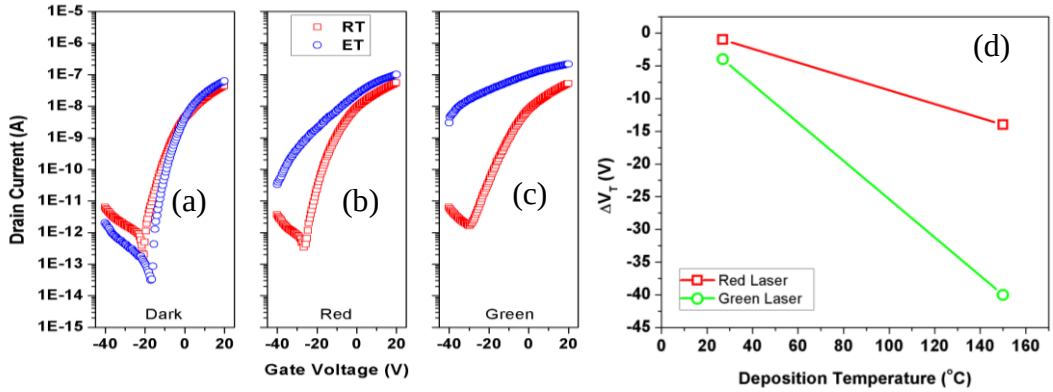

Figure 4.50. The of photoexcitation with respect to deposition temperature.

Table 4.16. Comparison of the effects of deposition temperature on TFT performance when excited by red (1.94 eV) laser

Deposition Temperature (°C)	ΔV_T (V)	ΔSS (V/decade)	ΔI_{off} (fA)
27 (RT)	-1	0	-298
150 (ET)	-14	Not measurable	Not measurable

Table 4.17. Comparison of the effects of deposition temperature on TFT performance when excited by green (2.33 eV) laser

Deposition Temperature (°C)	ΔV_T (V)	ΔSS (V/decade)	ΔI_{off} (fA)
27 (RT)	-4	3.75	2.00E+03
150 (ET)	-40	Not measurable	Not measurable

A similar behavior is also observed with annealing temperature, where the higher temperature invokes greater change in the characteristics with increased excitation energy (Figure 4.51a). For 350 °C annealing, characteristics for the red laser were invariant from that of the non-excited measurements, see Table 4.18. Under green laser excitation the 350 °C annealed device demonstrated a larger shift in V_T as well as the SS value being larger than that of 250 °C, see Table 4.19.

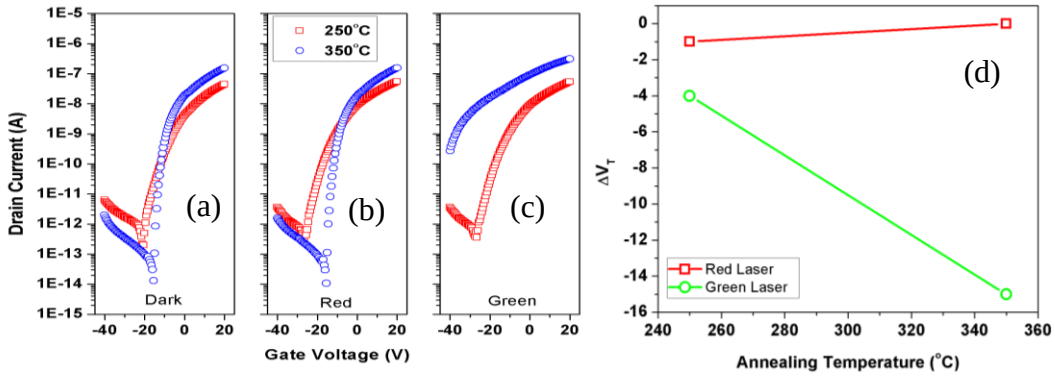

Figure 4.51. The of photoexcitation with respect to annealing temperature.

Table 4.18. Comparison of the effects of annealing temperature on TFT performance when excited by red (1.94 eV) laser

Annealing Temperature (°C)	ΔV_T (V)	ΔSS (V/decade)	I_{off} (fA)
250	-1	0	-298
350	0	0.25	-2.3

Table 4.19. Comparison of the effects of annealing temperature on TFT performance when excited by green (2.33 eV) laser

Annealing Temperature (°C)	ΔV_T (V)	ΔSS (V/decade)	ΔI_{off} (fA)
250	-4	3.75	2.00E+03
350	-15	Not measureable	Not measureable

CHAPTER 5

DISCUSSION

Deposition and post-deposition parameters are significantly influential in optimizing the characteristics of GSZO films and their resulting devices. The amount of oxygen incorporated during deposition has been shown to decrease transparency, alter film composition, and vary TFT performance. The variation in the concentration of O_I is correlated to a change in oxygen vacancies, and the discussion is thereby based on this.

5.1 Oxygen flow

As previously mentioned, the elemental at. concentrations were slightly varied as O_2 was increased during deposition. Zn concentrations are shown to increase with increased O_2 flow as opposed to the O at. % (illustrated in Figure 4.7). The differing trends of O_2 flow and O at. % is attributed to both a reduction in surface point defects and the chemisorption of O_2 molecules onto the films surface. Surface defects are reduced with increased O_2 during deposition, thereby reducing the dangling bonds available to induce chemisorption [145], and hence reducing the concentration of oxygen on the surface, as well as O_I/O_{II} ratio (shown in Figure 5.1).

In addition, Zn vacancies were explored as a result of the observed dependence on oxygen. To investigate this, the relationship between O_{II} and the deconvoluted C peaks was determined. The O_{II} peaks were shown to be proportional to C and therefore the presence of zinc vacancies was excluded as a possibility. Hence, the O_{II} peak is said to be solely resultant of absorbed species.

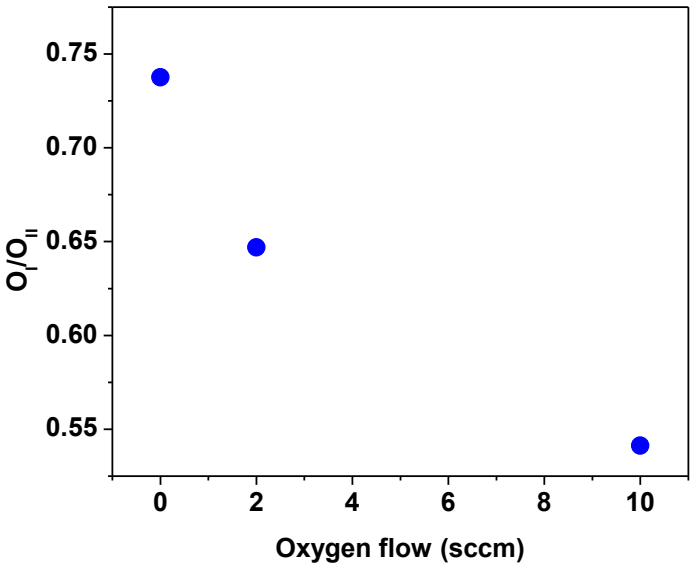

Figure 5.1. Variation in O_I/O_{II} with oxygen flow introduced during deposition.

Another effect of oxygen, which is consistently reported throughout the literature on ZnO and ZnO based material systems is the ability to increase film resistivity. This could not be verified in this work quantitatively, as the resistance of the films was beyond measurement capabilities of the Hall system. Instead the resistance was qualitatively inferred from the V_T of devices measured, though it is understood that other processing factors contribute to the V_T values. V_T shows a linear relationship with Ga/O_I ratio (Figure 5.2). This proportional dependence is expected since Ga is considered as scavenger of oxygen vacancies due to its strong bonding with oxygen. Therefore as the Ga/O_I ratio increase, the carrier concentration in the film is thought to decrease. This is verified with the consequent shift in V_T towards positive direction as well as increase in I_{off} (Figure 5.3). The variation in V_T and I_{off} with Ga/O_I ratio is due to the change in Ga occurring in the film. However, the SS value is found to be inversely varying with Ga/Sn

ratio (Figure 5.4). This is understandable as increase in Ga/Sn represents higher mobility with decreased oxygen vacancy and hence decreases the SS.

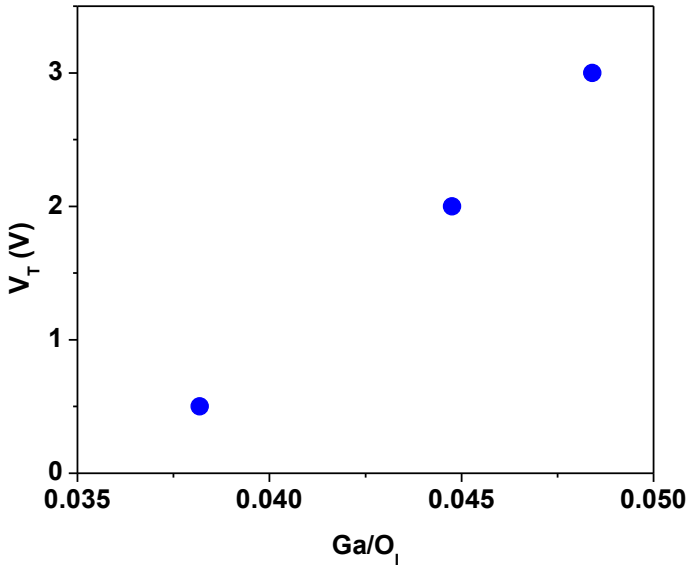

Figure 5.2. Variation in V_T with Ga/O_I ratio.

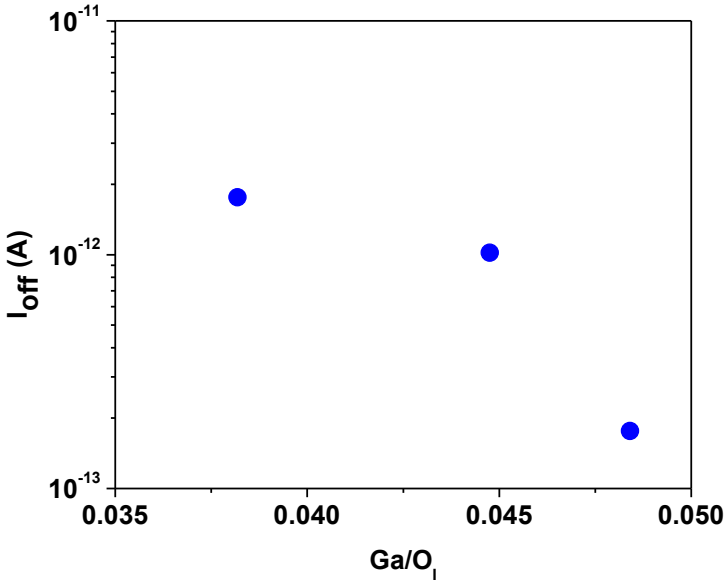

Figure 5.3. Variation of I_{off} with Ga/O_I ratio.

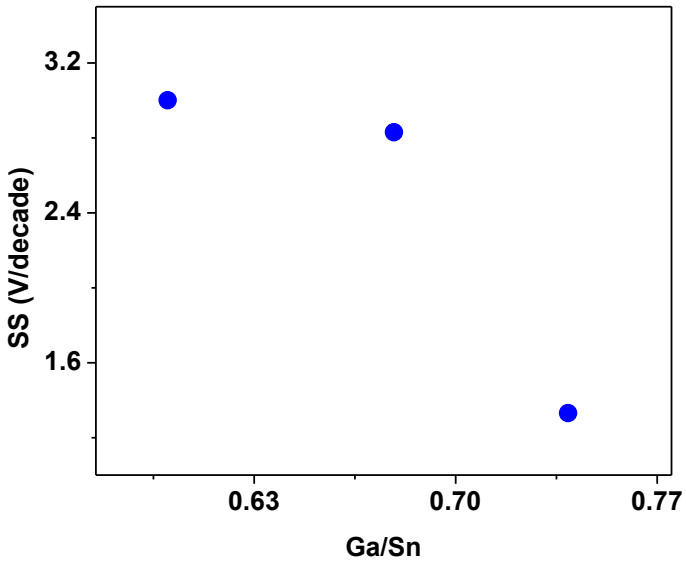

Figure 5.4. Variation of SS value with Ga/Sn ratio.

The stability tests (electrical stress and photoexcitation) conducted demonstrates a change in degradation and performance of devices based on oxygen incorporation. The instability of the 0 sccm oxygenated device is due to the absorption of negatively charged oxygen species during the stress period. Instability of the 10 sccm oxygenated device is due to increased electron trapping within existing traps, not increased trap creation. This increased trapping is due to an increased carrier concentration. The theory for the behavior of the 10 sccm device is in agreement with the conclusion drawn by Kim et al. [147].

5.2 Deposition and annealing temperature

There is consensus amongst published literature that in addition to oxygen incorporation, the effects of deposition and annealing temperature have the ability to significantly alter the characteristics of ZnO based active layers. This observation is also illustrated throughout the presented work. The influence of deposition temperature is

blatantly illustrated by the inoperability of devices with RT as-deposited active layers, where ET as-deposited devices were operational though not optimally. The difference in the functionality of these as-deposited devices is resultant of the annihilation of inherent defects, and improvement of the local arrangement of atoms by the higher thermal energy supplied during the ET deposition. The oxygen incorporation is also reduced at high deposition temperature. Substrate heating was also found to be effective in reducing the required annealing temperature for which significant changes in device characteristics such as V_T and SS are observed.

RT and ET annealed films, possess Sn/Zn atomic fractions close in value, and show similar behaviour with annealing temperature. The major differences between the RT and ET films are the variations of the Zn/O_I and O_I/O_{II} ratios, which are complimentary to each other with increased annealing temperature. Both of these differences explain the observed opposite modes of operation of the devices.

Zn/O_1 decreases with annealing temperature Figure 5.5, while the O_I/O_{II} increases with annealing temperature Figure 5.6 though it is more linear in the case of RT annealed samples. Both data sets indicate that with the increase in annealing temperature, Zn/O_1 decreases which imply that carrier concentration increases with V_T increasing. The increasing value of O_I/O_{II} indicates that on annealing there are more oxygen vacancies being created resulting in increase in carrier concentration. In the case of ET films however, Zn/O_I increases with the annealing temperature while the O_I/O_{II} decreases with the annealing temperature, excluding the sample at 150 °C which does not fit the data. Also O_I/O_{II} is quite high for the ET samples as compared to RT annealed samples. The

higher O_I/O_{II} implies higher carrier concentration and hence the V_T is negative and with increasing annealing temperature it shifts to the positive side with decreasing O_I/O_{II}.

All TFTs illustrate a possible relationship between Zn/O_I and V_T, where V_T increases as the Zn/O_I ratio Figure 5.7 increases. This relationship appears to be primarily dependent on the atomic percent of oxygen in that there is a decrease in V_T as O atomic percent increases. The decrease of V_T with increase in O atomic percent as well as O_I relative percent is consistent with what is expected. As O atomic percent increases there is an increase in O vacancies which thereby increases carrier concentration, channel conductivity, I_{off}. Regarding annealing, the O_I/O_{II} ratio of the RT films increases with increased annealing signifying increased oxygen vacancies in the system.

SS decreases drastically with Sn/O_I ratio Figure 5.8 but does not vary significanlty in the case of ET films. The difference in the behavior can be explained that in the RT films the improvement of defect is significant hence the mobility variation could be higher with increase in Sn/O_I while in the case of ET films as the deposited films are already less defective, increased Sn does not significanlty affect the films. Also it is to be pointed out that normally the changes in V_T and I_{off} are associated with the bulk traps and variations in SS are associated with the interface states. So both the Zn and Ga atomic concentration impacts bulk traps while Sn/O_I appears to affect the interface state density. Figure 5.9 clearly illustrates the dependence of $I_{on/off}$ on the Sn/Ga ratio, and shows that the Sn/Ga should not exceed 1.4 in order to maintain at least an $I_{on/off}$ of 10^6.

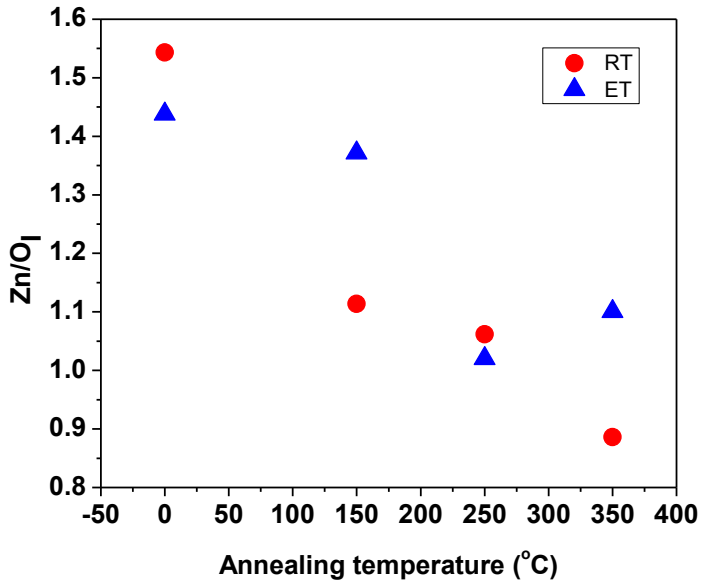

Figure 5.5. Dependence of Zn/O_I with annealing temperature.

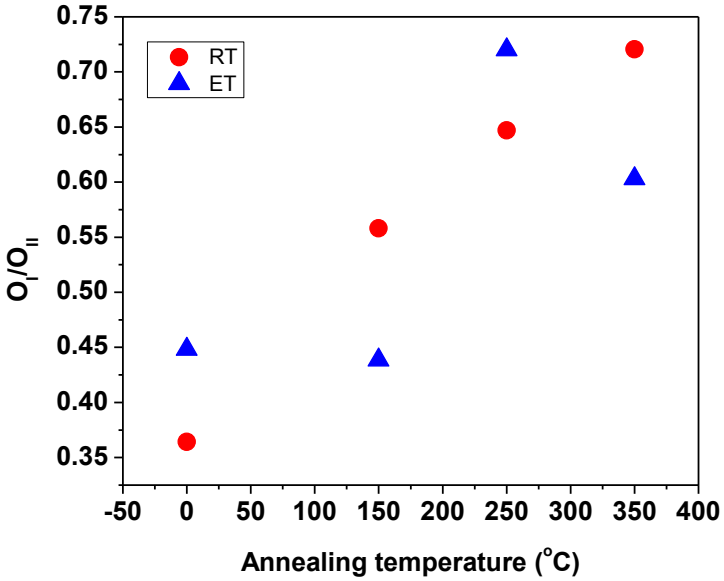

Figure 5.6. Dependence of O 1s components on annealing temperature.

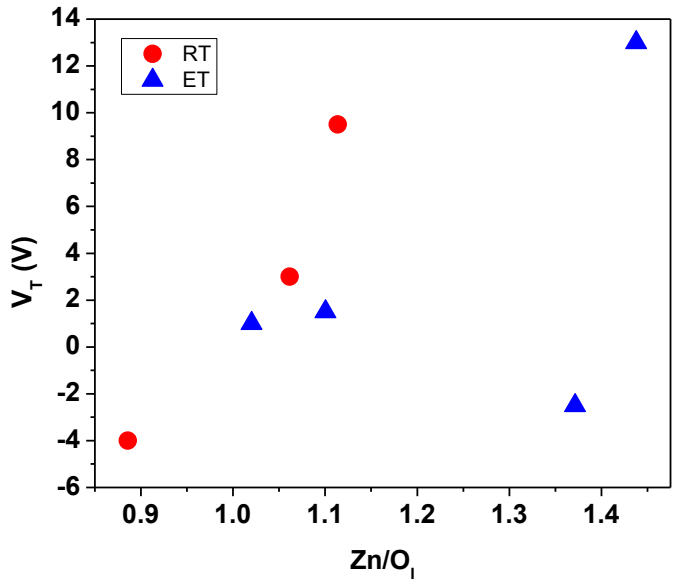

Figure 5.7. V_T dependence on Zn/O_I ratio.

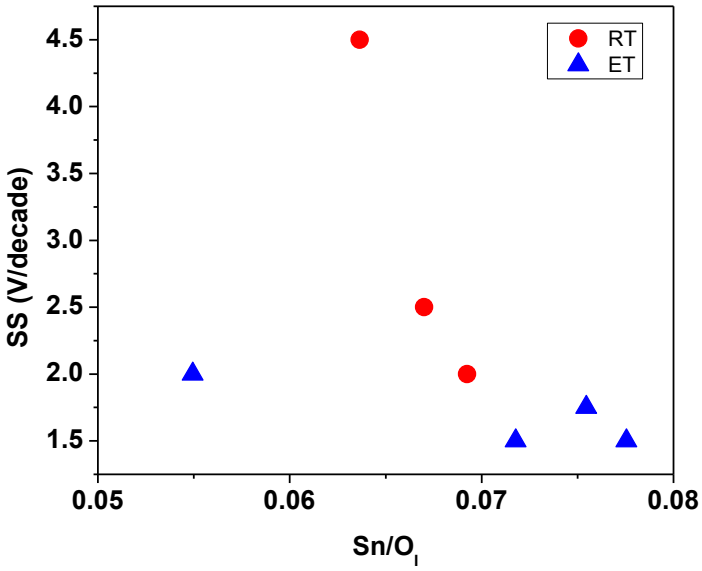

Figure 5.8. SS dependence on Sn/O_I ratio.

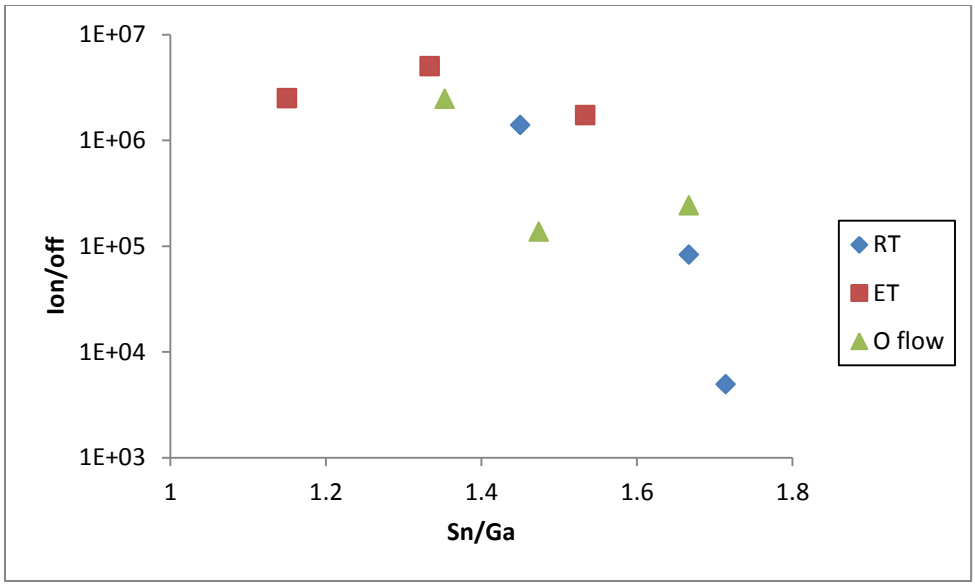

Figure 5.9. Influence of Sn/Ga ratio on $I_{on/off}$.

In addition to annealing temperature, the annealing duration and ambient were investigated. Annealing duration refers back to the comparisons of Figure 4.25, Table 4.6 and Table 4.7, which highlights a negative shift in V_T with increased annealing time. This negative shift is attributed to the active layers being more conducting with increased annealing duration. The influence of annealing ambient proved to have significant effects on the performance of the devices. Our findings being similar to that of Huang et al. [50], where vacuum yields the lowest resistivity, followed by air, then nitrogen. With air annealing held as the baseline standard, the various resistivities resulting from vacuum and nitrogen are commonly attributed [148] to an increase in oxygen vacancies and production of acceptors, respectively.

Various mechanisms that are commonly attributed to influence the stabilty of ZnO and ZnO based AOS devices are interface traps, chemisorption of oxygen, and defect creation in the channel. The distinction between each of these can be made by the

observed changes in SS, V_T, and I_{off} . For instance, during photoexcitation TFTs demonstrating a change in SS accompanied with a negative shift in V_T are indicative of electrons detrapping from the states during laser illumination. More specifically, the changes in SS and V_T occuring without an increase in I_{off} signifies detrapping of electrons from the interface states only [149].

When illuminated by the red and green laser respectively, TFTs produced with 0 sccm flow oxygen exhibit the largest variation in SS and V_T in contrast to the TFTs with higher oxygen incorporations of 2 and 10 sccm. The large variations in the characteristics of oxygen deficient TFTs even under red laser illumination indicate the existence of shallow traps, consistent with the reports on pulsed laser deposited ZnO films [150] where it was found that channel layers deposited under oxygen deficient conditions are more defective with traps located at 0.32 eV below the conduction band edge. It is to be noted that the traps refer to both the traps in the channel and the interface traps. The light illumination has been shown [149, 151] to create doubly ionized oxygen vacancy defects, V_O^{2+} , from the neutral oxygen vacancy, V_O, already existing in the channel. This also manifests in enhanced interface trap density in these ZnO and the associated AOS systems [149]. As a result, the observed shift in V_T with illumination is always negative due to electrons detrapping from the trap states as well as from the interface states. A comparatively smaller change of V_T, SS and I_{off} values for the 2 sccm oxygen incorporation occurs when illuminated by the green laser compared to the results collected in the dark. Further, the variation in V_T between 0 sccm and 2 sccm oxygen incorporation is indicative of significant reduction in the density of trap states in the 2

sccm device. Further, for the largest oxygen incorporation of 10 sccm, a minimal change in V_T accompanied with considerably invariant SS and I_{off} under excitation from both lasers represent continued reduction in trap density. The inherent defects within the channel layer of the oxygen deficient device highlighted during photoexcitation measurements were also observed under stress tests. However, the instability in this case is represented by a positive shift in V_T with SS being invariant. Further, instability with respect to gate bias stress was also observed in the TFT fabricated at the other extreme oxygen condition of 10 sccm. These variations under stress manifest only in V_T shift and not SS. The lowest V_T shift observed in 2sccm can be explained in terms of the difference in the location of the quasi Fermi levels at the interface between this TFT and the other two TFTs. It is to be noted that the V_T values are similar -2 V and -1 V for 0 and 10 sccm , respectively, despite other differences in these two samples, while it is -3 V for 2 sccm. Hence, it speculated that for 2 sccm the quasi Fermi level is quite low closer to the mid gap level and the changes due to the charge trapping comparatively have minimal effect in the V_T shift. As the device is fairly stable under photoexcitation as well as the stress condition for the intermediate oxygen incorporation of 2 sccm this deposition condition was chosen for further investigating the effect of subtrate and annealing temperatures, despite the slightly inferior transfer characteristics to those of 10 sccm oxygen flow.

The photoexcitation results on 250 °C annealed ET devices are also consistent, in that higher drain current and larger negative shifts in V_T are observed on illumination, indicative of enhanced detrapping of electrons than 250 °C RT devices. Similar changes

on green illumination are observed for RT device at higher annealing temperature of 350 °C. This clearly indicates depending on the deposition and annealing combination one can change the energetic distribution of the interface states in the gap.

Thus our findings show that it is possible to achieve enhancement and depletion mode devices through different combinations of oxygen partial pressures during deposition as well as deposition plus post-deposition annealing temperatures, with both remaining below 250 °C, thus making the entire process compatible for potential applications on flexible substrates. Further these can be judiciously chosen to get a stable performance both with respect to the bias stress as well under illumination, a great practical importance for potential applications in highly stable transparent TFTs.

CHAPTER 6

CONCLUSION

GSZO films of 30nm have been deposited by rf sputtering at both RT and ET with varied oxygen partial pressures. The films produced are amorphous within the temperature ranges of this investigation. Transparency typically above 80% in the visible region were observed for films with at least 2 sccm oxygen incorporation during deposition, with an optical band gap of approximately 3.1 eV. All the data have been explained by delineating the O 1s XPS peak into two peaks with the first one at lower binding energy attributed to the metal oxides and oxygen vacancies. The second peak at higher binding energy to chemisorbed species on the surface. The changes that were observe in O_2 flow as well as in the annealing temperature depend on the variation that occurs in the elemental atomic concentration of the films which is correlated to the variations in the oxygen vacancies through O_I peak . It is to be noted that zinc vacancies were also considered as a contributing factor in the variation of film composition, but was excluded after further investigation. GSZO depletion mode TFTs have been fabricated with I_D of 10^{-6} A, V_T of -3 V, SS of 1.3 V/decade, and $I_{on/off}$ of 10^6 when operated in the dark without gate stress. The trap density, defect creation in the layer and oxygen chemisorption play a critical role in determining the operational characteristics of the device, all which can be controlled by the oxygen incorporation and temperature during deposition, along with post-deposition annealing. Device instability, with respect to the electrical stress and optical illumination, can be suppressed by suitably tailoring these parameters. TFTs with 10 sccm oxygen incorporation deposited 50 μm x 50 μm channel

with post-deposition annealing at 250 °C exhibits the best performance in enhancement mode with $I_D = 10^{-7}$A, $V_T = 3$ V, SS = 1.3 V / decade, and $I_{on/off} = 10^6$. Mobility values are shown to increase with oxygen incorporation, and are low compared to the literature. A stable TFT has been achieved under electrical stress for the intermediate 2 sccm RT deposition with 250 °C annealing condition, exhibiting ΔV_T as low as ~0.5 V for 3hour stress under a gate bias of 1.2 and 12 V, while optical stability has been achieved at 10 sccm oxygen deposition and 250 °C annealing condition.

CHAPTER 7

RECOMMENDATIONS

Due to the lack of information on the GSZO material system and its characteristic influence on resulting device behavior, there remain unexplored/underexplored phenomena. Regarding, film characterization the following areas would prove beneficial. First, additional XPS analysis conducted within a week of deposition. This analysis should be performed without sputtering of surface oxide and with sputtering. In addition analysis should be further by including depth profiling. Secondly, Hall measurements for highly resistive films should be performed to give quantified insight into the effects of deposition parameters and post deposition techniques on the film characteristics. Regarding TFT production the next step would be fabrication on a flexible substrate, and it is the advice of the author to further reduce the active layer area so that it does not protrude from under the source and drain electrodes. In reference to device characterization, RT TFTs should be produced with active layers that are annealed at temperatures above 350 °C, in an attempt to observe a positive migration in V_T as in that of the ET samples. In addition, photoexcitation measurements should be repeated using lasers of the same power density. To complement the photoexcitation measurements, capacitance – voltage measurements should also be performed to identify the density of traps, as it was not achievable during this work. Lastly, it is the suggestion of the author to modify the target composition with a higher Sn atomic fraction to improve the attainable I_D within the 0 – 10 V V_{DS} and V_G range. These recommendations are resultant

from the deposition, processing, fabrication, and testing experience acquired during this research work.

REFERENCES

1. Chopra, K.L., S. Major, and D.K. Pandya, *Transparent conductors—A status review.* Thin Solid Films, 1983. **102**(1): p. 1-46.

2. Klingshirn, C., *ZnO: From basics towards applications.* physica status solidi (b), 2007. **244**(9): p. 3027-3073.

3. Exarhos, G.J. and X.D. Zhou, *Discovery-based design of transparent conducting oxide films.* Thin Solid Films, 2007. **515**(18): p. 7025-7052.

4. Fortunato, E., et al., *Zinc oxide, a multifunctional material: From material to device applications.* Applied Physics A: Materials Science & Processing, 2009. **96**(1): p. 197-205.

5. Hosono, H., *Recent progress in transparent oxide semiconductors: Materials and device application.* Thin Solid Films, 2007. **515**(15): p. 6000-6014.

6. Kamiya, T., K. Nomura, and H. Hosono, *Present status of amorphous In–Ga–Zn–O thin-film transistors.* Science and Technology of Advanced Materials, 2010. **11**: p. 044305.

7. Kwon, J.Y., D.J. Lee, and K.B. Kim, *Review paper: Transparent amorphous oxide semiconductor thin film transistor.* Electronic Materials Letters, 2011. **7**(1): p. 1-11.

8. Özgür, Ü., et al., *A comprehensive review of ZnO materials and devices.* Journal of Applied Physics, 2005. **98**: p. 041301.

9. Kumomi, H., et al., *Materials, Devices, and Circuits of Transparent Amorphous-Oxide Semiconductor.* Journal of Display Technology, 2009. **5**(12): p. 531-540.

10. *Oxide Thin Film Transistor Technology Status and Development Status*, 2011.

11. Jeong, J.K., *The status and perspectives of metal oxide thin-film transistors for active matrix flexible displays.* Semiconductor Science and Technology, 2011. **26**: p. 034008.

12. Palmer, G. and K. Poeppelmeier, *Phase relations, transparency and conductivity in Ga2O3---SnO2---ZnO.* Solid state sciences, 2002. **4**(3): p. 317-322.

13. Fortunato, E.M., *High mobility indium free amorphous oxide thin film transistors.* Appl. Phys. Lett., 2008. **92**(22): p. 222103.

14. Hosono, H., et al., *Factors controlling electron transport properties in transparent amorphous oxide semiconductors.* Journal of non-crystalline solids, 2008. **354**(19-25): p. 2796-2800.

15. Ogo, Y., et al., *Amorphous Sn–Ga–Zn–O channel thin film transistors.* physica status solidi (a), 2008. **205**(8): p. 1920-1924.

16. MOON, J.H., et al., *OXIDE SEMICONDUCTOR THIN FILM AND FABRICATION METHOD THEREOF*, 2009, WO Patent WO/2009/119,968.

17. Riedl, T., P. Gorrn, and W. Kowalsky, *Transparent Electronics for See-Through AMOLED Displays.* Display Technology, Journal of, 2009. **5**(12): p. 501-508.

18. Jeong, Y., et al., *Bias-Stress-Stable Solution-Processed Oxide Thin Film Transistors.* ACS Applied Materials & Interfaces, 2010. **2**(3): p. 611-615.

19. Jeong, Y., et al., *Effect of gallium content on bias stress stability of solution-deposited Ga-Sn-Zn-O semiconductor transistors.* Thin Solid Films, 2011.

20. Kim, D.-H., et al., *Sputter-deposited Ga–Sn–Zn–O thin films for transparent thin film transistors.* physica status solidi (a), 2011. **208**(12): p. 2934-2938.

21. Kim, H.R., et al., *Effects of Ga Concentration on Electrical and Physical Properties of Amorphous Ga-Zn-Sn-O Semiconductor Thin Films.* Electrochemical and Solid-State Letters, 2011. **14**: p. H411.

22. Chin, S., *North Carolina research team to develop flexible displays for U.S. Army,* in *EE Times*2004.

23. Chopra, K., S. Major, and D. Pandya, *Transparent conductors--A status review.* Thin solid films, 1983. **102**(1): p. 1-46.

24. Freeman, A., et al., *Chemical and thin-film strategies for new transparent conducting oxides.* MRS Bulletin, 2000. **25**(8): p. 45-51.

25. Hosono, H., *Ionic amorphous oxide semiconductors: Material design, carrier transport, and device application.* Journal of non-crystalline solids, 2006. **352**(9-20): p. 851-858.

26. Nomura, K., et al., *Room-temperature fabrication of transparent flexible thin-film transistors using amorphous oxide semiconductors.* Nature, 2004. **432**(7016): p. 488-492.

27. Minami, T., *New n-type transparent conducting oxides.* MRS Bulletin, 2000. **25**(08): p. 38-44.

28. Facchetti, A. and T.J. Marks, *Transparent electronics: from synthesis to applications*2010: Wiley.

29. Flewitt, A., et al., *Stability of thin film transistors incorporating a zinc oxide or indium zinc oxide channel deposited by a high rate sputtering process.* Semiconductor Science and Technology, 2009. **24**: p. 085002.

30. Klingshirn, C., *ZnO: Material, Physics and Applications.* ChemPhysChem, 2007. **8**(6): p. 782-803.

31. Izyumskaya, N., et al., *Preparation and properties of ZnO and devices.* physica status solidi (b), 2007. **244**(5): p. 1439-1450.

32. Webb, J.B., D.F. Williams, and M. Buchanan, *Transparent and highly conductive films of ZnO prepared by rf reactive magnetron sputtering.* Applied Physics Letters, 1981. **39**(8): p. 640-642.

33. Bethke, S., *Luminescence of heteroepitaxial zinc oxide.* Appl. Phys. Lett., 1988. **52**(2): p. 138.

34. Ahn, C.H., et al., *Influence of the thermal annealing temperature of the channel layers grown at room temperature on the device performance in the ZnO thin-film-transistors.* Physica B: Condensed Matter, 2009. **404**(23–24): p. 4835-4838.

35. Jie, J., A. Morita, and H. Shirai, *Role of oxygen atoms in the growth of magnetron sputter-deposited ZnO films.* Journal of Applied Physics, 2010. **108**: p. 033521.

36. Im, S., *Ultraviolet emission and microstructural evolution in pulsed-laser-deposited ZnO films.* J. Appl. Phys., 2000. **87**(9): p. 4558.

37. Carcia, P., et al., *Transparent ZnO thin-film transistor fabricated by rf magnetron sputtering.* Applied Physics Letters, 2003. **82**(7): p. 1117-1119.

38. Murphy, T., K. Moazzami, and J. Phillips, *Trap-related photoconductivity in ZnO epilayers.* Journal of electronic materials, 2006. **35**(4): p. 543-549.

39. Chowdhury, M.D., *Light induced instabilities in amorphous indium gallium zinc oxide thin-film transistors.* Appl. Phys. Lett., 2010. **97**(17): p. 173506.

40. Liu, Y., et al., *Ultraviolet detectors based on epitaxial ZnO films grown by MOCVD.* Journal of electronic materials, 2000. **29**(1): p. 69-74.

41. Roth, A.P. and D.F. Williams, *Properties of zinc oxide films prepared by the oxidation of diethyl zinc.* Journal of Applied Physics, 1981. **52**(11): p. 6685-6692.

42. Mandalapu, L.J., *Low-resistivity Au/Ni Ohmic contacts to Sb-doped p-jour ZnO.* Appl. Phys. Lett., 2007. **90**(25): p. 252103.

43. Lee, S., et al., *Combined effect of the target composition and deposition temperature on the properties of ZnO:Ga transparent conductive oxide films in pulsed dc magnetron sputtering.* Semiconductor Science and Technology, 2011. **26**(11): p. 115007.

44. Song, P.K., et al., *Electrical and optical properties of gallium-doped zinc oxide films deposited by dc magnetron sputtering.* Thin Solid Films, 2002. **411**(1): p. 82-86.

45. Wu, F., et al., *Effect of substrate temperature on the structural, electrical and optical properties of ZnO:Ga thin films prepared by RF magnetron sputtering.* Physica E: Low-dimensional Systems and Nanostructures, 2010. **43**(1): p. 228-234.

46. Nagarani, S. and C. Sanjeeviraja, *Structural, Electrical and Optical Properties of Gallium Doped Zinc Oxide Thin Films Prepared by Electron Beam Evaporation Technique.* AIP Conference Proceedings, 2011. **1349**(1): p. 589-590.

47. Ma, Q.B., et al., *Influence of Ar/O2 ratio on the properties of transparent conductive ZnO: Ga films prepared by DC reactive magnetron sputtering.* Materials Letters, 2007. **61**(11-12): p. 2460-2463.

48. Martins, R., et al., *Role of order and disorder on the electronic performances of oxide semiconductor thin film transistors.* Journal of Applied Physics, 2007. **101**: p. 044505.

49. Wong, L.M., et al., *Role of oxygen for highly conducting and transparent gallium-doped zinc oxide electrode deposited at room temperature.* Applied Physics Letters, 2011. **98**(2): p. 022106-3.

50. Huang, C.H., D.Y. Chen, and C.Y. Hsu, *Influence of deposition parameters and annealing treatment on the properties of GZO films grown using rf magnetron sputtering.* Ceramics International, 2012. **38**(2): p. 1057-1063.

51. Nunes, P., et al., *Effect of different dopant elements on the properties of ZnO thin films.* Vacuum, 2002. **64**(3-4): p. 281-285.

52. Kelly, P. and Y. Zhou, *Zinc oxide-based transparent conductive oxide films prepared by pulsed magnetron sputtering from powder targets: Process features and film properties.* Journal of Vacuum Science & Technology A: Vacuum, Surfaces, and Films, 2006. **24**: p. 1782.

53. Park, J.-S., et al., *Effects of Zn content on structural and transparent conducting properties of indium-zinc oxide films grown by rf magnetron sputtering.* Journal of Vacuum Science & Technology B: Microelectronics and Nanometer Structures, 2006. **24**(6): p. 2737-2740.

54. Kumar, B., H. Gong, and R. Akkipeddi, *High mobility undoped amorphous indium zinc oxide transparent thin films.* Journal of Applied Physics, 2005. **98**(7): p. 073703-5.

55. Martins, R., et al., *Transport in high mobility amorphous wide band gap indium zinc oxide films.* physica status solidi (a), 2005. **202**(9): p. R95-R97.

56. Naghavi, N., et al., *Systematic study and performance optimization of transparent conducting indium–zinc oxides thin films.* Electrochimica Acta, 2001. **46**(13–14): p. 2007-2013.

57. Wang, Y.L., et al., *Room temperature deposited indium zinc oxide thin film transistors.* Applied Physics Letters, 2007. **90**(23): p. 232103-232103-3.

58. Fortunato, E., et al., *High mobility and low threshold voltage transparent thin film transistors based on amorphous indium zinc oxide semiconductors.* Solid-State Electronics, 2008. **52**(3): p. 443-448.

59. Naghavi, N., et al., *Characterization of indium zinc oxide thin films prepared by pulsed laser deposition using a Zn3In2O6 target.* Thin Solid Films, 2000. **360**(1–2): p. 233-240.

60. Dehuff, N.L., et al., *Transparent thin-film transistors with zinc indium oxide channel layer.* Journal of Applied Physics, 2005. **97**(6): p. 064505-5.

61. Gonçalves, G., et al., *Crystallization of amorphous indium zinc oxide thin films produced by radio-frequency magnetron sputtering.* Thin Solid Films, 2008. **516**(7): p. 1374-1376.

62. Ito, N., et al., *Electrical and optical properties of amorphous indium zinc oxide films.* Thin Solid Films, 2006. **496**(1): p. 99-103.

63. Ku, D.Y., et al., *Structural and electrical properties of sputtered indium–zinc oxide thin films.* Thin Solid Films, 2006. **515**(4): p. 1364-1369.

64. Jeon, J.-W., et al., *Effect of annealing temperature on optical band-gap of amorphous indium zinc oxide film.* Journal of Alloys and Compounds, 2011. **509**(41): p. 10062-10065.

65. Lee, S., B. Bierig, and D.C. Paine, *Amorphous structure and electrical performance of low-temperature annealed amorphous indium zinc oxide transparent thin film transistors.* Thin Solid Films, 2011(0).

66. Takagi, A., et al., *Carrier transport and electronic structure in amorphous oxide semiconductor, a-InGaZnO4.* Thin Solid Films, 2005. **486**(1-2): p. 38-41.

67. Yabuta, H., *High-mobility thin-film transistor with amorphous InGaZnO4 channel fabricated by room temperature rf-magnetron sputtering.* Appl. Phys. Lett., 2006. **89**(11): p. 112123.

68. Shin, J.-H.C., Duck-Kyun., *Effect of Oxygen on the Optical and the Electrical Properties of Amorphous InGaZnO Thin Films Prepared by RF Magnetron Sputtering.* Journal of the Korean Physical Society, 2008. **53**(4): p. 5.

69. Na, J.H., M. Kitamura, and Y. Arakawa, *High field-effect mobility amorphous InGaZnO transistors with aluminum electrodes.* Applied Physics Letters, 2008. **93**: p. 063501.

70. Park, J.S., et al., *Electronic transport properties of amorphous indium-gallium-zinc oxide semiconductor upon exposure to water.* Applied Physics Letters, 2008. **92**: p. 072104.

71. Kwon, S., J. Park, and P.D. Rack, *Device Characteristics of Amorphous Indium Gallium Zinc Oxide TFTs Sputter Deposited with Different Substrate Biases.* Electrochemical and Solid-State Letters, 2009. **12**: p. H278.

72. Chen, J., *Substrate temperature influence on the properties of InGaZnO thin films grown by PLD technique.* Proc. SPIE, 2010. **7658**(1): p. 76580E.

73. Ko, J., et al., *Effects of ZnO addition on electrical and structural properties of amorphous SnO2 thin films.* Thin Solid Films, 2006. **494**(1-2): p. 42-46.

74. Jayaraj, M.K., et al., *Optical and electrical properties of amorphous zinc tin oxide thin films examined for thin film transistor application.* Journal of Vacuum Science & Technology B: Microelectronics and Nanometer Structures, 2008. **26**: p. 495.

75. Neamen, D.A., *An introduction to semiconductor devices*2006: McGraw-Hill.

76. Casey, H.C., *Devices for integrated circuits: silicon and III-V compound semiconductors*1999: John Wiley.

77. Weimer, P.K., *The TFT a new thin-film transistor.* Proceedings of the IRE, 1962. **50**(6): p. 1462-1469.

78. Fortunato, E., et al., *Zinc Oxide Thin-Film Transistors Zinc Oxide — A Material for Micro- and Optoelectronic Applications*, N.H. Nickel and E. Terukov, Editors. 2005, Springer Netherlands. p. 225-238.

79. Stallinga, P. and H. Gomes, *Modeling electrical characteristics of thin-film field-effect transistors:: I. Trap-free materials.* Synthetic metals, 2006. **156**(21-24): p. 1305-1315.

80. Wager, J.F., *ZnO Transparent Thin-Film Transistor Device Physics Zinc Oxide* in *ZnO Transparent Thin-Film Transistor Device Physics: Zinc Oxide — A Material for Micro- and Optoelectronic Applications*, N.H. Nickel and E. Terukov, Editors. 2005, Springer Netherlands. p. 217-224.

81. Boesen, G.F. and J.E. Jacobs, *ZnO field-effect transistor.* Proceedings of the IEEE, 1968. **56**(11): p. 2094-2095.

82. Meyers, S.T., et al., *Aqueous inorganic inks for low-temperature fabrication of ZnO TFTs.* Journal of the American Chemical Society, 2008. **130**(51): p. 17603-17609.

83. Kamiya, T. and H. Hosono, *Material characteristics and applications of transparent amorphous oxide semiconductors.* NPG Asia Materials, 2010: p. 15-22.

84. Boesen, G. and J. Jacobs, *ZnO field-effect transistor.* Proceedings of the IEEE, 1968. **56**(11): p. 2094-2095.

85. Fortunato, E., et al., *Recent advances in ZnO transparent thin film transistors.* Thin Solid Films, 2005. **487**(1-2): p. 205-211.

86. Kwon, S., et al., *Characteristics of the ZnO thin film transistor by atomic layer deposition at various temperatures.* Semiconductor Science and Technology, 2009. **24**: p. 035015.

87. Bae, H., et al., *Photodetecting properties of ZnO-based thin-film transistors.* Applied Physics Letters, 2003. **83**: p. 5313.

88. Lee, K., et al., *Interfacial Trap Density of States in Pentacene and ZnO Based Thin Film Transistors Measured via Novel Photo excited Charge Collection Spectroscopy.* Advanced Materials, 2010. **22**(30): p. 3260-3265.

89. Lee, K., et al., *Density of trap states measured by photon probe into ZnO based thin-film transistors.* Applied Physics Letters, 2010. **97**: p. 082110.

90. Powell, M.J., *The physics of amorphous-silicon thin-film transistors.* Electron Devices, IEEE Transactions on, 1989. **36**(12): p. 2753-2763.

91. Wehrspohn, R.B., et al., *Relative importance of the Si--Si bond and Si--H bond for the stability of amorphous silicon thin film transistors.* Journal of Applied Physics, 2000. **87**(1): p. 144-154.

92. Cross, R.B., *Investigating the stability of zinc oxide thin film transistors.* Appl. Phys. Lett., 2006. **89**(26): p. 263513.

93. Su, L.-Y., et al., *Study of the Effect of Electrical Stress on ZnO TFTs.* ECS Transactions, 2010. **33**(5): p. 331-336.

94. Navamathavan, R., et al., *Effects of Electrical Bias Stress on the Performance of ZnO-Based TFTs Fabricated by RF Magnetron Sputtering.* Journal of The Electrochemical Society, 2006. **153**(5): p. G385-G388.

95. Verma, V.P., et al., *Characteristics of low doped gallium-zinc oxide thin film transistors and effect of annealing under high vacuum.* Thin Solid Films, 2008. **516**(23): p. 8736-8739.

96. Barquinha, P., et al., *Effect of UV and visible light radiation on the electrical performances of transparent TFTs based on amorphous indium zinc oxide.* Journal of non-crystalline solids, 2006. **352**(9–20): p. 1756-1760.

97. Liu, P.-T., Y.-T. Chou, and L.-F. Teng, *Environment-dependent metastability of passivation-free indium zinc oxide thin film transistor after gate bias stress.* Applied Physics Letters, 2009. **95**(23): p. 233504-233504-3.

98. Xu, H., et al., *High performance indium-zinc-oxide thin-film transistors fabricated with a back-channel-etch-technique.* Applied Physics Letters, 2011. **99**(25): p. 253501-253501-4.

99. Hoffman, R., *Effects of channel stoichiometry and processing temperature on the electrical characteristics of zinc tin oxide thin-film transistors.* Solid-State Electronics, 2006. **50**(5): p. 784-787.

100. Hong, D., H.Q. Chiang, and J.F. Wager, *Zinc tin oxide thin-film transistors via reactive sputtering using a metal target.* Journal of Vacuum Science & Technology B: Microelectronics and Nanometer Structures, 2006. **24**(5): p. L23-L25.

101. Görrn, P., *Stability of transparent zinc tin oxide transistors under bias stress.* Appl. Phys. Lett., 2007. **90**(6): p. 063502.

102. Görrn, P., *The influence of visible light on transparent zinc tin oxide thin film transistors.* Appl. Phys. Lett., 2007. **91**(19): p. 193504.

103. Jeong, Y., et al., *Bias Stress Stability of Solution-Processed Zinc Tin Oxide Thin-Film Transistors.* Journal of The Electrochemical Society, 2009. **156**: p. H808.

104. Chen, Y.C., et al., *Bias-induced oxygen adsorption in zinc tin oxide thin film transistors under dynamic stress.* Applied Physics Letters, 2010. **96**: p. 262104.

105. Nayak, P.K., et al., *Environmental, Optical, and Electrical Stability Study of Solution-Processed Zinc–Tin–Oxide Thin-Film Transistors.* Display Technology, Journal of, 2011. **7**(12): p. 640-643.

106. Kang, D., *Amorphous gallium indium zinc oxide thin film transistors: Sensitive to oxygen molecules.* Appl. Phys. Lett., 2007. **90**(19): p. 192101.

107. Barquinha, P., et al., *The effect of deposition conditions and annealing on the performance of high-mobility GIZO TFTs.* Electrochemical and Solid-State Letters, 2008. **11**: p. H248.

108. Chiang, H.Q., et al., *Processing effects on the stability of amorphous indium gallium zinc oxide thin-film transistors.* Journal of non-crystalline solids, 2008. **354**(19-25): p. 2826-2830.

109. Barquinha, P., et al., *Toward high-performance amorphous GIZO TFTs.* Journal of The Electrochemical Society, 2009. **156**: p. H161.

110. Suresh, A., et al., *Room temperature pulsed laser deposited indium gallium zinc oxide channel based transparent thin film transistors.* Applied Physics Letters, 2007. **90**(12): p. 123512-123512-3.

111. Suresh, A., P. Wellenius, and J.F. Muth. *High performance transparent thin film transistors based on indium gallium zinc oxide as the channel material*. in *Electron Devices Meeting, 2007. IEDM 2007. IEEE International*. 2007.

112. Lee, J., *Bias-stress-induced stretched-exponential time dependence of threshold voltage shift in InGaZnO thin film transistors.* Appl. Phys. Lett., 2008. **93**(9): p. 093504.

113. Suresh, A. and J. Muth, *Bias stress stability of indium gallium zinc oxide channel based transparent thin film transistors.* Applied Physics Letters, 2008. **92**(3): p. 033502-033502-3.

114. Cho, I.T., et al., *Charge trapping and detrapping characteristics in amorphous InGaZnO TFTs under static and dynamic stresses.* Semiconductor Science and Technology, 2009. **24**: p. 015013.

115. Hoshino, K., et al., *Constant-voltage-bias stress testing of a-IGZO thin-film transistors.* Electron Devices, IEEE Transactions on, 2009. **56**(7): p. 1365-1370.

116. Chuang, C.-S., et al., *P-13: Photosensitivity of Amorphous IGZO TFTs for Active-Matrix Flat-Panel Displays.* SID Symposium Digest of Technical Papers, 2008. **39**(1): p. 1215-1218.

117. Jeong, J.H., et al., *Origin of subthreshold swing improvement in amorphous indium gallium zinc oxide transistors.* Electrochemical and Solid-State Letters, 2008. **11**: p. H157.

118. Kim, J.H., *Correlation of the change in transfer characteristics with the interfacial trap densities of amorphous In?Ga?Zn?O thin film transistors under light illumination.* Appl. Phys. Lett., 2011. **98**(23): p. 232102.

119. Lim, W., et al., *High performance indium gallium zinc oxide thin film transistors fabricated on polyethylene terephthalate substrates.* Applied Physics Letters, 2008. **93**: p. 082102.

120. Lim, W., et al., *Stable room temperature deposited amorphous $InGaZnO_4$ thin film transistors.* Journal of Vacuum Science & Technology B: Microelectronics and Nanometer Structures, 2008. **26**(3): p. 959-962.

121. Moon, M.R., et al., *Effects of Substrate Heating on the Amorphous Structure of InGaZnO Films and the Electrical Properties of Their Thin Film Transistors.* Applied Physics Express, 2010. **3**(11): p. 111101.

122. Jeon, S.J., et al., *Enhancement in electrical performance of indium gallium zinc oxide-based thin film transistors by low temperature thermal annealing.* Materials Science in Semiconductor Processing, 2011.

123. Jeong, J.K., et al., *Origin of threshold voltage instability in indium-gallium-zinc oxide thin film transistors.* Applied Physics Letters, 2008. **93**: p. 123508.

124. Park, S.M., T. Ikegami, and K. Ebihara, *Effects of substrate temperature on the properties of Ga-doped ZnO by pulsed laser deposition.* Thin Solid Films, 2006. **513**(1-2): p. 90-94.

125. Trinh, T.T., et al., *Improvement in the performance of an InGaZnO thin-film transistor by controlling interface trap densities between the insulator and active layer.* Semiconductor Science and Technology, 2011. **26**: p. 085012.

126. Yao, J., et al., *Electrical and Photosensitive Characteristics of a-IGZO TFTs Related to Oxygen Vacancy.* Electron Devices, IEEE Transactions on, 2011. **58**(4): p. 1121-1126.

127. Ogata, K., et al., *Control of chemical bonding of the ZnO surface grown by molecular beam epitaxy.* Applied surface science, 2004. **237**(1–4): p. 348-351.

128. Jang, Y.R., K.-H. Yoo, and S.M. Park, *Properties of ZnO Thin Films Grown on Si (100) Substrates by Pulsed Laser Deposition.* Journal of Materials Science & Technology, 2010. **26**(11): p. 973-976.

129. Oh, S.J., et al., *Improving the Electrical Properties of Zinc Tin Oxide Thin Film Transistors Using Atmospheric Plasma Treatment.* Electrochemical and Solid-State Letters, 2011. **14**: p. H354.

130. Jain, V.K., et al., *Study of post annealing influence on structural, chemical and electrical properties of ZTO thin films.* Journal of Alloys and Compounds, 2011. **509**(8): p. 3541-3546.

131. Cho, D.Y., et al., *Electronic structure of amorphous InGaO3 (ZnO) 0.5 thin films.* Thin Solid Films, 2009. **518**(4): p. 1079-1081.

132. Jeong, S., et al., *Role of Gallium Doping in Dramatically Lowering Amorphous Oxide Processing Temperatures for Solution Derived Indium Zinc Oxide Thin Film Transistors.* Advanced Materials, 2010. **22**(12): p. 1346-1350.

133. Kim, G.H., W.H. Jeong, and H.J. Kim, *Electrical characteristics of solution-processed InGaZnO thin film transistors depending on Ga concentration.* physica status solidi (a), 2010. **207**(7): p. 1677-1679.

134. Chen, M.-C., et al., *Influence of Oxygen Partial Pressure on Resistance Random Access Memory Characteristics of Indium Gallium Zinc Oxide.* Electrochemical and Solid-State Letters, 2011. **14**(12): p. H475-H477.

135. Chen, J., et al. *Substrate temperature influence on the properties of InGaZnO thin films grown by PLD technique*. 2010. Dalian, China: SPIE.

136. Wolf, S. and R.N. Tauber, *Silicon Processing for the VLSI Era: Process Technology*. 2 ed. Vol. 1. 2000.

137. *Atomic Processes on Surface and Film Growth*. Available from: http://surface.iphy.ac.cn/sf03/sputtering.htm.

138. *RF-magnetron sputtering: View*. Available from: http://www.mems-exchange.org/catalog/P1998/.

139. Jaeger, R.C., *Introduction to microelectronic fabrication*. Vol. 2. 2002: Prentice Hall Upper Saddle River, NJ.

140. Bowen, A.S., *The Structural and Electrical Properties of RF Sputtered ZnO:F Thin Films Deposited on Polyethylene Naphthalate and Glass*, in *Electrical and Computer Engineering*2009, North Carolina Agricultural and Technical State University: Greensboro. p. 84.

141. Alston, R.A., *RF-Sputtered Gallium Tin Zinc Oxide Films and Thin Film Transistors*, in *Electrical and Computer Engineering*2010, North Carolina Agricultural and Technical State University: Greensboro. p. 75.

142. Ewing, G.W. *Analytical Instrumentation Handbook*. [Book] 1997; 1454p.]. Available from: http://search.ebscohost.comsheba.ncat.edu/login.aspx?direct=true&db=nlebk&AN=12791&site=ehost-live.

143. Schroder, D.K., *Semiconductor material and device characterization*2006: Wiley-IEEE Press.

144. *Topic 5: What are the uses and hazards of waves that form the Electromagnetic Spectrum?* ; Available from: http://www.antonine-education.co.uk/physics_gcse/Unit_1/Topic_5/topic_5_what_are_the_uses_and_ha.htm.

145. Kwon, S., et al., *Quantitative Calculation of Oxygen Incorporation in Sputtered IGZO Films and the Impact on Transistor Properties.* Journal of The Electrochemical Society, 2011. **158**: p. H289.

146. Hwang, Y.H., et al., *Ultraviolet Photo-Annealing Process for Low Temperature Processed Sol-Gel Zinc Tin Oxide Thin Film Transistors.* Electrochemical and Solid-State Letters, 2012. **15**(4): p. H91-H93.

147. Kim, S., et al., *Impact of Oxygen Flow Rate on the Instability Under Positive Bias Stresses in DC-Sputtered Amorphous InGaZnO Thin-Film Transistors.* Electron Device Letters, IEEE, 2011. **PP**(99): p. 1-3.

148. Garces, N.Y., et al., *Production of nitrogen acceptors in ZnO by thermal annealing.* Applied Physics Letters, 2002. **80**(8): p. 1334-1336.

149. Kim, J.H., et al., *Correlation of the change in transfer characteristics with the interfacial trap densities of amorphous In–Ga–Zn–O thin film transistors under light illumination.* Applied Physics Letters, 2011. **98**(23): p. 232102-232102-3.

150. Casteleiro, C., et al., *Study of trap states in zinc oxide (ZnO) thin films for electronic applications.* Journal of non-crystalline solids, 2008. **354**(19-25): p. 2519-2522.

151. Oh, H., et al., *Photon-accelerated negative bias instability involving subgap states creation in amorphous In--Ga--Zn--O thin film transistor.* Applied Physics Letters, 2010. **97**(18): p. 183502-3.